Phenomenology of Dark Radiation and String Compactifications

Stephen Angus

Wadham College
University of Oxford

A thesis submitted for the degree of
Doctor of Philosophy in Theoretical Physics

Trinity Term 2014

Abstract

In this Thesis I explore aspects of dark radiation and its role in String Phenomenology. Dark radiation is any additional hidden type of relativistic matter present in the Universe today, conventionally labelled as an "excess effective number of neutrino species", ΔN_{eff}. It provides a powerful test of hitherto untested theoretical models based on fundamental theories such as String Theory.

I begin by considering dark radiation in the LARGE Volume Scenario, a phenomenologically viable class of string compactifications. First I review how the minimal setup slightly overproduces axionic dark radiation via modulus decay. I then demonstrate that loop corrections to the main competing visible-sector decay process have a negligible effect and are unable to alleviate the tension with observations.

In the following chapter I explore fibred extensions of the LARGE Volume Scenario. The predictions for ΔN_{eff} are qualitatively different: in particular, models with a sequestered visible sector on D3 branes at a singularity are swamped by massless axions and decisively ruled out. I then consider TeV-scale supersymmetry in a model with anisotropic modulus stabilisation. If the Standard Model is realised on D7 branes wrapping the small volume cycle a hierarchy of soft terms is generated, which may have applications to natural supersymmetry.

The final chapter takes a different approach and investigates the proposition that dark radiation, in the form of a Cosmic Axion Background, could explain the long-standing soft X-ray excess from galaxy clusters. I show for the Coma cluster that the morphology of the excess can be reproduced by axion-photon conversion in the intracluster magnetic field, provided the field is allowed to have more structure on smaller scales than typically assumed based on Faraday rotation data. This explanation requires an inverse axion-photon coupling $M \sim 10^{11} - 10^{12}\,\text{GeV}$ and a mean axion energy $\langle E_{\text{CAB}} \rangle \sim 50 - 250\,\text{eV}$.

Phenomenology of Dark Radiation and String Compactifications

Stephen Angus

Wadham College

University of Oxford

A thesis submitted for the degree of

Doctor of Philosophy in Theoretical Physics

Trinity Term 2014

"In the end it's only a
passing thing, this shadow;
even darkness must pass."

—Samwise Gamgee,
The Lord of the Rings

Acknowledgements

There are many people I would like to thank, a far greater number than I have time and space to mention here.

First and foremost, I am immensely thankful to my supervisor Joseph Conlon, who throughout my time as a DPhil student has been a constant source of encouragement, support, and motivation, and whose limitless enthusiasm is deeply inspiring. I am also indebted to my other collaborators, David Marsh, Ulrich Haisch, Andrew Powell, and Lukas Witkowski, who have been a pleasure to work with and from whom I have learned much over the past few years. In addition, I would like to thank everyone else who has provided me with advice, feedback, and inspiring discussions over my years as a research student — an incomplete list includes: Michele Cicoli, Graham Ross, Andre Lukas, Sven Krippendorf, Francisco Pedro, Markus Rummel, Doddy Marsh, Mark Goodsell, Jeroen Franse, Pedro Alvarez, Francesca Day, Ed Hardy, Eirik Svanes, Felix Kahlhöfer, James Unwin, ...

Furthermore, I owe a debt of gratitude to Wadham College, for taking care of me for eight years as both an undergraduate and a postgraduate student. In my time as an undergraduate I benefited greatly from the tuition of Martin Bureau, Giulia Zanderighi, Dean Horton, and in particular Candadi Sukumar, whose inspiring devotion to the mysteries of the Universe has been a key influence on my intellectual development and research interests. Also, I would like to thank the STFC for graciously providing me with a studentship, which has allowed me to continue to study Physics for the past four years.

With regard to that other type of string, I am extremely thankful to the Oxford University Orchestra, the Oxford University Philharmonia, and the many other orchestras and ensembles in which I've played violin during my time at Oxford, as well as to all the amazingly fun and interesting people I've met as a consequence, who have enriched immeasurably my time amongst the dreaming spires.

On a personal level, there are some people to whom I owe special thanks: to Kim Lake, whose existence I am extremely grateful for and whose relentless dedication to spreading joy makes the world a better place; to Sami Massey, for offering to proofread, for keeping me calm in times of stress, and for being an unbelievably awesome and supportive friend; and to all my other friends, past and present, who have cheered me up, looked out for me, and shaped me into the person I am today. Last but definitely not least, I would like to thank a pair of unsung heroes: my parents, Louise and Ross Angus, whose unwavering love and support has been the bedrock of my life.

Statement of Originality

This Thesis is the result of my own work and no part is the result of work done in collaboration, except where specifically indicated in the text. No part of this Thesis has previously been submitted, nor is being submitted concurrently, for a degree or other qualification at this or any other University. The original research presented in this Thesis is based on the papers [1–4].

The Introduction and sections 2.1 and 2.2 consist of background information on dark radiation and string compactifications. The remainder of Chapter 2 contains original research based on the paper [2]. My main contribution to this paper was to compute the one-loop anomalous dimension of the coupling (2.27). The calculation is presented in detail in Appendix A, which is entirely my own work except section A.2.3, which was written primarily by Andrew J. Powell. Section 2.5 is based on text written primarily by Ulrich Haisch.

Chapter 3 contains original research based on the papers [1] and [4]. Sections 3.2 and 3.3 are based on [4], which is entirely my own work. The remainder of the chapter is based on [1], in which I performed all of the calculations and wrote most of the text. Section 3.4 prior to section 3.4.1, and section 3.7.3, are based on material written primarily by Joseph P. Conlon.

Chapter 4 contains original research based on the paper [3]. This paper was written collaboratively with Joseph P. Conlon, M.C. David Marsh, Andrew J. Powell, and Lukas T. Witkowski as the result of a large collaborative project. My main contributions to this project were writing some early axion-photon conversion code and analysing the simulation data, in order to obtain predictions for the soft-excess morphology. Section 4.2 is based on work by Joseph P. Conlon and M.C. David Marsh, and it has been included here for completeness.

Abstract

In this Thesis I explore aspects of dark radiation and its role in String Phenomenology. Dark radiation is any additional hidden type of relativistic matter present in the Universe today, conventionally labelled as an "excess effective number of neutrino species", $\Delta N_{\rm eff}$. It provides a powerful test of hitherto untested theoretical models based on fundamental theories such as String Theory.

I begin by considering dark radiation in the LARGE Volume Scenario, a phenomenologically viable class of string compactifications. First I review how the minimal setup slightly overproduces axionic dark radiation via modulus decay. I then demonstrate that loop corrections to the main competing visible-sector decay process have a negligible effect and are unable to alleviate the tension with observations.

In the following chapter I explore fibred extensions of the LARGE Volume Scenario. The predictions for $\Delta N_{\rm eff}$ are qualitatively different: in particular, models with a sequestered visible sector on D3 branes at a singularity are swamped by massless axions and decisively ruled out. I then consider TeV-scale supersymmetry in a model with anisotropic modulus stabilisation. If the Standard Model is realised on D7 branes wrapping the small volume cycle a hierarchy of soft terms is generated, which may have applications to natural supersymmetry.

The final chapter takes a different approach and investigates the proposition that dark radiation, in the form of a Cosmic Axion Background, could explain the long-standing soft X-ray excess from galaxy clusters. I show for the Coma cluster that the morphology of the excess can be reproduced by axion-photon conversion in the intracluster magnetic field, provided the field is allowed to have more structure on smaller scales than typically assumed based on Faraday rotation data. This explanation requires an inverse axion-photon coupling $M \sim 10^{11} - 10^{12}\,\text{GeV}$ and a mean axion energy $\langle E_{\rm CAB}\rangle \sim 50 - 250\,\text{eV}$.

Contents

List of Figures

List of Tables

Chapter 1

Introduction

1.1 Overview

For the past few decades, almost every known physical phenomenon has been explained within the framework of a single theory: the Standard Model of Particle Physics. This quantum field theory successfully describes the strong, electromagnetic and weak forces of nature, which mediate interactions between three generations of quarks and leptons. The final ingredient, the Higgs boson, was discovered in July 2012, filling in the final piece of the puzzle and providing final confirmation of the Standard Model as an accurate description of our world and one of the pillars of modern physics. However, the Standard Model, while successful up to at least the TeV-scale (corresponding to distances of order $\sim 10^{-18}\,\mathrm{m}$) and consistent at energies below the Planck scale, encodes its own incompleteness. The Higgs boson, observed to have a mass of $m_H = 125\,\mathrm{GeV}$, receives loop corrections that are quadratically dependent on the energy scale at which it is observed. This implies a severe fine-tuning of the Higgs mass, a quandary known as the electroweak hierarchy problem.

More significantly, the Standard Model does not incorporate gravity. This is instead described by the second pillar of modern physics, Einstein's General Theory of Relativity, in which matter and energy induce curvature in the fabric of spacetime, giving rise to an effective gravitational force. However, upon attempting to quantise gravity at the Planck scale, $M_\mathrm{P} = 2.4 \times 10^{18}\,\mathrm{GeV}$ (the

natural energy scale of gravity), one encounters an infinte number of uncontrollable divergences. It is impossible to cancel all of them using counterterms — a consequence of the fact that General Relativity is non-renormalisable when expressed as a quantum theory, so loop corrections stack up and perturbation theory breaks down. Hence the second pillar also begins to crumble when pushed beyond its limits. Furthermore, the standard ΛCDM Cosmological model demands the presence of Dark Matter, which cannot be accounted for by any of the observed particles, and a Cosmological Constant (also known as Dark Energy), the nature of which is mysterious. Furthermore, the observed Dark Energy abundance requires a fine-tuning of one part in 10^{120} to reconcile its value in our Universe with the typical values expected from quantum field theory — this is known as the cosmological hierarchy problem.

In principle, all of the above can be explained by introducing new physics. For example, a popular solution to the electroweak hierarchy problem is to invoke supersymmetry and postulate the existence of bosonic superpartners to the known fermions, and vice versa. In such supersymmetric extensions of the Standard Model, the quadratic divergences to the Higgs mass are cancelled by an equal and opposite-sign contribution from the superpartners (for example, stop squark loops in the case of the top quark contribution). In particular models, the lightest supersymmetric particle (LSP) can be rendered stable and thus provide a candidate for dark matter.

Furthermore, scientific reductionism implies that the Standard Model and General Relativity should each be subsumed into a broader theory, a Theory of Everything, in which all of the above issues are ultimately resolved. This can also be understood from a Wilsonian point of view: at some higher energy scale, beyond which we have currently observed, new physics should appear. We do not observe this new physics from our relatively low-energy vantage point because these high-energy (and hence short-distance) modes have been 'integrated out' — heuristically this means that our current detectors have too low a resolution to pick out the fine underlying details, which are instead

smeared out. From this perspective, the Standard Model and General Relativity can be understood as low-energy *effective* theories, and the prospective Theory of Everything is their *ultraviolet (UV) completion*.

The best-understood candidate UV completion of the Standard Model is String Theory. In its simplest realisation, which consists only of bosons, string theory describes matter not as infinitesimal point particles travelling on a worldline, but as one-dimensional strings living on a worldsheet. String excitations then correspond to higher-spin states — in particular, there is always a spin-2 excitation corresponding to the graviton. However, bosonic string theory also predicts the existence of tachyons, particles whose mass squared is negative and which thus travel faster than light, violating causality. Their existence can be avoided by introducing supersymmetry. The resulting *superstring theory* now includes fermions and has five consistent realisations, known as Type I, Type IIA and IIB, and the Heterotic SO(32) and $E_8 \times E_8$ superstring theories, respectively. Furthermore, it turns out that these five theories are not so independent after all — it has been shown that they are all interrelated via duality transformations, and in conjunction with eleven dimensional supergravity they form perturbative limits of the mysterious framework known as M-theory [5].

However, there are some major problems with String Theory as a theory of quantum gravity, which can be divided into roughly two classes: *predictivity* and *testability*. First of all, with regard to testability, the prediction of particles having a one-dimensional structure would typically be expected to produce an observable effect only at the Planck scale, $l \simeq 10^{-33}\,\mathrm{m}$, well beyond the reach of any current or near-future particle accelerator. Furthermore, the requirement that physical theories must be free of anomalies demands that any consistent superstring theory must exist in ten spacetime dimensions. Consequently, the extra six spatial dimensions must somehow be unobservable to us — this can be achieved by compactification on a six-dimensional manifold, such as a Calabi-Yau manifold or an orbifold.

Unfortunately this raises some further problems. Any compactification will give rise to scalar fields called moduli, which heuristically speaking correspond to the size and shape of the extra-dimensional manifold. *A priori* these massless zero-modes can take any value, which will tend to result in decompactification. This is the problem of moduli stabilisation — how do the extra dimensions remain compact? One solution is the following: Type IIA and IIB theories both contain extended multidimensional membrane-like objects called Dp branes, which are extended in $p+1$ dimensions and can become magnetised in the presence of flux (higher-dimensional tensor generalisations of the gauge fields present in four-dimensional quantum field theories). When these objects are wrapped around compact cycles in the geometry, the flux becomes quantised and some (but not all) of the moduli can be stabilised. However, this induces a problem of predictivity — in a typical Calabi-Yau there are $\mathcal{O}(100)$ cycles around which branes could be wrapped, each of which is allowed to satisfy $\mathcal{O}(10)$ quantisation conditions, so the estimated number of degenerate Calabi-Yau vacua is $\gtrsim 10^{500}$ [6]. This is known as the *landscape problem*.

Given this state of affairs, has String Theory failed as a predictive theory? Does it even give testable predictions? These are the questions that String Phenomenology seeks to answer. One way in which it does so is by abandoning the notion of String Theory as a uniquely-defined theory and instead approaching it as a model-building framework in which problems in quantum gravity can be addressed directly. In recent years there has been substantial progress in this area, which broadly falls into two different categories. The first approach is to brute-force the landscape and attempt to count the number of Calabi-Yau compactifications that lead to a Universe that has broadly the same physical properties as our own. Another approach is to attempt to build specific models that have desirable properties — examples of this are the KKLT scenario [7] and the LARGE Volume Scenario [8–10]. The latter is particularly interesting because it produces an exponentially large compactification volume for natural ($\mathcal{O}(1)$) input parameters, which in turn leads to a prediction of new particles

with masses many orders of magnitude below the Planck scale, providing a natural solution to the hierarchy problem.

These approaches have successfully begun to create a bridge across the vast chasm between String Theory and experiment. However they still rely upon testing the properties of particular models to determine whether they are consistent with our Universe; if they are not we can always retreat to an alternative scenario, and the promise of String Theory remains. As such, many have accused String Theory of being *unfalsifiable*. This begs the question: is there any physical phenomenon that is within reach of current experiments, of which observation or lack thereof would decisively confirm or exclude a wide class of string models? The answer is yes, and it is the subject of this thesis.

Dark radiation is a catch-all term to describe any extra hidden type of relativistic particle species present in the Universe today, in addition to the usual photons and three generations of neutrinos. Cosmologists have historically parametrised dark radiation as an "excess effective number of neutrino species,"

$$\Delta N_{\rm eff} = \frac{8}{7}\left(\frac{11}{4}\right)^{4/3}\frac{\rho_{\rm DR}}{\rho_\gamma}\ . \tag{1.1}$$

Unfortunately, for our purposes this notation is extremely obfuscating. $\Delta N_{\rm eff}$ is simply the energy density in dark radiation normalised to the energy density of photons in the Universe, so it need not be integer-valued. Furthermore there is no requirement (and very little theoretical motivation) that the extra radiation should be an additional neutrino species: it could be, for example, a massless axion or a dark photon. It need not even be a single type of particle — an excess could be the sum total of additional energy due to several hidden radiation components.

It is possible to observe dark radiation indirectly from the Cosmic Microwave Background (CMB). Primordial fluctuations in the early Universe determine how the temperature of CMB photons from different patches of the sky are correlated depending on their relative separation. These photons originate

from the surface of last scattering; by expanding the correlations as spherical harmonics on this surface, one can construct the CMB power spectrum. The shape of this spectrum depends on the thermal history of the Universe and on the different contributions to the energy density of the Universe at different times in its history. In particular, from the ratio between the first peak and the damping tail, the total energy density present in radiation after recombination can be inferred. Comparing the value thus obtained with estimates of the total radiation density in photons gives a prediction for the effective number of neutrino species (i.e. neutrinos plus dark radiation).

Recent experiments have hinted at the existence of about half a neutrino's worth of dark radiation, corresponding to $\Delta N_{\rm eff} \simeq 0.5$. Assuming a tensor-to-scalar ratio $r = 0$, a combination of recent CMB observations by Planck [11], high-l data from SPT [12] and ACT [13], WMAP 9-year polarisation data [14], BAO measurements, and the value of H_0 observed by the Hubble Space Telescope [15], suggests $N_{\rm eff} = 3.52^{+0.48}_{-0.45}$ at 95% c.l.. Meanwhile, independent constraints from Big Bang Nucleosynthesis give $N_{\rm eff} = 3.50 \pm 0.20$ [16].[1] These constraints are set to tighten significantly in the next ten years, with sensitivities down to $\Delta N_{\rm eff} \lesssim 10^{-4}$ predicted.

In many string models, dark radiation is commonplace. In compactifications of Type IIB String Theory, moduli parametrising the size of the extra dimensions (known as Kähler moduli) are always present. Their imaginary part a obeys a shift symmetry,

$$a \to a + c \,, \tag{1.2}$$

where c is a real constant. Such a particle is known in the string literature as an *axion*.[2] The shift symmetry places strong restrictions on the a-dependent

[1]The case for dark radiation is further enhanced if one incorporates the claimed discovery of primordial B-modes by BICEP2 [17]: using a ΛCDM+r model with a tensor-to-scalar ratio $r = 0.20^{+0.07}_{-0.05}$, the authors of [18] find a preference for dark radiation with $N_{\rm eff} = 4.00 \pm 0.41$ [Planck+WP+BICEP2] at 68% c.l.; meanwhile, other similar studies [19, 20] find $N_{\rm eff} \sim 3.86 \pm 0.25$ and $N_{\rm eff} \sim 3.95 \pm 0.33$ at 68% c.l., respectively.

[2]In the experimental/phenomenological literature, the term "axion" is reserved for the

terms that are allowed in the Lagrangian. One such consequence is that in phenomenologically viable compactifications, there is usually at least one massless axion present, which can play the role of dark radiation. In fact, Type IIB compactifications typically have hundreds of moduli with associated light axions, and hence hundreds of dark radiation candidates.

Furthermore, in models with compact extra dimensions such as string models, the Universe typically enters a moduli-dominated phase at the end of inflation. The lightest of these moduli is the longest-lived, and its decays to visible matter reheat the Universe and give rise to a standard hot Big Bang cosmology. Notably, the branching fraction of the decays of this modulus to dark radiation is often the same order of magnitude as the fraction decaying to visible matter, so even the presence of only a single light axion species can yield a sizable fraction of dark radiation [21, 22]. The conclusion we can draw from this is that by measuring the amount of dark radiation we can constrain a broad range of contemporary string models, many of which will be excluded in the near future.

The structure of this thesis is as follows. In the remainder of this chapter I review terminology related to dark radiation and its context in the thermal history of the Universe, while introducing some technical concepts that will prove useful later. Following this, in Chapter 2 I discuss dark radiation in the context of a simple, phenomenologically viable model based on the LARGE Volume Scenario. I show how this minimal model is in tension with data, even after loop corrections are accounted for. In Chapter 3 I explore extensions of the minimal model in which the Calabi-Yau has a fibration structure, which has significant consequences for dark radiation production. The rest of the chapter is then devoted to discussion of a phenomenologically interesting model in which the Calabi-Yau is stabilised very anisotropically, leading to an unusual and distinctive low-energy matter spectrum.

QCD axion; the particles we are discussing would instead be referred to as "axion-like particles" (ALPs). Henceforth we will use the terms "axion" and "ALP" interchangeably.

The remainder of this thesis is devoted to a detailed exploration of a new and exciting idea, which connects dark radiation to a long-standing astrophysical mystery. The axions produced in the early Universe from moduli decay interact extremely weakly with visible matter, so they stream freely to the present day, forming a Cosmic Axion Background (CAB). In certain circumstances these axions can convert into photons in the presence of a magnetic field. Normally this effect is tiny; however, when the axions propagate through an extremely large object such as a galaxy cluster, the effect is coherent and the conversion rate to photons can easily reach observable levels. In fact, there is a known excess of low-energy X-rays from galaxy clusters — in Chapter 4 I explain how axion-photon conversion occurs in galaxy clusters and describe the results of a detailed numerical simulation of this effect in the Coma cluster. Finally, in Chapter 5 I draw these strands together and discuss prospects for future work.

1.2 Reheating and dark radiation

1.2.1 The excess effective number of neutrino species

The present-day radiation content of the Universe can be described in terms of the energy density associated with each relativistic particle species — at present this radiation consists of photons and neutrinos plus any additional hidden components, which we call *dark radiation* (DR):

$$\rho_{\rm radiation} = \rho_\gamma + \rho_\nu + \rho_{\rm DR} \ . \tag{1.3}$$

We would like to express this in terms of an effective number of neutrino species, $N_{\rm eff}$, defined at the time of neutrino decoupling as

$$N_{\rm eff} \equiv \left. \frac{\rho_{\nu\ {\rm eff}}}{\rho_{1\nu}} \right|_{T_{\rm dec}} \ . \tag{1.4}$$

The energy density of each radiation component is

$$\rho_i = \frac{\pi^2}{30}\, g_{*,i}(T_i) T_i^4 \ , \tag{1.5}$$

where T_i is temperature and $g_{*,i}$ is the effective number of degrees of freedom associated with the component. For fermions, the latter comes with a factor of 7/8 relative to bosons, accounting for the difference between Fermi-Dirac and Bose-Einstein statistics. The entropy in a comoving volume is conserved, implying that $a(T)^3 g_*(T) T^3$ is constant ($a(T)$ is the scale factor of the Universe). In particular, neutrinos are decoupled from the thermal bath and $g_{*,\nu}$ does not change as the Universe expands and cools.

On the other hand, photons interact with the thermal plasma so we must account for the e^+e^--annihilation that takes place after neutrino decoupling — this reduces g_* from 11/2 at the time of decoupling, when electrons and positrons were present in the thermal bath, to 2 at CMB times, when only the two photon polarisations make a contribution. Since by definition neutrinos and photons were in local thermal equilibrium at decoupling, the present-day neutrino temperature is

$$\left.\frac{T_\nu}{T_\gamma}\right|_{\rm CMB} = \left(\frac{g_*^{\rm CMB}}{g_*^{\rm dec}}\right)^{1/3} = \left(\frac{4}{11}\right)^{1/3} . \tag{1.6}$$

Hence the relationship between the total radiation energy density and $N_{\rm eff}$ is

$$\rho_{\rm radiation} = \rho_\gamma \left[1 + \frac{7}{8}\left(\frac{4}{11}\right)^{4/3} N_{\rm eff}\right] . \tag{1.7}$$

If there was no dark radiation we would expect to find $N_{\rm eff} = 3.046$ — this is slightly greater than 3 to account for partial reheating due to e^+e^--annihilation. Any excess can be accounted for by the presence of dark radiation,

$$\rho_{\rm DR} = \rho_\gamma \left(\frac{7}{8}\left(\frac{4}{11}\right)^{4/3} \Delta N_{\rm eff}\right) , \tag{1.8}$$

where

$$\Delta N_{\rm eff} = N_{\rm eff} - 3.046 . \tag{1.9}$$

1.2.2 Reheating via decay of a heavy scalar field

We would like to relate $\Delta N_{\rm eff}$ to theoretical models of the early Universe. The isotropy of the CMB over large scales can be explained by *inflation*, which

postulates a period of rapid accelerated expansion in the very early history of the Universe. This is followed by a period of *reheating*, in which the expansion slows and energy is transferred to the Standard Model particles, which enter local thermal equilibrium. This reproduces all the successful predictions of the hot Big Bang model while explaining the observation that photons could only have travelled at most 1° on the night sky if a purely thermal history were assumed (rendering an isotropic CMB extremely unlikely).

Consider the scenario in which the Universe is reheated by a single scalar Φ decaying into Standard Model particles with branching fraction $B_{\rm SM}$.[3] Suppose that this scalar can also decay into dark radiation, with each decay producing two dark relativistic species a, with branching fraction B_a. The axions subsequently decouple and no longer interact with the thermal plasma — they remain extremely non-interacting thereafter, simply redshifting with the expansion as radiation,[4]

$$\rho_a \sim a(T)^{-4} \, . \tag{1.10}$$

The Standard Model states produced by the decay will also be relativistic; however, as the Universe expands and cools the number of relativistic degrees of freedom will decrease whenever the temperature of the thermal bath drops below the mass of a particle species. Hence by applying conservation of comoving entropy to (1.5), we see that the energy density of relativistic visible matter dilutes as

$$\rho_{\rm SM} \sim g_*(T)^{-1/3} a(T)^{-4} \, , \tag{1.11}$$

[3]This scalar could be, for example, one of the moduli in String Theory.

[4]Equation (1.10) has a simple origin. The scale factor $a(T)$ relates spatial coordinates x to physical distances r: $r = a(T)x$. Since energy densities scale inversely with volume, a $a(T)^{-3}$ dependence is induced. For non-relativistic matter this is the end of the story, since $E \sim m$. However, the energy in relativistic matter (i.e. radiation) is inversely proportional to its wavelength, $E \sim 1/\lambda$, which introduces an additional factor of $a(T)^{-1}$.

so we find that

$$\left.\frac{\rho_a}{\rho_{\rm SM}}\right|_{T_{\rm dec}} = \left(\frac{g_*(T_{\rm dec})}{g_*(T_{\rm rh})}\right)^{1/3} \left.\frac{\rho_a}{\rho_{\rm SM}}\right|_{T_{\rm rh}} = \left(\frac{g_*(T_{\rm dec})}{g_*(T_{\rm rh})}\right)^{1/3} \frac{B_a}{B_{\rm SM}} \,. \tag{1.12}$$

At the time of neutrino decoupling the thermal bath consists of photons, neutrinos, electrons and positrons, so $g_*(T_{\rm dec}) = 10.75$.

What is the reheating temperature, $T_{\rm rh}$? We can estimate it as follows. Reheating occurs when the expansion rate of the Universe slows down sufficiently that it becomes comparable to the decay rate of Φ. The expansion rate is given by the Hubble parameter, $H \equiv \dot{a}/a$, which is related to the energy density in radiation though the Friedmann–Robertson–Walker (FRW) equation. For a radiation-dominated universe,

$$H^2 = \frac{8\pi G_{\rm N}\rho}{3} \sim \frac{T^4}{M_{\rm P}^2} \,, \tag{1.13}$$

where the reduced Planck mass $M_{\rm P} = 1/\sqrt{8\pi G_{\rm N}}$ in natural units ($\hbar = c = 1$). In the next section we will show that the decay rate of Φ is of order $\Gamma_\Phi \sim m_\Phi^3/M_{\rm P}^2$, so the reheating temperature is approximately

$$T_{\rm rh} \sim \sqrt{\Gamma_\Phi M_{\rm P}} \sim \frac{m_\Phi^{3/2}}{M_{\rm P}^{1/2}} \,. \tag{1.14}$$

For $m_\Phi \sim 10^6\,{\rm GeV}$, as one might expect for TeV-scale supersymmetry, the reheating temperature is $T_{\rm rh} \sim 1\,{\rm GeV}$.

Finally, we would like to relate the total density of Standard Model radiation to that in one neutrino species. From (1.5), the density ratio is simply the ratio of $g_*(T_{\rm dec})$ to the effective number of degrees of freedom in one neutrino generation, so

$$\left.\frac{\rho_{\rm SM}}{\rho_{1\nu}}\right|_{T_{\rm dec}} = \frac{10.75}{2\cdot\frac{7}{8}} = \frac{43}{7} \,. \tag{1.15}$$

Bringing it all together, we take the product of (1.12) and (1.15) to find

$$\Delta N_{\rm eff} = \left.\frac{\rho_a}{\rho_{1\nu}}\right|_{T_{\rm dec}} = \left.\frac{\rho_a}{\rho_{\rm SM}}\right|_{T_{\rm dec}} \left.\frac{\rho_{\rm SM}}{\rho_{1\nu}}\right|_{T_{\rm dec}}$$
$$\Delta N_{\rm eff} = \frac{43}{7}\left(\frac{10.75}{g_*(T_{\rm rh})}\right)^{1/3} \frac{B_a}{B_{\rm SM}} \,. \tag{1.16}$$

This expression relates primordial branching fractions to the amount of dark radiation present in the Universe, and so it underpins much of the analysis in this thesis.

1.3 Type IIB Calabi-Yau orientifolds

This section provides an overview of key aspects of a phenomenologically viable class of Type IIB String Theory compactifications known as *Calabi-Yau orientifolds*. The low-energy effective field theories corresponding to string models are *supergravity* theories - we provide a brief review of concepts in supersymmetry, supergravity and string compactifications before introducing a particularly powerful model known as the LARGE Volume Scenario.

1.3.1 Supersymmetry and Supergravity

In nature, two types of continuous symmetry have thus far been observed: Poincaré symmetry, which includes translations in spacetime as well as Lorentz transformations (rotations in space and Lorentz boosts to a frame moving at constant relative velocity); and internal (gauge) symmetries, such as those responsible for the strong and electroweak forces. In 1967, Coleman and Mandula proved that these are the only continuous bosonic symmetries allowed in a consistent four-dimensional quantum field theory, and that these two types of symmetry cannot have any non-trivial dependence on each other.[5] However,

[5]In group-theoretical terms their commutator vanishes, so each is in the singlet representation of each other — if you move in spacetime then perform a gauge transformation, you get the same result as if you had made the gauge transformation first. The symmetries are independent, and the overall symmetry group can be expressed as a direct sum of gauge and Poincaré symmetry.

they did not account for *fermionic* symmetries, the generators of which may anticommute to produce a spacetime translation,

$$\left\{Q_\alpha, \overline{Q}_{\dot{\alpha}}\right\} = 2\sigma^\mu_{\alpha\dot{\alpha}} P_\mu \ . \tag{1.17}$$

The Qs and $\overline{Q}$s act on bosonic fields to produce fermions, and vice-versa — such transformations are known as *supersymmetry* (SUSY) transformations. Equation (1.17) includes the minimal set of supersymmetry generators, known as $\mathcal{N} = 1$ SUSY; it is also possible to have multiple independent copies of this minimal set, corresponding to $\mathcal{N} = 2$, etc. In four dimensions the spinor indices α and $\dot{\alpha}$ each run over two components, so a theory with $\mathcal{N} = 1$ SUSY in 4d has four supersymmetry transformations that leave the theory invariant (or equivalently, it has four conserved *supercharges*).[6]

For $\mathcal{N} = 1$ supersymmetry, it is possible to write the bosonic fields and their fermion partners together in a single *superfield*, which exists in a version of spacetime augmented by the addition of two anticommuting coordinates, θ and $\overline{\theta}$, called *superspace*. For example, a *chiral superfield* Φ contains no $\overline{\theta}$-dependent terms and takes the form

$$\Phi(x, \theta, \overline{\theta}) = \phi(x) + \sqrt{2}\theta\psi(x) + \theta\theta F(x) \ , \tag{1.18}$$

where $F(x)$ is a non-dynamical field. The Lagrangian describing a supersymmetric theory can be derived from two functions: the Kähler potential $K(\Phi_i, \Phi_i^\dagger)$, which typically generates kinetic terms; and the superpotential $W(\Phi_i)$, which is holomorphic (independent of the $\Phi_i^\dagger$s) and typically generates supersymmetric mass terms and interactions. Notably, $W(\Phi_i)$ is not renormalised to any order in perturbation theory.[7]

[6] *Noether's theorem* is one of the most powerful results in theoretical physics — it states that for every continuous symmetry of a physical theory, there is an associated quantity that is conserved. For example, the invariance of the laws of physics under translation in space/time gives rise to momentum/energy conservation, while electric charge is conserved as a result of the U(1) gauge symmetry of the electromagnetic field.

[7] This can be understood heuristically as follows. Perturbation theory is an expansion in coupling parameters, and the couplings of any physical theory are strictly real. On the other hand, couplings in supersymmetric theories can be understood as the vacuum expectation

Global supersymmetry is the invariance of a theory under a supersymmetry transformation that, for any particular field, acts identically on it at every point in spacetime. However, General Relativity famously promotes the global Lorentz symmetry of Special Relativity to a local symmetry, under which the fields transform differently at different points. A theory that is invariant under a local symmetry can be realised by introducing a connection, which ensures that fields at different points transform in a covariant manner, giving rise to curvature. Examples of this include: the Levi-Civita connection in General Relativity, which defines parallel transport in any coordinate system and induces curvature in spacetime; the photon gauge field, which promotes the complex phase of charged particles to a local symmetry; and the gluons, which promote quark color to a local symmetry. To combine supersymmetry with gravity we also need to promote supersymmetry to a local symmetry — the resulting framework is known as *supergravity*.

In supergravity theories there are well-known expressions for the terms that appear in the Lagrangian [23]. For example, the scalar kinetic terms are

$$\mathcal{L} \supset -K_{i\bar{j}}\partial_\mu\phi^i\partial^\mu\phi^{*\bar{j}} \ , \tag{1.19}$$

where $K_{i\bar{j}} = \partial_i\overline{\partial}_{\bar{j}}K$ is known as the *Kähler metric*. Another important term is the supergravity scalar potential, which takes the form

$$V = e^K\left[K^{i\bar{j}}(D_iW)(\overline{D_{\bar{j}}W}) - 3|W|^2\right] \ , \tag{1.20}$$

where $K^{i\bar{j}}K_{k\bar{j}} = \delta^i_k$, $D_iW = W_i + K_iW$, and subscript indices $i, j, \ldots$ denote partial derivatives with respect to the scalar fields ϕ^i.

1.3.2 Compactification of Type IIB String Theory

In the perturbative regime, Type IIB String Theory can be described as a supergravity theory in 10 spacetime dimensions. This theory has $\mathcal{N} = 2$ su-

values (VEVs) of superfields, and the superpotential is a holomorphic function of all such superfields, i.e., including both real and imaginary parts together. Therefore any perturbative expansion of $W(\Phi_i)$ would either not be purely real or not be holomorphic, so such an expansion is impossible.

persymmetry, and the smallest irreducible spinor in 10d has 16 independent components, so there are 32 supercharges in total. We would like to compactify six of the spatial dimensions while preserving some of the supersymmetry — this can be done by compactifying on a *Calabi-Yau manifold*. Such a compactification breaks 3/4 of the supersymmetry, leaving only 8 unbroken supercharges corresponding to $\mathcal{N} = 2$ supersymmetry in 4d. However we are not quite done because quarks and leptons are chiral fermions (i.e. they have a handedness), which are only allowed in (at most) $\mathcal{N} = 1$ supersymmetric theories. The final step is to use an *orientifold projection*, an operation that interchanges left- and right-moving string states and can be understood heuristically as a higher-dimensional parity operation. Only states left invariant under this orientifold projection are preserved, which further breaks supersymmetry down to $\mathcal{N} = 1$.

Compactification of Type IIB String Theory on Calabi-Yau orientifolds has proven to be a fruitful avenue for research, leading to a plethora of phenomenologically viable models. Deformations of the compactified manifold give rise to scalar fields called *moduli*, which are massless directions in the scalar potential and thus need to be stabilised to avoid decompactification. The problem of moduli stabilisation can be solved partially by wrapping magnitised D-branes around cycles (compact directions) in the extra-dimensional geometry. The resulting "flux compactifications" stabilise approximately half of the moduli supersymetrically [24], namely the *axio-dilaton* S and the *complex structure moduli* U_α that describe the shape of the compact geometry.

However, one class of moduli remains unstabilised — the *Kähler moduli* τ_i parametrising the volumes of compact 4-cycles in the geometry. Additionally, the theory contains a four-index tensor flux potential C_4 (whose derivative is a self-dual field strength, a higher-rank tensor analogue of electromagnetic flux), the dimensional reduction of which around any orientifold-invariant 4-cycle D_4^+ is equivalent to an axion,

$$a_i = \int_{D_4^+} C_4 \ . \tag{1.21}$$

The resulting 4d axion field obeys a shift symmetry, $a_i \to a_i + c$. The number of topologically-inequivalent, orientifold-invariant 4-cycles in a Calabi-Yau manifold is denoted by the Hodge number $h^{1,1}_+$.[8] Hence there are $h^{1,1}_+$ moduli τ_i and the same number of axions a_i, so we can write them as complexified Kähler moduli, $T_i = \tau_i + ia_i$.

To conclude this discussion, let us briefly mention one interesting type of model: the *no-scale model*, which has a Kähler potential of the form

$$K = K_0 - 3\ln\left(T + \overline{T}\right) \ . \tag{1.22}$$

Owing to the shift symmetry of $a = \mathrm{Im}(T)$, it is not possible for the superpotential W to depend on Kähler moduli at the perturbative level due to its holomorphic nature. Hence after we have stabilised the S and U_α moduli, the superpotential takes a constant value, $\langle W \rangle = W_0$.

It can be shown by direct calculation that this model satisfies the relation

$$K^{i\bar{j}} K_i K_{\bar{j}} = 3 \ , \tag{1.23}$$

so the scalar potential (1.20) vanishes and is thus independent of T (hence "no-scale"). In general, the T_i-dependent piece of the Kähler potential can be written in terms of the compactification volume $\mathcal{V}$ as

$$K = -2\ln\mathcal{V} \ . \tag{1.24}$$

Comparing with (1.22), we see that in no-scale models the volume is controlled by the size of a single 4-cycle $\tau = \mathrm{Re}(T)$,

$$\mathcal{V} = \tau^{3/2} \ . \tag{1.25}$$

[8]The (1,1) refers to the fact that these 4-cycles are dual to 2-cycles that each have one holomorphic and one antiholomorphic coordinate, while the + sign refers to their invariance under the orientifold projection.

1.3.3 The LARGE Volume Scenario

We now turn to a phenomenologically powerful model: the LARGE Volume Scenario [8–10]. This scenario is based on an extension of the no-scale model described above, with the addition of at least one small "blow-up" cycle $\tau_{\rm s}$ in addition to the large cycle $\tau_{\rm b}$ (previously τ) that fixes the bulk volume $\mathcal{V}$. This is sometimes known as a "Swiss-cheese model", which is a good visual metaphor for the resulting geometry. The volume takes the form

$$\mathcal{V} = \tau_{\rm b}^{3/2} - \sum_{i=2}^{h_+^{1,1}} \tau_i^{3/2} \ , \tag{1.26}$$

where $\tau_{\rm s}$ is one of the small 4-cycles τ_i, $2 \leq i \leq h_+^{1,1}$. For explicit calculations we will mostly consider a simple toy model with only one small 4-cycle,

$$\mathcal{V} = \tau_{\rm b}^{3/2} - \tau_{\rm s}^{3/2} \ , \tag{1.27}$$

To extract a useful physical model from this setup, two types of quantum corrections must be included. The first is a perturbative correction to the Kähler potential, which modifies (1.24) to

$$K = -2\ln\left(\mathcal{V} + \hat{\xi}\right) \ , \tag{1.28}$$

where $\hat{\xi}$ depends on the string coupling (which is equivalent to the real part of the axio-dilaton S) and the detailed geometry of the particular Calabi-Yau in question. The second correction is the addition of a non-perturbative term to the superpotential,

$$W = W_0 + Ae^{-\alpha T_{\rm s}} \ , \tag{1.29}$$

where A and α are constants that depend on the precise mechanism giving rise to the correction (e.g. gaugino condensation on N D7 branes wrapping $\tau_{\rm s}$ gives $\alpha = 2\pi/N$).

To maintain control over the perturbative corrections, it makes sense to consider a regime in which $\mathcal{V} \gg \hat{\xi} \sim \mathcal{O}(1)$ (which also necessarily implies $\tau_{\rm b} \gg \tau_{\rm s}$). In addition, for this approximation to be valid the moduli τ_i cannot

be too small, so in particular $\exp(-\alpha\tau_{\rm s}) \ll 1$. Expanding the scalar potential to leading order in $\exp(-\alpha\tau_{\rm s})$ and $\mathcal{V}^{-1}$ gives

$$V = \frac{8\alpha^2 A^2 \sqrt{\tau_{\rm s}} e^{-2\alpha\tau_{\rm s}}}{3\mathcal{V}} + \frac{4AW_0\tau_{\rm s}e^{-\alpha\tau_{\rm s}}\cos(\alpha a_{\rm s})}{\mathcal{V}^2} + \frac{3W_0^2\hat{\xi}}{2\mathcal{V}^3} \ . \tag{1.30}$$

Minimising with respect to the axion $a_{\rm s}$ makes the second term negative,

$$V = \frac{8\alpha^2 A^2 \sqrt{\tau_{\rm s}} e^{-2\alpha\tau_{\rm s}}}{3\mathcal{V}} - \frac{4AW_0\tau_{\rm s}e^{-\alpha\tau_{\rm s}}}{\mathcal{V}^2} + \frac{3W_0^2\hat{\xi}}{2\mathcal{V}^3} \ , \tag{1.31}$$

and subsequently minimising with respect to $\mathcal{V}$ and $\tau_{\rm s}$ yields a solution

$$\langle\mathcal{V}\rangle = \frac{3W_0}{4\alpha A}\sqrt{\tau_{\rm s}}e^{\alpha\tau_{\rm s}} \quad , \qquad \langle\tau_{\rm s}\rangle = \hat{\xi}^{2/3} \ . \tag{1.32}$$

This solution is exact in the limit $\mathcal{V} \to \infty$, in which the potential V vanishes to leading order. On the other hand, at large finite volume the first two terms dominate since they scale as $(\ln\mathcal{V})^{3/2}/\mathcal{V}^3$, whereas the last term only scales as $1/\mathcal{V}^3$. Of the first two terms the second has the larger numerical coefficient, so the overall contribution from these two terms is negative. Hence as $\mathcal{V} \to \infty$ the potential (1.31) approaches zero from below, implying that V has a stable minimum at an exponentially large volume.

This large volume is generated dynamically and can be easily achieved without requiring any parameters at the string scale to take on special values. Hence once established, this scenario does not require any fine-tuning. Furthermore, a distinctive spectrum of mass scales is obtained,

$$\begin{aligned} M_{\rm string} &\sim \frac{M_{\rm P}}{\mathcal{V}^{1/2}} \ , \\ m_{\tau_{\rm s}} \sim m_{a_{\rm s}} &\sim \frac{M_{\rm P}\ln\mathcal{V}}{\mathcal{V}} \ , \\ m_{3/2} \sim m_{U_\alpha} \sim m_S &\sim \frac{M_{\rm P}}{\mathcal{V}} \ , \\ m_{\tau_{\rm b}} &\sim \frac{M_P}{\mathcal{V}^{3/2}} \ , \\ m_{a_{\rm b}} &\lesssim M_P\, e^{-2\pi\mathcal{V}^{2/3}} \sim 0 \ . \end{aligned} \tag{1.33}$$

In particular, the volume modulus is hierarchically lighter than all the other moduli except for the volume axion $a_{\rm b}$, which is essentially massless.

The Standard Model matter content can be realised in string models via *soft terms*, which are terms in the Lagrangian that dominate at low energies and break supersymmetry. Such terms can arise from D3 or D7 branes in various configurations, typically giving masses $M_{\text{soft}} \sim M_{\text{P}}/\mathcal{V}$ or smaller [9]. Hence for sufficiently large volumes ($\mathcal{V} \sim 10^8$ or greater depending on the setup), the LARGE Volume Scenario can provide a natural solution to the electroweak hierarchy problem.

1.3.4 Fibred models

To conclude this section, let us explore a simple extension of LVS in which the exponentially large volume is the product of two distinct geometric cycles. Calabi-Yau manifolds with this property can be realised using fibre bundles. The mathematical definition of a fibre bundle is as follows:

Definition. A *fibre bundle* (E, π, B, F, G) is a differentiable manifold E, in conjunction with differentiable manifolds B (the *base space*) and F (the *fibre*), a *projection* $\pi : E \to B$, which is a surjective map of E onto B, and a Lie group G. The total space E is locally the product $B \times F$: for any open covering $\{U_i\}$ of the base manifold B and at each point p on B, there exist local trivialisations $\phi_i(p) : U_i \times F \to \pi^{-1}(U_i)$ such that $\pi \circ \phi_i(p, f) = p$, so ϕ_i^{-1} maps $\pi^{-1}(U_i)$ onto the direct product $U_i \times F$. For any $p \in U_i \cap U_j \neq \emptyset$ there exists a transition function between trivialisations, $t_{ij}(p) \equiv \phi_{i,p}^{-1} \circ \phi_{j,p}$, and the set of all such transition functions defines the *structure group* G.

In other words, a fibre bundle is *locally* the product of two spaces but not necessarily globally; if a fibre bundle is globally $B \times F$, it is known as a *trivial bundle* and all the transition functions t_{ij} can be chosen to be the identity operation.

There exist classes of Calabi-Yau manifolds that have a fibration structure: examples include 4d fibrations over the 2d projective space $\mathbb{P}^1$, where the fibre could be a K3 surface or a 4d torus T^4. The LARGE Volume Scenario can be

realised in such models, which have a compactified Calabi-Yau volume of the form

$$\mathcal{V} = \sqrt{\tau_1}\tau_2 - \sum_{i=3}^{h^{1,1}_+} \tau_i^{3/2} \ . \tag{1.34}$$

In Chapter 3 I will discuss extensively some the phenomenological consequences of these models.

Chapter 2

Dark Radiation in the Minimal LARGE Volume Scenario

2.1 Introduction

The first non-introductory section of this chapter is a continuation of the review from Chapter 1 — the work reviewed here was first presented in [21, 22]. The remainder, mostly in the second half of the chapter, is based on my paper [2], which was written in collaboration with Joseph P. Conlon, Ulrich Haisch and Andrew J. Powell.

In the previous chapter we introduced the LARGE Volume Scenario (LVS) as a promising model-building framework in String Theory. We would now like to study the cosmological history that follows from LVS models, in particular the production of dark radiation in the early Universe. This will enable us to take a leap across the chasm between String Theory and experiment and provide some theoretical predictions that can be tested in the near future.

It is expected based on CMB observations that the early Universe underwent a period of accelerated expansion, known as inflation. In the context of string compactifications, the moduli fields associated with the compactified directions will be displaced from the minimum of the potential during this epoch and will generally get large, non-zero vacuum expectation values (VEVs).[1] When

[1]The displacement is driven by the large inflationary energy density and its coupling to the moduli fields. A large displacement will arise whenever $V_{\rm inf} \gtrsim m^2_{\Phi,{\rm vac}} M_{\rm P}^2$, where $m_{\Phi,{\rm vac}}$ is the vacuum mass of the modulus, and in practice moduli domination will come to occur

inflation ends, these moduli will begin to oscillate about their minima, acquiring a large energy density in the process. The moduli will then begin to decay at a rate proportional to their mass cubed,

$$\Gamma_\Phi \sim \frac{m_\Phi^3}{M_{\rm P}^2} \,. \tag{2.1}$$

The heaviest moduli will decay first — their decay products thermalise and, being much lighter than the moduli, behave as radiation (i.e. relativistic matter). As the Universe expands and cools, the energy density in radiation evolves with the scale factor $a(T)$ as

$$\rho_{\rm radiation} \sim \frac{1}{a(T)^4} \,. \tag{2.2}$$

Each modulus Φ will begin to decay after the temperature of the Universe drops below its mass m_Φ. However, since the modulus decay rate (2.1) is Planck-suppressed, the moduli will remain for a long time thereafter, continuing to oscillate coherently while redshifting as non-relativistic matter,

$$\rho_{\rm matter} \sim \frac{1}{a(T)^3} \,. \tag{2.3}$$

Since $a(T)$ increases with the expansion of the Universe, (2.3) will eventually come to dominate over (2.2), so the Universe will enter a moduli-dominated phase. Furthermore, (2.1) tells us that the lightest moduli have the slowest decay rates and are the last to decay. Meanwhile, the decay products of any early-decaying moduli, being relativistic, will have long since redshifted away. Therefore we conclude that independent of the details of the inflationary mechanism, *the lightest modulus, which is last to decay, will come to dominate the energy density of the universe* — what happens next depends entirely upon the final states into which this modulus can decay.

We can separate the decay products of the lightest modulus into two categories. The first is decays that go to the *visible sector* — that is, decays to

even for very small initial displacements.

the known particles of the Standard Model, or its extensions such as the Minimal Supersymmetric Standard Model (MSSM). The decays to visible matter induce reheating, after which the standard hot Big Bang cosmology follows. In addition, there may also be decays to *hidden sector* states. In the context of string compactifications these could be other localised matter sectors, separated in the compact geometry from the Standard Model, as well as bulk states that extend throughout the compactified volume — in particular the hidden sector contains any candidates for dark radiation, such as massless axions or light hidden gauge bosons. The key point is that the amount of dark radiation obtained is completely fixed by the decay rates of the lightest modulus into each of its decay channels.

The LARGE Volume Scenario is an appealing framework in which to address the issue of dark radiation. In particular, LVS is tractable to analyse because it has a unique lightest modulus: the volume modulus Φ, which is parametrically lighter than any other modulus.[2] As argued above, the presence of a single lightest Planck-coupled modulus then implies that within these models reheating should be driven by decays of the volume modulus, independent of the details of the high-scale inflationary model. This is attractive as, being the volume modulus, the majority of its couplings are calculable in a model-independent fashion.

In constructing a viable model, there are some important considerations. First of all, we would like to ensure that decays to the visible sector are kinematically viable, in order to induce reheating. Another significant issue is the following: if the reheating temperature is below $\sim 1\,\mathrm{MeV}$, it becomes impossible to reproduce the successful predictions of Big Bang Nucleosynthesis. This is known as the Cosmological Moduli Problem [25–27]; avoiding it requires all moduli to have masses $\gtrsim 30\,\mathrm{TeV}$. We can solve both of these issues and pre-

[2]We will use τ_b to describe the volume modulus in a string compactification context; however we will use Φ to denote the canonically-normalised form of this modulus that decays in the early Universe. The need for this distinction will become clearer in the next section.

serve TeV-scale supersymmetry by assuming the visible sector is *sequestered*, so that all supersymmetry-breaking soft terms are at a scale [28]

$$M_{\rm soft} \sim \frac{M_{\rm P}}{\mathcal{V}^2} \ . \tag{2.4}$$

One way to achieve this is to build the Standard Model on spacetime-filling D3 branes that are located at a singularity in the compact geometry.

If we follow this prescription, it turns out that there are two important couplings. The first is to the volume axion a_b, which is a hidden-sector state so the corresponding decay channel $\Phi \to a_b a_b$ gives rise to dark radiation. The second coupling is to the bilinear $H_u H_d$ of Higgs fields. This interaction leads to the only competitive visible-sector decay mode, $\Phi \to H_u H_d$, and induces the reheating of the Universe. The corresponding coupling Z is an undetermined constant with a natural value of $\mathcal{O}(1)$ at the string scale $M_{\rm string}$. However, if the Higgs sector has an exact shift symmetry (see for example [29, 30] for explicit string theory constructions of such a symmetry), then Z is fixed to 1 at $M_{\rm string}$. The case of a shift-symmetric Higgs sector with pure MSSM matter content is then completely defined and predictive. We will refer to this specific LVS as Minimal LVS (MLVS).

Let us make some general comments on the cosmology implicit this model. Since reheating arises from modulus decays, reheating occurs at a temperature $T_{\rm rh} \sim 1\,{\rm GeV}$. Low reheating temperatures are common to all models of SUSY breaking once they are embedded into string theory and moduli are included in the spectrum. Since the temperature is lower than the decoupling temperature of weakly interacting massive particles (WIMPs), the conventional freeze-out calculation of MSSM neutralino dark matter (DM) becomes invalid. WIMP DM can however still be produced, for instance via non-thermal production in modulus decays. Another natural DM candidate is axions, for which late modulus decays dilute the axion DM abundance and allow higher values of the axion decay constant f_a than in a conventional cosmology. A potentially more serious problem is the compatibility of baryogenesis with low-scale reheating.

While this is beyond the scope of this thesis, note that Affleck-Dine baryogenesis has been argued to give acceptable baryon asymmetries even for low reheating temperatures [31].

This chapter is structured as follows. In the next section I review the tree-level calculation of $\Delta N_{\rm eff}$ performed in [21, 22]. Following that, in section 2.3 I motivate the need to consider loop corrections, for which I calculate the appropriate loop diagrams in section 2.4. In section 2.5 I present the results of a numerical simulation of the running couplings, and I conclude this chapter by discussing the consequences for $\Delta N_{\rm eff}$ in section 2.6.

2.2 The leading contribution

We will now compute the branching ratios of the volume modulus decay modes in MLVS. Our starting point is the simple LARGE-volume model presented in Chapter 1, in which the compactification volume takes the form

$$\mathcal{V} = \tau_{\rm b}^{3/2} - \tau_{\rm s}^{3/2} \ . \tag{2.5}$$

Decay to the light axion $a_{\rm b}$ takes place primarily through the supergravity kinetic terms for the Kähler moduli, which from (1.19) are

$$\mathcal{L} \supset -K_{i\bar{j}} \partial_\mu T^i \partial^\mu \overline{T}^{\bar{j}} \ . \tag{2.6}$$

The modulus $\tau_{\rm s}$ parametrising the small blow-up 4-cycle will give a sub-leading contribution, so we can neglect it in what follows. This approximation reduces the Kähler potential to that of a simple no-scale model,

$$\begin{aligned} K &= K_0 - 2\ln \mathcal{V} \\ &= K_0' - 3\ln\left(T_{\rm b} + \overline{T}_{\rm b}\right) \ , \end{aligned} \tag{2.7}$$

where $T_{\rm b} \equiv \tau_{\rm b} + i a_{\rm b}$. Inserting this into (2.6) gives kinetic terms,

$$\mathcal{L} = \frac{3}{4\tau_{\rm b}^2} \partial_\mu \tau_{\rm b} \partial^\mu \tau_{\rm b} + \frac{3}{4\tau_{\rm b}^2} \partial_\mu a_{\rm b} \partial^\mu a_{\rm b} \ . \tag{2.8}$$

In order to extract physical predictions these need to be expressed in standard form, which necessitates the reparametrisation

$$\tau_{\rm b} = \sqrt{\frac{3}{2}} \ln \Phi \quad , \qquad a_{\rm b} \to \sqrt{\frac{2}{3}} a_{\rm b} \; . \tag{2.9}$$

Using this in (2.8) gives the *canonically normalised* terms

$$\mathcal{L} = \frac{1}{2} \partial_\mu \Phi \partial^\mu \Phi + \frac{1}{2} e^{-2\sqrt{\frac{2}{3}}\Phi} \partial_\mu a_{\rm b} \partial^\mu a_{\rm b} \; . \tag{2.10}$$

Expanding out the exponential reveals the dimension-5 operator

$$\mathcal{L}_{\Phi \to a_{\rm b} a_{\rm b}} = -\frac{2}{\sqrt{6} M_{\rm P}} \Phi \partial_\mu a_{\rm b} \partial^\mu a_{\rm b} \; , \tag{2.11}$$

where we have restored the dependence on $M_{\rm P}$ for clarity.

Since the axion $a_{\rm b}$ is massless, the decay channel $\Phi \to a_{\rm b} a_{\rm b}$ is kinematically open. We can compute the decay rate using the standard formula from quantum field theory,

$$\Gamma = \frac{1}{S} \int d\Gamma \quad , \qquad d\Gamma = \frac{1}{2E_{\rm in}} \left| \mathcal{T} \right|^2 d{\rm LIPS}_2(k_{\rm in}) \; . \tag{2.12}$$

Here $k_{\rm in}$ and $E_{\rm in}$ are the 4-momentum and energy of the initial particle, S is a symmetry factor that counts the number of identical particles in the final state (in this case $S = 2! = 2$), $\mathcal{T}$ is the matrix element of the decay process and $d{\rm LIPS}_2$ is the 2-particle Lorentz-invariant phase space measure,

$$d{\rm LIPS}_2(k) = \frac{1}{4(2\pi)^2 E_1' E_2'} \delta^4(k - k_1' - k_2') d^3k_1' d^3k_2' \; . \tag{2.13}$$

In the present case $E_{\rm in} = m_\Phi$ and $E_1' = E_2' \equiv E_a$ in the CM frame, so equation (2.12) simplifies to

$$\Gamma = \frac{1}{S} \frac{\left| \mathcal{T} \right|^2}{16\pi m_\Phi} = \frac{\left| \mathcal{T} \right|^2}{32\pi m_\Phi} \; . \tag{2.14}$$

Meanwhile, the momentum-space matrix element associated with (2.11) is

$$\mathcal{T} = \left(\frac{2}{\sqrt{6} M_{\rm P}} \right) 2 \left(k_1' \cdot k_2' \right) = -\frac{2 m_\Phi^2}{\sqrt{6} M_{\rm P}} \; , \tag{2.15}$$

so the total decay rate to axions is

$$\Gamma_{\Phi\to a_{\rm b}a_{\rm b}} = \frac{1}{48\pi}\frac{m_\Phi^3}{M_{\rm P}^2}\ . \tag{2.16}$$

The dominant visible-sector decay channel is the decay to Higgs bosons. In the MSSM there are two Higgs doublets, H_u and H_d.[3] Each of these is a two-component complex field, so there are 8 degrees of freedom altogether. The decay rate can be derived by including the matter contribution to the Kähler potential,

$$K = K_0' - 3\ln\left(T_{\rm b}+\overline{T}_{\rm b}\right) + \frac{H_u\overline{H}_u + H_d\overline{H}_d + (Z H_u H_d + \text{h.c.})}{\left(T_{\rm b}+\overline{T}_{\rm b}\right)}\ . \tag{2.17}$$

The important terms in the canonically-normalised Lagrangian are

$$\begin{aligned}\mathcal{L} \supset\ & \frac{1}{2}\partial_\mu\Phi\partial^\mu\Phi + \partial_\mu H_u\partial^\mu\overline{H}_u + \partial_\mu H_d\partial^\mu\overline{H}_d \\ & + \frac{1}{\sqrt{6}M_{\rm P}}\left[\Phi\left(H_u\Box\overline{H}_u + H_d\Box\overline{H}_d\right) + (Z\,H_uH_d\Box\Phi + \text{h.c.})\right]\ .\end{aligned} \tag{2.18}$$

The dominant contribution to the decay of Φ comes from the Giudice-Masiero coupling $Z H_u H_d \Box\Phi$ [32], as all other couplings are mass-suppressed (since for on-shell processes, $\Box H = m_H^2 \ll m_\Phi^2$). Taking care to add up the partial widths from each of the four decay channels encompassed by this interaction (since each field is a complex doublet), we get

$$\Gamma_{\Phi\to H_uH_d} = \frac{2Z^2}{48\pi}\frac{m_\Phi^3}{M_{\rm P}^2}\ . \tag{2.19}$$

Let us briefly consider other possible visible-sector decay channels. Other scalars have an interaction Lagrangian similar to (2.18) but without the Giudice-Masiero piece, so the decay to scalars is mass-suppressed. Decays to fermions have a similar suppression because the appropriate terms always include the

[3]Two Higgs fields are required because in a supersymmetric model, each is the scalar component of a chiral superfield. Hence there is also a fermionic component (the higgsino), and chiral fermions are consistent only if they are free of *anomalies*. The anomaly coefficient is proportional to the gauge charge cubed, and since the Higgs field has non-trivial electroweak charge there needs to be an additional doublet, with equal and opposite charge, to cancel the anomaly.

chiral operator $\bar{\chi}\bar{\sigma}^{\mu}D_{\mu}\chi$, which vanishes on-shell. The gauge bosons will interact with Φ via their gauge kinetic function. Since the Standard Model is localised at a singularity while the volume modulus is a bulk field, decays to gauge bosons will be volume-suppressed (in practice the dominant contribution will arise at loop level). Hence in the MLVS, where we consider only the volume axion $a_{\rm b}$ as a source of dark radiation, the ratio of branching ratios of visible-sector and hidden-sector decays is simply given by [21, 22]

$$\frac{\mathrm{B}_a}{\mathrm{B}_{\rm SM}} = \frac{\mathrm{Br}(\Phi \to a_b a_b)}{\mathrm{Br}(\Phi \to H_u H_d)} = \frac{1}{2Z^2} \,, \tag{2.20}$$

where the coupling Z is understood to be normalised at the mass m_{Φ} of the volume modulus.

In terms of (2.20) the excess effective number of neutrinos is given by (1.16),

$$\Delta N_{\rm eff} = \frac{43}{7}\left(\frac{10.75}{g_*(T_{\rm rh})}\right)^{1/3}\frac{1}{2Z^2} \,. \tag{2.21}$$

This has a weak dependence on the effective number of thermal degrees of freedom at the time of reheating. For TeV-scale supersymmetry we require $m_{\Phi} \simeq 5 \times 10^6\,\mathrm{GeV}$, from which it follows that the reheating temperature is $T_{\rm rh} \sim m_{\Phi}^{3/2}/M_{\rm P}^{1/2} \sim 1\,\mathrm{GeV}$. This implies a slight ambiguity in $g_*(T_{\rm rh})$, since its value depends upon whether the b quarks, c quarks and τ leptons are still thermalised ($g_*(T_{\rm rh}) = 86.25$) or not ($g_*(T_{\rm rh}) = 61.75$). Hence there is a small uncertainty in the amount of dark radiation predicted,

$$\frac{1.53}{Z^2} \,\leq\, \Delta N_{\rm eff} \,\leq\, \frac{1.72}{Z^2} \,. \tag{2.22}$$

At tree level in the MLVS one has $Z(m_{\Phi}) = Z(M_{\rm string}) = 1$, which implies that $\Delta N_{\rm eff} \simeq 1.6$. On the other hand, the measured values of $N_{\rm eff}$ require $\Delta N_{\rm eff} \lesssim 0.95$ at the 95% confidence level, which translates into $Z \gtrsim 1.3$.

2.3 Looking beyond tree-level

The MLVS tree-level prediction for $\Delta N_{\rm eff}$ would appear to be in tension with observation. However, the shift symmetry that fixes $Z = 1$ is defined at the

compactification scale — even if the Higgs sector is exactly shift symmetric at this scale, this symmetry is broken at lower energies by the gauge and Yukawa couplings. In consequence, the coupling Z will receive logarithmically-enhanced quantum corrections of the form $1/(4\pi)\ln(M_{\rm string}/m_\Phi)$ from MSSM loop diagrams. In view of the large hierarchy $M_{\rm string} \gg m_\Phi$, the resulting terms can be of $\mathcal{O}(1)$ and have to be resummed using renormalisation group (RG) techniques. An immediate question then arises as to whether the induced radiative corrections are large enough to make the MLVS compatible with the measurements of $N_{\rm eff}$, which call for $Z(m_\Phi) \gtrsim 1.3$. Our goal in the rest of this chapter is to answer this question.

Before turning to the calculation of the anomalous dimension of the coupling Z that determines the relative amount of dark radiation via (2.20), let us emphasise the main assumptions that enter our analysis. First, the general spectrum of moduli masses is set by the LVS (1.33). Second, the volume modulus is displaced from its eventual minimum during inflation. Given this, the volume modulus will come to dominate the energy density of the Universe and thereby drive reheating. Third, the spectrum of SUSY breaking soft terms has the sequestered form (2.4) [28]. In what follows, we will assume that the level of volume sequestering is the same for both scalar and gaugino masses, so that $M_{\rm soft} \sim m_0 \sim m_{1/2} \sim M_{\rm P}/\mathcal{V}^2$. Hence to solve the gauge hierarchy problem, i.e. $M_{\rm soft} \sim 1\,\text{TeV}$, one needs $\mathcal{V} \sim 5\times 10^7$. For the hierarchy of scales in LVS (1.33), this results in in $M_{\rm string} \sim 3\times 10^{14}\,\text{GeV}$ and $m_\Phi \sim 7\times 10^6\,\text{GeV}$.

2.4 Analytic results

2.4.1 Volume modulus interactions

The interaction terms in the LVS Lagrangian that give rise to the leading decay modes of the volume modulus, i.e. $\Phi \to a_b a_b$ and $\Phi \to H_u H_d$, are

$$\mathcal{L} \supset \frac{2}{\sqrt{6}M_{\rm P}}\left(\partial_\mu a_b\right)^2\Phi + \frac{1}{\sqrt{6}M_{\rm P}}\left[Z\,H_u H_d \Box\Phi + \text{h.c.}\right], \tag{2.23}$$

where $H_u H_d = \epsilon_{ij} H_u^i H_d^j = H_u^+ H_d^- - H_u^0 H_d^0$ represents the usual contraction between $\mathrm{SU}(2)_L$ doublets and all fields are understood to be canonically normalised. While the presence and the form of the $\Phi a_b a_b$ and $\Phi H_u H_d$ couplings in (2.23) are robust predictions of the LVS [21, 22], in generic models further contributions to the volume modulus decays into the hidden and visible sector may arise. Contributions of the former type can come, e.g., from local closed string axions, but since such decays represent dark radiation they will always enhance the ratio of branching ratios (2.20), worsening the tension between theory and experiment. Thus we will not consider additional hidden-sector contributions beyond $\Phi \to a_b a_b$ in this analysis.

2.4.2 Running of the volume modulus Higgs coupling

In contrast to the $\Phi a_b a_b$ coupling, which receives only Planck-suppressed corrections, the $\Phi H_u H_d$ coupling is modified by the virtual exchange of MSSM particles. As a result the interaction strength Z entering (2.23) will evolve logarithmically from M_{string} to m_Φ, where the volume modulus decays. The scale dependence of Z is determined by the Renormalisation Group (RG) equation

$$\frac{\mathrm{d}}{\mathrm{d}t} Z = \gamma_Z Z \ , \tag{2.24}$$

where $t \equiv \ln(Q/Q_0)$ with Q denoting the renormalisation scale and Q_0 a reference scale, and γ_Z is the corresponding anomalous dimension.

Since the $\Phi H_u H_d$ coupling arises from the Kähler potential and the volume modulus field itself does not renormalise, the anomalous dimension γ_Z can be written in terms of Higgs wavefunction renormalisations only (as a consequence of the supersymmetric non-renormalisation theorem [33]). One obtains

$$\gamma_Z = \gamma_{H_u} + \gamma_{H_d} \ , \tag{2.25}$$

where γ_{H_u} and γ_{H_d} are the anomalous dimensions of the Higgs superfields. To verify the correctness of (2.25), we have calculated the one-loop correction

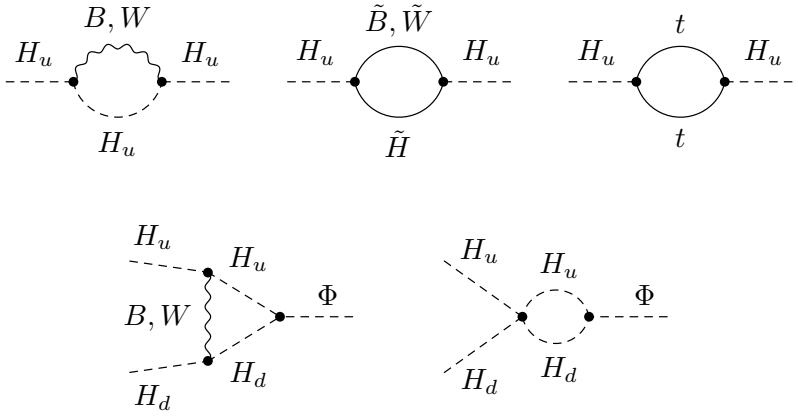

Figure 2.1: The $H_u H_u$ self-energy diagrams (upper row) and $\Phi H_u H_d$ vertex diagrams (lower row) that contribute to the one-loop anomalous dimension $\gamma_Z^{(1)}$. The $H_d H_d$ self-energy diagrams needed to determine the wave-function renormalisation factor of H_d are not shown.

$\gamma_Z^{(1)}$ to the anomalous dimension γ_Z explicitly. The corresponding Feynman diagrams are depicted in figure 2.1.

Let us explain the procedure involved in the calculation. First of all, one must compute the Feynman diagrams of figure 2.1 using the machinery of quantum field theory. Since unitarity requires us to sum over all possible intermediate states, we must therefore integrate over all possible values of the loop momenta. Naively, in many cases (such as the present case) this gives an infinite result. However, this is merely a consequence of the fact that the strengths of the interactions involved (the couplings) change with energy scale; furthermore we know that the Standard Model/MSSM is only valid up to some energy scale less than the Planck scale $M_{\rm P}$, so it actually makes no sense to integrate up to infinite loop momentum. By allowing the interaction strengths to vary with energy scale, we can cancel the divergent pieces of the loop diagrams order-by-order in perturbation theory.

The solution, then, is to turn a problem (an infinite answer) into an opportunity — the coefficient of the divergent piece of each diagram gives crucial information about the running of the couplings that is required to get a finite

answer for all physically observable quantities. The final step is to parametrise our initial (incorrect) assumption that all couplings are independent of energy scale — in the present case,

$$\frac{\mathrm{d}}{\mathrm{d}t} Z_{\mathrm{bare}} = 0 \,. \tag{2.26}$$

We now have a complete map between scale-independent "bare" parameters and scale-dependent "renormalised" parameters, which allows us to translate the divergent pieces of loop diagrams into the anomalous dimension γ_Z.

We performed the calculation of the self-energy and vertex diagrams using dimensional regularisation with modified minimal subtraction (i.e. the $\overline{\mathrm{DR}}$ scheme). The contributions to the scalar fields $H_{u,d}$ were computed in Wess-Zumino gauge, retaining an arbitrary R_ξ gauge for the vector fields.[4] While both classes of diagrams are individually gauge dependent, the ξ dependence cancels in the sum of contributions. Our results for the individual diagrams agree with those given in [34–36]. Keeping only the third-family Yukawa couplings $y_{t,b,\tau}$, we obtain the one loop result[5]

$$\gamma_Z^{(1)} = \frac{1}{(4\pi)^2}\left[-\frac{3g_1^2}{5} - 3g_2^2 + 3|y_t|^2 + 3|y_b|^2 + |y_\tau|^2\right] \,, \tag{2.27}$$

which equals the sum $\gamma_{H_u}^{(1)} + \gamma_{H_d}^{(1)}$ of one-loop superfield anomalous dimensions as given e.g. in the review [37]. Here the couplings g_1 and g_2 are given in terms of the conventional $\mathrm{U}(1)_Y$ and $\mathrm{SU}(2)_L$ SM gauge couplings by $g_1 = \sqrt{5/3}\, g'$ and $g_2 = g$, respectively.

Employing the one-loop anomalous dimension (2.27) to solve the RG equation (2.24), we find to leading logarithmic accuracy

$$\begin{aligned} K \equiv \frac{Z(m_\Phi)}{Z(M_{\mathrm{string}})} &\simeq 1 - \gamma_Z^{(1)} \ln\left(\frac{M_{\mathrm{string}}}{m_\Phi}\right) \\ &\simeq 1 - \frac{18}{(4\pi)^2}\left(-1.7 + \frac{1.5}{\sin^2\beta} + \frac{1.6\cdot 10^{-4}}{\cos^2\beta}\right) \,. \end{aligned} \tag{2.28}$$

[4] Note that in Wess-Zumino gauge SUSY is broken, which explains the need to compute vertex diagrams.

[5] For a detailed look at the calculation, see Appendix A.

To arrive at the numerical expression we have employed $g_1(M_{\rm string}) \simeq 0.65$, $g_2(M_{\rm string}) \simeq 0.69$, $y_t(M_{\rm string}) \simeq 0.70/\sin\beta$, $y_b(M_{\rm string}) \simeq 6.0 \times 10^{-3}/\cos\beta$ and $y_\tau(M_{\rm string}) \simeq 7.2 \times 10^{-3}/\cos\beta$, corresponding to $M_{\rm string} = 3 \times 10^{14}\,{\rm GeV}$ and $m_\Phi = 7 \times 10^6\,{\rm GeV}$.[6] In the final result in (2.28), we have shown the contributions arising from the terms $g_{1,2}^2$, $|y_t|^2$ and $|y_{b,\tau}|^2$ separately.

The different overall signs multiplying the contributions from the gauge and the Yukawa couplings imply that the individual terms in (2.27) tend to cancel. The relative magnitude of the different Yukawa couplings is set by the ratio of the Higgs vacuum expectation values, $\tan\beta$. In fact, the semi-analytic expression for $\gamma_Z^{(1)}$ used in (2.28) is less than 0 for $3 \lesssim \tan\beta \lesssim 35$ and vice versa. Hence we expect to find that loop corrections suppress (enhance) the partial decay rate $\Gamma(\Phi \to H_u H_d)$ for small and large (moderate) $\tan\beta$. However, in order to obtain a reliable prediction for K, the large logarithm appearing in (2.28) has to be resummed by solving (2.24) together with the RG equations describing the scale dependence of the gauge and Yukawa couplings.

2.5 Numerical results

Having presented the analytic result for the anomalous dimension of the Guidice-Masiero coupling Z in the previous section, we now turn to the numerical RG analysis of the $\Phi \to H_u H_d$ decay mode. Our methodology is detailed in the following.

2.5.1 Solution of RG equations

The system of differential equations describing the renormalisation scale dependence of the coupling strength Z as well as those of the gauge and Yukawa couplings is solved iteratively with the help of SoftSusy 3.3.7 [38]. We perform the calculation including all relevant one-loop and two-loop effects.[7]

[6] These values for the couplings have been obtained using the numerical procedure outlined in Section 2.5.1.

[7] However, two-loop effects have a very minor impact on the analysis, so we have presented only the result of the one-loop anomalous dimension $\gamma_Z^{(1)}$ in (2.27).

In order to constrain the RG evolution at low energies we use the following SM inputs: the fine structure constant $\alpha(m_Z) = 1/127.973$; the Fermi constant $G_F = 1.16637 \times 10^{-5}\ \mathrm{GeV}^{-2}$; the strong coupling $\alpha_s(m_Z)$; the pole mass m_t of the top quark; the bottom mass $m_b = 4.2\,\mathrm{GeV}$; and the tau mass $m_\tau = 1.777\,\mathrm{GeV}$. These low-energy boundary conditions were applied at the Z-boson mass $m_Z = 91.1875\,\mathrm{GeV}$.

At the string scale M_{string} we impose *minimal supergravity* (MSUGRA) boundary conditions, which leave just five free SUSY parameters: common scalar and gaugino masses, m_0 and $m_{1/2}$; universal trilinear terms A_0; the bilinear soft SUSY breaking term B; and the SUSY μ parameter. Following common practice, we employ the one-loop corrected electroweak symmetry breaking (EWSB) conditions (see e.g. [39]) to trade B and the magnitude $|\mu|$ in favour of $\tan\beta$ and the sign of μ. Notice that the assumed scaling of $m_0 \sim m_{1/2} \sim M_{\mathrm{P}}/\mathcal{V}^2$ naturally requires $B \sim M_{\mathrm{P}}^2/\mathcal{V}^4$ and $\mu \sim M_{\mathrm{P}}/\mathcal{V}^2$ to achieve EWSB. We assume that these scalings are realised by an appropriate volume sequestering, and furthermore we take $A_0 \sim M_{\mathrm{P}}/\mathcal{V}^2$. The SUSY scale is determined by the geometric mean $M_{\mathrm{soft}} \equiv \sqrt{m_{\tilde{t}_1} m_{\tilde{t}_2}}$ of the masses $m_{\tilde{t}_{1,2}}$ of the stop mass eigenstates. Finally, the mass of the volume modulus is obtained from $m_\Phi = M_{\mathrm{string}}^3/M_{\mathrm{P}}^2$.

2.5.2 SM and MSUGRA parameter dependencies

Before studying the dependencies of (2.28) on the MSUGRA parameters, we consider the impact of the parametric SM errors. The dominant sources of SM uncertainties arise from the top mass and the strong coupling constant. This is to be expected because (2.27) is quadratic in the top Yukawa coupling and the RG evolution of y_t depends sensitively on the low-energy initial conditions for m_t and α_s. The world average of the strong coupling evaluated at the Z-boson mass is $\alpha_s(m_Z) = 0.1184 \pm 0.0007$ [40]. This value is obtained from a large set of measurements with significant spreads between them, so to account for this

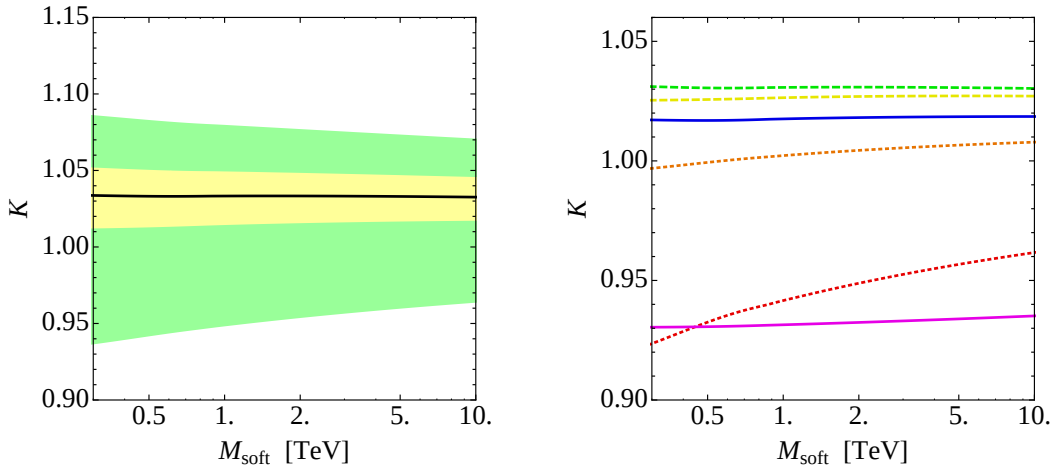

Figure 2.2: Left: Predictions for K for fixed MSUGRA input. The solid black line indicates the result obtained for the central choice of SM inputs while the coloured bands reflect the uncertainties associated with the errors in the top mass and the strong coupling constant. Right: Predictions for K for different values of $\tan\beta$. See text for further explanations.

fact we will also give results employing the 3σ error ± 0.0021 of the α_s world average.

The more critical ingredient is the top mass, for which the latest Tevatron measurements find $m_t = (173.2 \pm 0.9)\,\text{GeV}$ [41]. However, the exact meaning of the mass parameter measured by CDF and D0 via a kinematical reconstruction of the top decay products and comparison to Monte Carlo simulations is unclear and so is its connection to y_t. A theoretically well-defined determination of m_t can, on the other hand, be obtained from the total cross section for top-quark pair production. While such extractions (see e.g. [42]) give values for m_t that are compatible with the mass determinations from direct reconstruction, the achieved accuracy is notably worse, with an uncertainty of around $\pm 5\,\text{GeV}$.

2.5.3 Results

Our predictions for K as a function of $M_{\rm soft}$ are shown in figure 2.2. The results displayed in the left panel correspond to $m_0 = m_{1/2} = A_0$, $\tan\beta = 10$ and $\text{sign}\,\mu = +1$. Almost identical predictions are obtained for different choices of A_0 and $\text{sign}\,\mu = -1$. The solid black curve corresponds to $m_t = 173.2\,\text{GeV}$ and

$\alpha_s(m_Z) = 0.1184$, while the yellow (green) band has been obtained by varying m_t and $\alpha_s(m_Z)$ by $\pm 0.9\,\text{GeV}$ and ± 0.0007 ($\pm 5\,\text{GeV}$ and ± 0.0021) around their central values. The results show that the ratio (2.28) is largely independent of the SUSY scale M_{soft}, but that the exact value of K depends to some extent on the low-energy input m_t and $\alpha_s(m_Z)$. Numerically, we find that the variations of $\pm 0.9\,\text{GeV}$ and ± 0.0007 ($\pm 5\,\text{GeV}$ and ± 0.0021) lead to shifts in K of less than $\pm 2\%$ $\left(^{+5\%}_{-10\%}\right)$ relative to the central values. The largest value of (2.28) is thereby attained for the smallest value of m_t and the largest value of $\alpha_s(m_Z)$, and vice versa.

We now analyse the dependence of K on the choice of $\tan\beta$. Our numerical results are shown in the right panel of figure 2.2. All curves have been obtained for $m_0 = m_{1/2} = A_0$, $\text{sign}\,\mu = +1$, $m_t = 173.2\,\text{GeV}$ and $\alpha_s(m_Z) = 0.1184$. The dotted red, dotted orange, dashed yellow, dashed green, solid blue and solid magenta lines correspond to $\tan\beta = 2, 3, 5, 15, 25$ and 50, respectively. As anticipated, we find that for $\tan\beta \lesssim 3$ the predictions for the ratio (2.28) are below 1, while for moderate values of $\tan\beta$ one obtains ratios above 1. In fact, the values of K saturate for $\tan\beta \simeq 10$, and increasing $\tan\beta$ further leads to a suppression of the ratio $\big($a feature that is also reproduced by the simple formula (2.28)$\big)$. For large $\tan\beta$ values, the ratio K then ends up below 1. We see furthermore that varying $\tan\beta$ in the range $[2, 50]$ shifts K by only $^{+3\%}_{-7\%}$ away from 1. The dependencies on the other MSUGRA parameters are even less pronounced than that on $\tan\beta$.

2.5.4 Prediction for the excess effective number of neutrinos

It is well-known that the mass m_h of the Higgs boson puts stringent constraints on the MSUGRA parameter space — a feature that has become especially relevant since the discovery of a relatively heavy Higgs-like state with a mass of around 126 GeV by ATLAS [43] and CMS [44]. This feature can easily be understood by recalling the classic MSSM result for m_h [45, 46], which includes

the dominant one-loop contributions arising from an incomplete cancellation of top-quark loops and top-squark loops. It reads

$$m_h^2 \simeq m_Z^2 \cos^2(2\beta) + \frac{3 G_F m_t^4}{\sqrt{2}\pi^2}\left[\ln\left(\frac{M_{\rm soft}^2}{m_t^2}\right) + \frac{X_t^2}{M_{\rm soft}^2}\left(1 - \frac{X_t^2}{12 M_{\rm soft}^2}\right)\right] , \quad (2.29)$$

where $X_t \equiv A_t - \mu \cot\beta$ denotes the stop-mixing parameter and A_t is the trilinear stop-Higgs coupling. The first term in (2.29) encodes the tree-level contribution to the squared mass of the Higgs and is maximised for $\tan\beta \to \infty$, while the second term approximates the one-loop corrections and is maximised for $X_t = \pm\sqrt{6} M_{\rm soft}$ (known as maximal mixing).

We assess the impact of the LHC measurements of the Higgs mass on the predictions for $\Delta N_{\rm eff}$ by performing a global scan in the MSUGRA parameter space. Only points that lead to $m_h \in [123, 129]\,\text{GeV}$ are retained, which is the range allowed by the ATLAS and CMS data [43,44] if one accounts for the theoretical uncertainties in the MSSM calculation of the Higgs mass (see e.g. [47]). We generate a large sample of points, allowing the MSUGRA parameters to take random values within $m_{0,1/2} \in [0.1, 10]\,\text{TeV}$, $A_0 \in [-30, 30]\,\text{TeV}$ and $\tan\beta \in [1, 60]$, while permitting μ to be of either sign. In order to incorporate SM uncertainties we let the top mass and the strong coupling constant float within $m_t = (173.2 \pm 5)\,\text{GeV}$ and $\alpha_s(m_Z) = 0.1184 \pm 0.0021$ respectively.

The allowed range of $\Delta N_{\rm eff}$ as a function of $M_{\rm soft}$ is then found from the minimal and maximal $\Delta N_{\rm eff}$ values that are consistent with the tree-level result [21],

$$3.06\,\kappa \leq \Delta N_{\rm eff} \leq 3.43\,\kappa , \quad (2.30)$$

where $\kappa \equiv \text{B}_a/\text{B}_{\rm SM} = 1/(2K^2 Z (M_{\rm string})^2)$ is calculated for each point. Recall that the two-sided bound (2.30) takes into account the uncertainty associated with the value of the reheating temperature. Since we effectively scan over all individual sources of uncertainties, the derived limits on $\Delta N_{\rm eff}$ should be considered very conservative.

Our results of the MSUGRA scan are shown in figure 2.3. The accessible parameter range before (after) imposing the Higgs-mass constraint is indicated

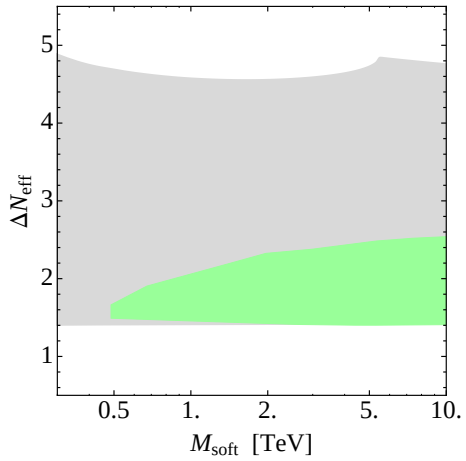

Figure 2.3: Predictions for the excess effective number of neutrino species in the MLVS framework. The coloured wedge-shaped region indicates the possible values of $\Delta N_{\rm eff}$ consistent with the LHC measurements of a Higgs-like state near 126 GeV. For comparison the accessible parameter space without imposing the Higgs constraint is underlaid in grey. For further details see text.

by the grey (coloured) region. We see that in the MLVS the values for $\Delta N_{\rm eff}$ compatible with the m_h constraint lie in the narrow range of about $[1.4, 2.6]$ for $M_{\rm soft} \lesssim 10\,\text{TeV}$, while the upper bound of the allowed region has only a weak, logarithmically-suppressed dependence on $M_{\rm soft}$. The constraint due to the Higgs mass influences the predictions for $\Delta N_{\rm eff}$ only indirectly by narrowing down the possible values of $M_{\rm soft}$ and $\tan\beta$. This effect is most visible for $M_{\rm soft} \lesssim 2\,\text{TeV}$, since such relatively low values of $M_{\rm soft}$ require large values of $\tan\beta$ to push the Higgs mass up to around 126 GeV. This feature is easy to understand from (2.29) and explains why the lower $\Delta N_{\rm eff}$ bound of 1.4 cannot be saturated for $M_{\rm soft}$ below 2 TeV. Notice also that the constraint from m_h cuts away the parts of the parameter space with $\Delta N_{\rm eff} \gtrsim 2.6$ and $M_{\rm soft} \lesssim 0.5\,\text{TeV}$. These regions are inaccessible because they correspond to either $\tan\beta \lesssim 2$ or to too light a stop spectrum. We expect that other low-energy constraints (such as e.g. flavour physics) have an even smaller impact on the limits obtained for $\Delta N_{\rm eff}$ than m_h.

The latest Planck measurement of $N_{\rm eff}$ [11] with (without) the constraint from H_0 [15] gives $\Delta N_{\rm eff} = 0.57 \pm 0.25$ ($\Delta N_{\rm eff} = 0.25 \pm 0.27$). Deviations of $N_{\rm eff}$

in the same ballpark are also found by ACT [12], SPT [13], and WMAP [14]. The minimal value of $\Delta N_{\rm eff} \simeq 1.4$ that is attainable in the MLVS thus corresponds to a discrepancy of about 3.3σ (4.2σ) between theory and experiment. These findings basically rule out the MLVS as a model of dark radiation.

2.6 Summary

The Planck results have ushered in a new era of precision cosmology. Although these measurements support the standard ΛCDM cosmological model, they still leave room for the presence of dark radiation corresponding to about half an extra neutrino species. Other recent experimental determinations of $N_{\rm eff}$ by WMAP, ACT and SPT are within errors all in agreement with the number reported by Planck.

In light of these developments, in this chapter we have analysed dark radiation in the context of sequestered LARGE Volume Scenarios. In this class of models, additional contributions to the excess effective number of neutrinos are an unavoidable consequence of the presence and interactions of a light volume modulus Φ: decays of this field to the visible sector drive reheating of the Universe after inflation, while dark radiation arises from its decays to an ultralight axion partner a_b. The only visible-sector decay mode that can compete with the axion channel is the decay into Higgs pairs induced by a Giudice-Masiero term. The interplay between the two channels $\Phi \to a_b\, a_b$ and $\Phi \to H_u H_d$ fixes the relative fraction of dark radiation uniquely in terms of the coupling strength Z between Φ and the bilinear $H_u H_d$. Assuming MSSM matter content and that the coupling Z is set to 1 at the string scale by means of a shift-symmetric Higgs sector, the ratio of branching ratios of visible-sector and hidden-sector decays can be predicted accurately. At tree level such a calculation leads to $\Delta N_{\rm eff} \simeq 1.6$, at variance with observation.

Unlike the coupling of the volume modulus to its axion partner, which receives only Planck-suppressed contributions, the $\Phi\, H_u H_d$ coupling is modified

by MSSM loops. These radiative corrections induce large logarithms that are formally of $\mathcal{O}(1)$ and hence have to be resummed to all orders. In this chapter we have calculated the anomalous dimension γ_Z of the composite operator $H_u H_d \Box\Phi$ needed to perform such a resummation. We found that the size of the leading-logarithmic corrections to the coupling strength Z depends sensitively on the ratio of the Higgs vacuum expectation values, $\tan\beta$, through the top Yukawa coupling. As a result, loop corrections suppress $\Gamma(\Phi \to H_u H_d)$ for $\tan\beta \lesssim 3$ and $\tan\beta \gtrsim 35$, while the partial decay rate to Higgs pairs is enhanced for all other $\tan\beta$ values. The maximal enhancements occur for $\tan\beta \simeq 10$, but amount to below 10% only.

This simple pattern of suppressions and enhancements is also reproduced by our high-statistics MSUGRA scan, which includes all relevant two-loop effects. Specifically, we find that in the Minimal LARGE Volume Scenario the values of ΔN_{eff} that are compatible with a Higgs-boson mass close to 126 GeV all lie in the range $[1.4, 2.6]$. The spread of the predictions is rather insensitive to the exact values of the MSUGRA parameters m_0, $m_{1/2}$ and $\operatorname{sign}\mu$ and is influenced by the Higgs mass requirement only indirectly because this constraint needs tuning of A_0 and $\tan\beta$. In consequence, it turns out that for moderate values of $\tan\beta$, radiative corrections tend to suppress the tree-level prediction $\Delta N_{\text{eff}} \simeq 1.6$. However, the loop-induced effects are always small, leading to a robust lower bound of $\Delta N_{\text{eff}} \gtrsim 1.4$. This limit corresponds to a 3σ to 4σ tension between theory and experiment, which essentially excludes the Minimal LARGE Volume Scenario — MSSM matter content and $Z = 1$ — as a model of dark radiation.

Chapter 3

Fibred Compactifications: Dark Radiation and Soft Supersymmetry Breaking

3.1 Introduction

The first half of this chapter is based on the paper [4]. The second half is mostly based on [1], which was written in collaboration with Joseph P. Conlon.

In the previous chapter we saw that the Minimal LARGE Volume Scenario (MLVS), with purely MSSM matter content and a shift-symmetric Higgs sector, produces an overabundance of dark radiation in the form of axions. Hence the minimal model suffers from a "moduli-induced axion problem" [48]. Given this state of affairs, it is worthwhile to investigate whether or not extensions of the minimal model can can yield a value of $\Delta N_{\rm eff}$ that is compatible with observations. Furthermore, with the LHC searching for new physics beyond the Standard Model it is also more important than ever to explore the possible TeV-scale particle spectra arising from fundamental theories such as String Theory. The current lack of detection of superpartners to Standard Model particles implores us to examine new avenues — if we wish to solve the electroweak hierarchy problem with low-scale supersymmetry, we must look to extended models in order to realise this idea consistently.

A simple extension of the LARGE Volume Scenario is the scenario in which the bulk volume is controlled by two Kähler moduli instead of one [49–53]. One

linear combination of these two moduli is the volume modulus, while a transverse flat direction remains unstabilised in the tree-level potential. Compactifications of this kind have a fibration structure: their volume can be expressed in terms of 4-cycles (divisors) as

$$\mathcal{V} = \alpha\sqrt{\tau_1}\tau_2 - \sum_{i=3}^{h^{1,1}_+} \beta_i \tau_i^{3/2} \,. \tag{3.1}$$

The τ_i are the real parts of the Kähler moduli T_i and determine the sizes of 4-cycles in the extra-dimensional geometry. The first term corresponds to the bulk compactification volume, while the second term includes small blow-up cycles, one of which is required in the LVS in order to stabilise the bulk volume at exponentially large values. Examples of explicit geometries of this nature can be found in [54–56].

After an appropriate orientifold projection, the bulk geometric moduli that need to be stabilised are the axio-dilaton, the above Kähler moduli and a number of complex structure moduli (or S-, T- and U-moduli, respectively). The S- and U-moduli are stabilised by background fluxes, while the T-moduli require a combination of α'-corrections and non-perturbative effects. An interesting feature of these compactifications is that the volume modulus is no longer the lightest modulus: the post-inflationary decays to visible and hidden radiation are instead controlled by the modulus parametrising the transverse direction. Hence this extension has non-trivial consequences for post-inflationary physics, and one might imagine that the constraints on dark radiation derived in the previous chapter could thus be avoided. The purpose of the first half of this chapter is to analyse such a scenario and determine how the branching fraction to dark radiation is modified.

Furthermore, with the right ingredients such a setup may lead to anisotropic modulus stabilisation [50–53]. In the second half of this chapter we shift our focus to the anisotropic limit of fibred compactifications, and we study the implications within the more conventional framework of supersymmetric solutions

to the hierarchy problem. Our particular aim here is to compute soft terms for such a scenario: one motivation for believing this is a worthwhile task is that the anisotropy provides extra geometric structure, which may in turn generate a non-standard pattern of soft terms. Such a non-standard pattern appears to be necessary due to the complete absence of any evidence for supersymmetry in current LHC runs.

The structure of this chapter is as follows. In section 3.2 I describe and justify a fibred compactification scheme, for which I compute the decay modes, and deduce the consequences for ΔN_{eff}, in section 3.3. In section 3.4 I review relevant aspects of the anisotropic Calabi-Yau constructions of [50] and compute the F-terms for the T-moduli in such constructions. Subsequently, in section 3.5 I review the generic structure of supersymmetry-breaking soft terms. Sections 3.6 and 3.7 are dedicated to calculating the soft terms for two different scenarios, corresponding to the two possible geometric cycles on which the Standard Model branes could be located. Finally, in section 3.8 I discuss the results and consider the scope for further research.

3.2 Fibred compactifications

Here we give an overview of some key features of fibred LVS models. First of all, the compactification volume $\mathcal{V}$ takes the form[1]

$$\mathcal{V} = \alpha\sqrt{\tau_1}\tau_2 - \sum_{i=3}^{h^+_{1,1}} \beta_i \tau_i^{3/2}\,, \tag{3.2}$$

where τ_1 and τ_2 are Kähler moduli that determine the bulk extra-dimensional volume, and the remaining τ_i describe blow-up cycles ("holes") in the geometry. Such a model will also have $h^+_{1,1}$ axions a_i, so we can define complexified Kähler moduli, $T_i \equiv \tau_i + ia_i$. In the following section we will neglect all moduli except T_1 and T_2, since it turns out that we are focussing on energy scales at which

[1]Examples of such compactifications are K3 or T^4 fibrations over a $\mathbb{P}^1$ base.

all the other moduli (including complex structure moduli and the axio-dilaton) can be integrated out.

We now wish to stabilise these moduli. In particular, by considering the case of a Euclidean D3 (ED3) brane wrapping one of the blow-up moduli (say τ_3) and stacks of D7s wrapping τ_1 and τ_2,[2] one obtains a non-perturbative superpotential of the form

$$W = W_0 + Ae^{-\alpha_3 T_3} \, . \tag{3.3}$$

Here W_0 is the tree-level superpotential, which is independent of the Kähler moduli, and the second term is a non-perturbative correction due to instanton effects. This scenario leads to stabilisation of $\mathcal{V} \sim \sqrt{\tau_1}\tau_2$ at an exponentially large value, while the flat transverse direction is lifted by string loop corrections, which arise due to the D7 stacks on the bulk cycles τ_1 and τ_2.

When constructing a realistic model we must bear in mind low-energy phenomenological constraints. In particular, we would like to ensure that soft terms in the visible sector are realised at a scale sufficiently suppressed relative to the masses of all moduli. If this were not the case, requiring TeV-scale superpartners would bring the moduli down to scales $m_\Phi \lesssim 30\,\text{TeV}$. Such low moduli masses encounter the Cosmological Moduli Problem (CMP), in which they dominate the energy density of the Universe at a scale low enough to spoil the successful BBN predictions [25–27]. This problem can be avoided if the Standard Model is realised on D3 branes at a singularity, leading to a sequestering of the scale at which soft masses appear, as illustrated below.

In the following discussion we focus on LVS models in which:

- the volume takes the form (3.2);
- the low-energy spectrum of moduli contains τ_1, τ_2, and their axions;

[2]This is the "small hierarchy" scenario of [50]. We will not consider the large-hierarchy case at present, since stabilising τ_1 and simultaneously avoiding the CMP requires some additional tuning ($\tau_1 \sim p$ [1] while $m_\Omega \sim M_\text{P}/\mathcal{V}^{(3+p)/2}$ [50]). However, in the second half of this chapter we will return to this scenario, for which we will consider the consequences for dark radiation in section 3.8.

- the modulus corresponding to the transverse direction is stabilised at a scale parametrically lighter than the volume modulus;
- the Standard Model is located on D3 branes at a singularity.

This includes most fibred models — exceptions include scenarios in which the Standard Model is realised via D7 branes on the fibre cycle, or in which the fibre modulus τ_1 is stabilised by D-term constraints (for example, as in the scenarios considered in [57]).

3.2.1 Mass hierarchy

In this particular fibred realisation of LVS, a distinctive hierarchy of mass scales is generated [9,50,58]. After diagonalising in terms of mass eigenstates, we find that

$$\begin{aligned} m_{\tau_i} \sim m_{a_i} &\sim \frac{M_{\rm P} \ln \mathcal{V}}{\mathcal{V}} \qquad (i \neq 1,2) \ , \\ m_{3/2} \sim m_S \sim m_U &\sim \frac{M_{\rm P}}{\mathcal{V}} \ , \\ m_{\mathcal{V}} &\sim \frac{M_{\rm P}}{\mathcal{V}^{3/2}} \ , \\ m_{\Omega} &\sim \frac{M_{\rm P}}{\mathcal{V}^{3/2}\tau_1^{1/4}} \ , \\ m_{a_1} \sim m_{a_2} &\simeq 0 \ . \end{aligned} \tag{3.4}$$

Here Ω is the direction transverse to the volume; in the limit $\tau_1 \to \tau_2$ the mass of the transverse modulus $m_\Omega \to M_{\rm P}/\mathcal{V}^{5/3}$. For scenarios in which the Standard Model is located on branes at a singularity, soft masses are expected to appear at a scale $M_{\rm soft} \sim M_{\rm P}/\mathcal{V}^2$ [28]; for TeV-scale superpartners this implies a volume $\mathcal{V} \sim 5 \times 10^7\,\text{GeV}$, so $m_{\mathcal{V}} \sim 3 \times 10^6\,\text{GeV}$ and $m_\Omega \sim 10^5\,\text{GeV}$ (for $\tau_1 \sim \tau_2$).[3]

[3] If there is no sequestering, the soft masses instead arise at a scale $m_{3/2} \sim M_{\rm P}/\mathcal{V}$, which for TeV-scale supersymmetry is incompatible with reheating via the decay of the lightest modulus (which also suffers from the CMP). Hence such a scenario requires high-scale supersymmetry.

Let us briefly comment on the values that the VEV of τ_1 can take. On one hand we require $\tau_1 \gg 1$ — if this were not the case, (3.4) indicates that the volume and transverse moduli would have comparable masses, so we would not be able to neglect the volume modulus interactions. Furthermore, if $\tau_1 \lesssim \mathcal{O}(1)$ in string units the perturbative α' expansion is no longer trustable. On the other hand, we cannot take τ_1 too large as this will reduce $m_\Omega \lesssim 30\,\text{TeV}$, so we encounter the CMP again — for TeV-scale SUSY this corresponds to $\tau_1 \gtrsim 10^9$. We avoid all of the above problems by taking "natural" values, $\tau_1 \sim \tau_2 \sim 10^4$–$10^6$.

3.3 Leading decay modes

We now compute decay rates for the leading decay modes of the lightest modulus Ω. In this analysis we focus on the branching fractions to dark radiation and to visible matter, neglecting other possible hidden-sector channels (some of which, such as additional closed-string axions, could also contribute to dark radiation).

3.3.1 Dark radiation

The decay to axions can be computed from the Kähler potential for the bulk Kähler moduli, which can be expressed as

$$K = -\ln(T_1 + \bar{T}_1) - 2\ln(T_2 + \bar{T}_2)\,. \tag{3.5}$$

This is simply the expansion of the usual 4-dimensional $\mathcal{N} = 1$ supergravity Kähler potential for the Kähler moduli, $K = -2\ln\mathcal{V}$, in the fibred scenario (up to an irrelevant constant term). From this, we generate un-normalised kinetic terms of the form

$$\mathcal{L} \supset \frac{1}{4\tau_1^2}\left(\partial_\mu\tau_1\partial^\mu\tau_1 + \partial_\mu a_1\partial^\mu a_1\right) + \frac{1}{2\tau_2^2}\left(\partial_\mu\tau_2\partial^\mu\tau_2 + \partial_\mu a_2\partial^\mu a_2\right)\,. \tag{3.6}$$

We can canonically normalise the moduli with the reparametrisation

$$\Phi_1 = \frac{1}{\sqrt{2}}\ln\tau_1\,, \quad \Phi_2 = \ln\tau_2\,, \tag{3.7}$$

which once expanded out gives

$$\mathcal{L} \supset \frac{1}{2}\partial_\mu \Phi_1 \partial^\mu \Phi_1 + \frac{1}{2}\partial_\mu a_1 \partial^\mu a_1 + \frac{1}{2}\partial_\mu \Phi_2 \partial^\mu \Phi_2 + \frac{1}{2}\partial_\mu a_2 \partial^\mu a_2 - \sqrt{2}\Phi_1 \partial_\mu a_1 \partial^\mu a_1 - \Phi_2 \partial_\mu a_2 \partial^\mu a_2 \ . \tag{3.8}$$

The second line of this expression contains the relevant interactions for decays of the Φ moduli to axions, which according to (3.4) are massless and therefore constitute dark radiation.

To extract the relevant physics, we must rotate Φ_1 and Φ_2 into their mass eigenbasis [59],

$$\Phi_{\mathcal{V}} \equiv \sqrt{\frac{2}{3}}\Phi_2 + \sqrt{\frac{1}{3}}\Phi_1 \ , \quad \Phi_\Omega \equiv \sqrt{\frac{1}{3}}\Phi_2 - \sqrt{\frac{2}{3}}\Phi_1 \ , \tag{3.9}$$

where $\Phi_{\mathcal{V}}$ is the volume modulus and Φ_Ω is the transverse flat direction. Since Φ_Ω is the lightest modulus its decays will dominate, and hence the relevant interaction Lagrangian for decays into dark radiation is

$$\mathcal{L}_{\Omega \to aa} = \frac{1}{\sqrt{3}M_{\rm P}} \Phi_\Omega \left(2\partial_\mu a_1 \partial^\mu a_1 - \partial_\mu a_2 \partial^\mu a_2\right) \ . \tag{3.10}$$

This yields a total decay rate to axions of

$$\Gamma_{\Omega \to aa} = \frac{5}{96\pi}\frac{m_\Omega^3}{M_{\rm P}^2} \ , \tag{3.11}$$

which is a factor 5/2 larger than in the Minimal LARGE Volume Scenario.

3.3.2 Visible sector

In the Minimal LVS we saw that the leading decay mode is to Higgs bosons via the Giudice-Masiero term [32],

$$\mathcal{L} \supset \frac{1}{\sqrt{6}M_{\rm P}} \Big[Z H_u H_d \Box\Phi + \text{h.c.} \Big] \ . \tag{3.12}$$

Let us see how this is modified in the fibred case. We can compute the relevant Lagrangian from a Kähler potential of the form

$$K = -\ln(T_1 + \bar{T}_1) - 2\ln(T_2 + \bar{T}_2) + \left\{ \frac{H_{\rm u}\bar{H}_{\rm u} + H_d \bar{H}_d + (Z H_u H_d + \text{h.c.})}{\left(T_1 + \bar{T}_1\right)^{1/3}\left(T_2 + \bar{T}_2\right)^{2/3}} \right\} \ . \tag{3.13}$$

This expression contains all the relevant physics: in particular, it incorporates the appropriate scaling of the Kähler matter metric with $\mathcal{V}^{-2/3}$ [1].

Extracting the leading terms, one finds the interaction Lagrangian

$$\begin{aligned}\mathcal{L} \supset & -\frac{1}{\sqrt{6}M_{\rm P}}\left(\sqrt{\frac{1}{3}}\Phi_1+\sqrt{\frac{2}{3}}\Phi_2\right)\left[H_u\Box\bar{H}_u+\bar{H}_u\Box H_u+H_d\Box\bar{H}_d+\bar{H}_d\Box H_d\right] \\ & -\frac{1}{\sqrt{6}M_{\rm P}}\left(Z\,H_uH_d+\text{h.c.}\right)\left(\sqrt{\frac{1}{3}}\Box\Phi_1+\sqrt{\frac{2}{3}}\Box\Phi_2\right)\,. \end{aligned} \tag{3.14}$$

The second line contains the dominant interactions, as the $\Box\Phi$ terms induce a scaling with m_Φ^2, which from (3.4) is a factor $\mathcal{V}^{1/2}\sim 10^3$ larger than m_H^2. The dominant terms have the same structure as (3.12); however, note that the moduli always appear in the combination $\sqrt{1/3}\,\Phi_1+\sqrt{2/3}\,\Phi_2\equiv\Phi_\mathcal{V}$. In particular, the Lagrangian is independent of the lightest modulus Φ_Ω, so this decay mode is suppressed at tree-level.[4]

Let us consider other possible decay modes of Φ_Ω. Chiral matter scalars also interact only with $\Phi_\mathcal{V}$ at tree-level (the relevant Lagrangian has the same form as the first line of (3.14)), while interactions with fermions are chirality-suppressed because they will always contain the Dirac operator $\bar{\chi}\bar{\sigma}^\mu\partial_\mu\chi$, which vanishes on-shell. Furthermore, since the Standard Model is localised on a blow-up cycle, interactions of gauge bosons with the bulk moduli $\Phi_\mathcal{V}$ and Φ_Ω will be volume-suppressed, so decay via gauge bosons also takes place only at loop level. Finally, if there are additional vector-like matter states, we expect their tree-level couplings to moduli to be of the same form as (3.14) and hence also independent of Φ_Ω. We conclude that all visible-sector decay modes must arise only at loop level, so decays to dark radiation (and possibly other hidden-sector particles) are the dominant processes.

[4]The volume $\mathcal{V}$ does have a subleading dependence on Φ_Ω, which has been computed in [60]. However, the resulting term is suppressed by $\mathcal{V}^{-1/3}\sim 3\times 10^{-3}$, so its contribution can be neglected.

3.3.3 Prediction for the excess effective number of neutrino species

We now provide an estimate of $\Delta N_{\rm eff}$ based on these conclusions. Assuming the relevant loop-level decay rates have the form

$$\Gamma_{1-\rm loop} \sim \frac{1}{16\pi}\left(\frac{\alpha_{\rm SM}}{4\pi}\right)^2 \frac{m_\Omega^3}{M_{\rm P}^2}\,, \tag{3.15}$$

where $\alpha_{\rm SM}$ represents visible-sector couplings, the ratio of hidden to visible branching ratios is

$$\kappa \equiv \frac{\rm Br(hidden)}{\rm Br(visible)} \sim \frac{5}{6}\left(\frac{4\pi}{\alpha_{\rm SM}}\right)^2 \sim 10^4\,. \tag{3.16}$$

Since (2.30) requires $\Delta N_{\rm eff} \gtrsim 3\kappa$ [21, 22] this implies $\Delta N_{\rm eff} \gtrsim 3\times 10^4$, which completely rules out the fibred sequestered LARGE Volume Scenario with D3 branes at a singularity as a realistic model of dark radiation. We must therefore turn to other scenarios in order to avoid overproduction of axion-like particles.

3.4 Anisotropic modulus stabilisation

For the remainder of this chapter we turn our attention to the anisotropic limit of fibred compactifications. The anisotropic scenario is particularly interesting for a couple of reasons. First, if the electroweak hierarchy problem is to be solved by TeV-scale supersymmetry, the lack of superpartners observed at the LHC seems to require a non-standard pattern of soft terms. It may be possible to obtain such a non-standard soft-term structure by harnessing the anisotropy in the right way. Furthermore, with an appropriate setup it may *also* be possible to enhance the visible-sector branching ratio after inflation, ameliorating the overabundance of axions produced in the previous, isotropic model. The possibility of addressing both issues simultaneously renders this a compelling scenario worthy of further investigation.

First we summarise how fibred constructions can lead to anisotropic modulus stabilisation. We consider one of the simplest fibred scenarios: a K3

fibration over a $\mathbb{P}^1$ base, with a single del Pezzo (blow-up) divisor localised in the bulk volume. The fibred structure allows for anisotropic stabilisation such that the K3 and blow-up mode are small while the $\mathbb{P}^1$ base is hierarchically larger. While "realistic" compactifications are expected to have hundreds of moduli, the advantage of the simple model is that it is calculationally tractable.

The simple scenario has a compactified volume of the form

$$\mathcal{V} = \alpha\Big(\sqrt{\tau}_1\tau_2 - \gamma\tau_3^{3/2}\Big) \,. \tag{3.17}$$

We are interested in anisotropic stabilisation of τ_1 and τ_2, with $\tau_1 \ll \tau_2$. In order to obtain this we will follow the model proposed in [50]. This model requires poly-instanton contributions [61] to the superpotential from a Euclidean D3 brane wrapping τ_1 and a stack of D7 branes wrapping τ_3. In the presence of a racetrack superpotential, this setup allows the moduli to be stabilised such that τ_1 and τ_3 are small while τ_2 is exponentially larger [50], generating the required anisotropy.

Poly-instantons are one approach to realising anisotropic geometries — another approach involving quantum corrections to the Kähler potential is discussed in [55]. There are subtle mathematical questions about the conditions under which such poly-instantons can exist, considered in [56]. We note that the models we study here are more string-inspired than string-derived, and our aim is not so much to claim any kind of fully honest top-down construction of anisotropic vacua. To this end we focus on studying the phenomenological consequences, under the assumption that all the key features of such models can be realised in a consistent manner.

Since the overall volume is exponentially large in the LARGE Volume Scenario, in order to match the Standard Model gauge couplings it is necessary that the Standard Model arises from branes wrapping a cycle that is either small or collapsed. We shall consider the cases where the Standard Model gauge groups arise from D7-brane stacks wrapping one of the small cycles in the extra-dimensional geometry.

There are two small 4-cycles that could possibly hold D7s: the small blow-up cycle and the small volume cycle (the K3): we consider each of these cases in turn. The key determinant of soft terms is the F-terms of the Kähler moduli,

$$F^i = \frac{W}{|W|} e^{K/2} K^{i\bar{j}} \left(\overline{W}_{\bar{j}} + \overline{W} K_{\bar{j}} \right) , \tag{3.18}$$

as the Kähler moduli are dominantly responsible for SUSY breaking. We also need the Kähler matter metric $\tilde{K}_{\bar{\alpha}\beta}$ and its functional dependence on the Kähler moduli. While this cannot be computed directly, we shall argue for its functional form by generalising arguments made in [62]. Matter can arise from modes either interior or transverse to the D7 brane, and the form of the Kähler metric differs in each case.

3.4.1 A simple fibred model

We start with a Calabi-Yau volume of the form

$$\mathcal{V} = \lambda_1 t_1 t_2^2 + \lambda_2 t_3^3 , \tag{3.19}$$

where the t_i are the volumes of internal 2-cycles in the geometry, while λ_1 and λ_2 depend on the particular properties of the Calabi-Yau under consideration. In particular, t_1 is the 2-cycle corresponding to the $\mathbb{P}^1$ base.

The volume can also be expressed in terms of the dual 4-cycles $\tau_i = \partial\mathcal{V}/\partial t_i$,

$$\tau_1 = \lambda_1 t_2^2 , \quad \tau_2 = 2\lambda_1 t_1 t_2 , \quad \tau_3 = 3\lambda_2 t_3^2 , \tag{3.20}$$

giving an expression of the form

$$\mathcal{V} = \alpha\left(\sqrt{\tau}_1 \tau_2 - \gamma \tau_3^{3/2} \right) = t_1 \tau_1 - \alpha\gamma \tau_3^{3/2} , \tag{3.21}$$

where $\alpha = 1/(2\sqrt{\lambda}_1)$ and $\gamma = \frac{2}{3}\sqrt{\lambda_1/(3\lambda_2)}$. (In most of what follows we set $\alpha = \gamma = 1$ for simplicity, unless explicitly stated otherwise.)

In the LARGE-volume regime we have $t_1\tau_1 \gg \alpha\gamma\tau_3^{3/2}$, so $\mathcal{V} \simeq t_1\tau_1$. Since $t_1 = (LM_{\rm string})^2$ is the size of the $\mathbb{P}^1$ base (where $M_{\rm string}$ is the string scale), $\tau_1 = (lM_{\rm string})^4$ is the volume of the K3 fibre. We are interested in anisotropic

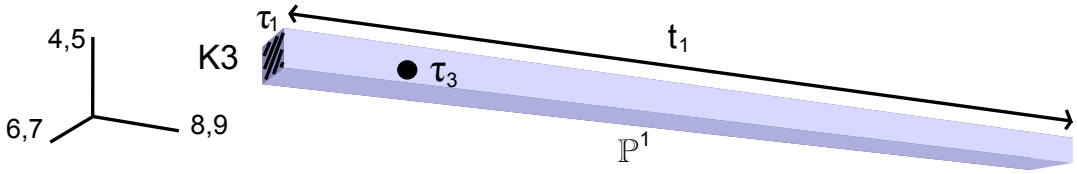

Figure 3.1: Schematic diagram of anisotropic Calabi-Yau structure.

compactifications where two of the extra dimensions are hierarchically larger than the other four, which we can achieve if $L \gg l$, or

$$\langle t_1 \rangle \gg \sqrt{\langle \tau_1 \rangle} \simeq \sqrt{\langle \tau_3 \rangle} \, . \tag{3.22}$$

This corresponds to the $\mathbb{P}^1$ base being much larger than the K3 fibre, as illustrated in figure 3.1.

3.4.2 Low-energy limit

The stabilisation is described via a four-dimensional $\mathcal{N} = 1$ supergravity theory. The Kähler moduli present are

$$T_i = \tau_i + i a_i \, , \quad i = 1, \ldots, h_{1,1} = 3 \, . \tag{3.23}$$

Here the τ_i are the volumes of the dual 4-cycles discussed above, while the $a_i = \int_{D_4^+} C_4$ are their associated axions. These appear as scalar fields in the effective 4D theory. The LVS Kähler potential is

$$K = -2 \ln \left(\mathcal{V} + \frac{\xi}{2 g_{\rm s}^{3/2}} \right) , \tag{3.24}$$

where $g_{\rm s}$ is the string coupling, and ξ depends on the particular Calabi-Yau in question but is generally $\sim \mathcal{O}(10^{-2})$.

In order to obtain a compactification that is naturally anisotropic, we follow [50] and consider a racetrack superpotential,

$$W = W_0 + A e^{-\alpha_3 T_3} - B e^{-\beta_3 T_3} \, . \tag{3.25}$$

Such a superpotential can arise from gaugino condensation on D7 branes wrapping the blow-up mode τ_3, with the requirement that the gauge group on τ_3

must be chosen to allow condensation into two separate gauge groups. However, as emphasised earlier, we use this as a phenomenological model and do not claim any kind of top-down derivation. Poly-instanton corrections may then arise when a Euclidean D3 brane wraps the τ_1 cycle. These give a non-perturbative modification of the T_3 gauge kinetic function,

$$T_3 \to T_3 + Ce^{-2\pi T_1} \ , \tag{3.26}$$

which in this scenario ends up being responsible for the anisotropic stabilisation. The full superpotential then takes the form

$$W = W_0 + Ae^{-\alpha_3(T_3 + C_1 e^{-2\pi T_1})} - Be^{-\beta_3(T_3 + C_2 e^{-2\pi T_1})} \ . \tag{3.27}$$

To stay in the semiclassical regime we require that $2\pi\langle\tau_1\rangle \gtrsim 1$, so at leading order

$$W = W_0 + Ae^{-\alpha_3 T_3}\big(1 - \alpha_3 C_1 e^{-2\pi T_1}\big) - Be^{-\beta_3 T_3}\big(1 - \beta_3 C_2 e^{-2\pi T_1}\big) \ . \tag{3.28}$$

The VEVs of the moduli $\tau_i = \mathrm{Re}(T_i)$ and axions $a_i = \mathrm{Im}(T_i)$ minimise the supergravity scalar potential

$$V_0 = e^K \Big[K^{i\bar{j}} \big(W_i + W K_i\big)\big(\overline{W}_{\bar{j}} + \overline{W} K_{\bar{j}}\big) - 3|W|^2 \Big] \ . \tag{3.29}$$

The minimisation procedure is carried out in two steps. In the LARGE-volume limit we can expand

$$V_0 = V_{\mathcal{O}(\mathcal{V}^{-3})} + V_{\mathcal{O}(\mathcal{V}^{-3-p})} \ , \tag{3.30}$$

where $V_{\mathcal{O}(\mathcal{V}^{-3})}$ is the leading-order piece that depends on the overall volume[5] and $V_{\mathcal{O}(\mathcal{V}^{-3-p})}$ contains the leading τ_1 and a_1 dependence. We proceed as follows:

1. Minimise $V_{\mathcal{O}(\mathcal{V}^{-3})}$ with respect to τ_3 in order to find a useful constraint, which ultimately fixes the VEV of τ_3;

2. Substitute the constraint into $V_{\mathcal{O}(\mathcal{V}^{-3-p})}$ and minimise the result with respect to τ_1 and a_1.

[5] In [50] it is shown (analogous to (1.31)) that under reasonable conditions $a_3 = 0$ is a minimum of $V_{\mathcal{O}(\mathcal{V}^{-3})}$. Hence we set $a_3 = 0$ in all subsequent calculations.

We focus on the key features of this calculation that are relevant to our purposes. Writing $\alpha_3 = \beta_3 + m$, one finds that $V_{\mathcal{O}(\mathcal{V}^{-3})}$ is minimised when

$$e^{-\beta_3\tau_3} = \frac{3W_0\sqrt{(\tau_3)}}{4Z\mathcal{V}} f_{\rm corr} \ , \tag{3.31}$$

where $Z \equiv B\beta_3 - A\alpha_3 e^{-m\tau_3}$ and, to leading order in τ_3^{-1},

$$f_{\rm corr} \equiv 1 - \frac{3}{4\tau_3}\left[\frac{Z}{B\beta_3^2 - A\alpha_3^2 e^{-m\tau_3}}\right] \equiv 1 - \delta_{\rm corr} \ . \tag{3.32}$$

We have assumed that $\beta_3\tau_3$ is large enough that $\delta_{\rm corr}$ will be sufficiently small for this approximation to be valid.

Substituting (3.31) into $V_{\mathcal{O}(\mathcal{V}^{-3-p})}$ we eventually find that [50]

$$V_{\mathcal{O}(\mathcal{V}^{-3-p})} = \frac{\beta}{\mathcal{V}^3}\big(2\pi\tau_1 - p\beta_3\tau_3\big)e^{-2\pi\tau_1}\cos\big(2\pi a_1\big) \ , \tag{3.33}$$

where

$$\beta \equiv 3W_0^2\sqrt{\tau_3} f_{\rm corr}\frac{\big(C_2 B\beta_3 - C_1 A\alpha_3 e^{-m\tau_3}\big)}{Z} \tag{3.34}$$

and

$$p \equiv -\left[\frac{C_2 B\beta_3^2 - C_1 A\alpha_3^2 e^{-m\tau_3}}{C_2 B\beta_3 - C_1 A\alpha_3 e^{-m\tau_3}}\right]\frac{\delta_{\rm corr}}{\beta_3} \ . \tag{3.35}$$

This potential has a global minimum at $\langle a_1\rangle = 1/2$ and $2\pi\langle\tau_1\rangle = p\beta_3\langle\tau_3\rangle + 1$. (For a more detailed derivation, see [50].)

A caveat

From the above calculation it appears that $\langle\tau_1\rangle \propto \langle\tau_3\rangle$, implying that τ_1 is naturally in the correct regime provided τ_3 is small (but sufficiently greater than one that $\delta_{\rm corr}$ is small). Let us see now why this is in fact not the case. The proportionality cancels because $p \propto \delta_{\rm corr} \propto \langle\tau_3\rangle^{-1}$ so

$$p\beta_3\langle\tau_3\rangle = -\frac{3}{4}\left[\frac{C_2 B\beta_3^2 - C_1 A\alpha_3^2 e^{-m\langle\tau_3\rangle}}{C_2 B\beta_3 - C_1 A\alpha_3 e^{-m\langle\tau_3\rangle}}\right]\frac{Z}{B\beta_3^2 - A\alpha_3^2 e^{-m\langle\tau_3\rangle}} \ . \tag{3.36}$$

This can be rearranged to give

$$p\beta_3\langle\tau_3\rangle = -\frac{3}{4}\left[1 + \frac{(C_2 - C_1)mAB\alpha_3\beta_3 e^{-m\langle\tau_3\rangle}}{(C_2 B\beta_3 - C_1 A\alpha_3 e^{-m\langle\tau_3\rangle})(B\beta_3^2 - A\alpha_3^2 e^{-m\langle\tau_3\rangle})}\right] \ . \tag{3.37}$$

Therefore the VEV of τ_1, corresponding to the volume of the K3 fibration, is given by

$$\begin{aligned}\langle\tau_1\rangle &= \frac{1}{2\pi}\left[p\beta_3\langle\tau_3\rangle + 1\right] \\ &= \frac{1}{8\pi}\left[1 - \frac{3(C_2 - C_1)mAB\alpha_3\beta_3 e^{-m\langle\tau_3\rangle}}{(C_2B\beta_3 - C_1A\alpha_3 e^{-m\langle\tau_3\rangle})(B\beta_3^2 - A\alpha_3^2 e^{-m\langle\tau_3\rangle})}\right] . \end{aligned} \tag{3.38}$$

This implies that for natural values $\langle\tau_1\rangle \sim 1/8\pi$, which is beyond the region where the α' expansion can be trusted.

Ideally we would like $\langle\tau_1\rangle$ to be larger; however this requires some fine-tuning. First of all we require the second term of (3.38) to be negative, in order to get a positive contribution to $\langle\tau_1\rangle$. Second, we would like this contribution to be large: the only way to do this is for the denominator to blow up, which is possible if either $C_2B\beta_3 \simeq C_1A\alpha_3 e^{-m\langle\tau_3\rangle}$ or alternatively $B\beta_3^2 \simeq A\alpha_3^2 e^{-m\langle\tau_3\rangle}$. Unfortunately the latter would pose problems, since a similar factor appears in the denominator of $\delta_{\rm corr}$ — which we do not want to be too small in case we end up outside the $\delta_{\rm corr} \ll 1$ approximation — so the only option appears to be the former. One possible solution would be to have $C_2 > C_1$ and $A\alpha_3 e^{-m\langle\tau_3\rangle} > B\beta_3$ with m positive. Then for $1 \gg C_2B\beta_3 - C_1A\alpha_3 e^{-m\langle\tau_3\rangle} > 0$ the correction would become large and negative, giving a positive contribution to $\langle\tau_1\rangle$.

We shall proceed on the basis that this issue can be resolved. One such resolution is that quantum corrections may push $\langle\tau_1\rangle$ into a controlled region. Alternatively we may hope that, as our interest is in the structural effects of the anisotropy on the soft terms, such structural effects — in particular the powers of the overall volume that appear — will be relatively unaffected by a small $\langle\tau_1\rangle$.

3.4.3 F-terms

Here we compute the F-terms,

$$F^i = e^{K/2}K^{i\bar{j}}\langle\overline{W}_{\bar{j}} + \overline{W}K_{\bar{j}}\rangle , \tag{3.39}$$

where the expectation value is written to emphasise that the VEVs are plugged in after taking derivatives.

Using (3.21), (3.24) and (3.28) we find that the F-terms are given by

$$F^1 = -\frac{2\langle\tau_1\rangle\tilde{F}}{\mathcal{V}-\frac{\xi}{4g_s^{3/2}}} \ , \tag{3.40}$$

$$F^2 = -\frac{2\langle\tau_2\rangle\tilde{F}}{\mathcal{V}-\frac{\xi}{4g_s^{3/2}}} - 4\sqrt{\tau_1}\langle W_1\rangle \ , \tag{3.41}$$

$$F^3 = -\frac{2\langle\tau_3\rangle\tilde{F}}{\mathcal{V}-\frac{\xi}{4g_s^{3/2}}} + \frac{8\sqrt{\tau_3}}{3}\langle W_3\rangle \ , \tag{3.42}$$

where

$$\begin{aligned}\tilde{F} =& W_0 + Ae^{-\alpha_3\langle\tau_3\rangle}\Big[\big(1+2\alpha_3\langle\tau_3\rangle\big) + \alpha_3 C_1 e^{-c\langle\tau_1\rangle}\big(1+2\alpha_3\langle\tau_3\rangle+2c\langle\tau_1\rangle\big)\Big] \\ &- Be^{-\beta_3\langle\tau_3\rangle}\Big[\big(1+2\beta_3\langle\tau_3\rangle\big) + \beta_3 C_2 e^{-c\langle\tau_1\rangle}\big(1+2\beta_3\langle\tau_3\rangle+2c\langle\tau_1\rangle\big)\Big] \ .\end{aligned} \tag{3.43}$$

The leading-order contributions are

$$F^1 = -\frac{2\langle\tau_1\rangle W_0}{\mathcal{V}} \ , \tag{3.44}$$

$$F^2 = -\frac{2\langle\tau_2\rangle W_0}{\mathcal{V}} \ , \tag{3.45}$$

$$F^3 = -\frac{2\langle\tau_3\rangle W_0\delta_{\rm corr}}{\mathcal{V}} \ . \tag{3.46}$$

In particular, note that F^3 is proportional to $\delta_{\rm corr}$ (defined above). This arises because at leading order $\langle W_3\rangle = (B\beta_3 e^{-\beta_3\langle\tau_3\rangle} - A\alpha_3 e^{-\alpha_3\langle\tau_3\rangle}) = e^{-\beta_3\langle\tau_3\rangle}Z$, so using the condition (3.31) in (3.42) we find that

$$\begin{aligned}F^3 &\simeq -\frac{2\langle\tau_3\rangle W_0}{\mathcal{V}} + \frac{8\sqrt{\tau_3}}{3}\langle W_3\rangle \\ &= -\frac{2\langle\tau_3\rangle W_0}{\mathcal{V}}\big(1-\frac{4e^{-\beta_3\tau_3}Z\mathcal{V}}{3W_0\sqrt{\tau_3}}\big) \\ &= -\frac{2\langle\tau_3\rangle W_0}{\mathcal{V}}\big(1-f_{\rm corr}\big) \ .\end{aligned} \tag{3.47}$$

Notably, since $\delta_{\rm corr} \propto \langle\tau_3\rangle^{-1}$, this means F^3 is independent of τ_3 at leading order. In fact, from the earlier discussion regarding $\langle\tau_1\rangle$, it turns out that F^1 and F^3 are both simply proportional to $1/\mathcal{V}$, each with a constant of proportionality that depends crucially on the details of the compactification.

At leading order F^2 dominates, since we are in the large hierarchy limit where $\langle\tau_2\rangle \gg \langle\tau_1\rangle \sim \langle\tau_3\rangle\delta_{\rm corr}$. Using $\mathcal{V} \simeq \sqrt{\langle\tau_1\rangle}\langle\tau_2\rangle$ we find that

$$F^2 \simeq -\frac{2W_0}{\sqrt{\langle\tau_1\rangle}} \tag{3.48}$$

at leading order. However, this dominance is not necessarily manifest in the soft terms, to which we now turn.

3.5 Soft terms: an overview

In the following sections we will compute the soft scalar masses, trilinear, and bilinear interaction terms, as well as the soft gaugino masses, that arise from moduli-mediated supersymmetry breaking in anisotropic LARGE-volume models. The moduli responsible for SUSY-breaking are the Kähler moduli. We will assume that the Standard Model is present on flux-stabilised D7 branes wrapping one of the small cycles in the extra-dimensional geometry. Small fluctuations about the vacuum configuration may then give rise to chiral matter. In this section we review the generic structure of soft terms in the supergravity framework.

The Kahler potential and superpotential can be expanded as a function of observable matter fields C^α to give

$$\mathcal{K} = K(T_i, T_{\bar{i}}^*) + \tilde{K}_{\overline{\alpha}\beta}(T_i, T_{\bar{i}}^*)C^{*\overline{\alpha}}C^\beta + \left[\frac{1}{2}Z_{\alpha\beta}(T_i, T_{\bar{i}}^*)C^\alpha C^\beta + \text{h.c.}\right] + \dots \tag{3.49}$$

and

$$\mathcal{W} = W(T_i) + \frac{1}{2}\mu_{\alpha\beta}C^\alpha C^\beta + \frac{1}{6}Y_{\alpha\beta\gamma}C^\alpha C^\beta C^\gamma + \dots \tag{3.50}$$

respectively, where K and W are the potentials for the moduli only (see (3.24) and (3.27)). We use the convention that Greek indices $\alpha, \beta, \dots$ run over observable fields while Roman indices $i, j, \dots$ correspond to the hidden moduli. Note that $\mu_{\alpha\beta}$ and $Y_{\alpha\beta\gamma}$ are independent of the T_i. This is because the Peccei–Quinn shift symmetry,

$$a_i \to a_i + c_i \ , \tag{3.51}$$

prevents the Kähler moduli from appearing in the holomorphic function $\mathcal{W}$ (except as non-perturbative terms, e.g. (3.27)). Since the superpotential is not renormalised at any order in perturbation theory, the symmetry is unbroken perturbatively. Hence the holomorphic terms are functions of the axio-dilaton and complex structure moduli only, however in the present scenario we have integrated those out. We conclude that the only remaining places where Kähler moduli can appear are in the Kähler matter metric $\tilde{K}_{\overline{\alpha}\beta}$ and the function $Z_{\alpha\beta}$. In general these are highly non-trivial to compute. However it turns out that, in the cases we want to consider, the dependence of $\tilde{K}_{\overline{\alpha}\beta}$ on the T-moduli can be deduced through scaling arguments. Finally, in order to fix $Z_{\alpha\beta}$ we assume that its dependence on the Kähler moduli is related to that of $\tilde{K}_{\overline{\alpha}\beta}$, as would be the case if these terms were to share a common origin in the fundamental theory.[6]

For now, let us compute the general structure of soft terms. By plugging $\mathcal{K}$ and $\mathcal{W}$ into the supergravity scalar potential,[7]

$$V = e^{\mathcal{K}}\left[\mathcal{K}^{I\overline{J}}\left(\mathcal{W}_I + \mathcal{W}\mathcal{K}_I\right)\left(\overline{\mathcal{W}}_{\overline{J}} + \overline{\mathcal{W}}\mathcal{K}_{\overline{J}}\right) - 3|\mathcal{W}|^2\right], \tag{3.52}$$

and taking the limit $M_P \to \infty$ to neglect non-renormalisable (hard) terms, we find that the scalar potential becomes

$$V = V_0 + V_{\text{soft}}\ . \tag{3.53}$$

The soft scalar potential V_{soft} can be written in the form

$$V_{\text{soft}} = \left(m_0^2 + m'^2\right)_{\overline{\alpha}\beta} C^{*\overline{\alpha}} C^{\beta} + \left(\frac{1}{2} B'_{\alpha\beta} C^{\alpha} C^{\beta} + \frac{1}{6} A'_{\alpha\beta\gamma} C^{\alpha} C^{\beta} C^{\gamma} + \text{ h.c.}\right), \tag{3.54}$$

where $(m_0^2)_{\overline{\alpha}\beta}$ is a supersymmetric mass term,[8] while $m'^2_{\overline{\alpha}\beta}$, $A'_{\alpha\beta\gamma}$ and $B'_{\alpha\beta}$ are the un-normalised scalar masses, trilinear *A-terms* and bilinear *B-terms*, re-

[6]Note that $Z_{\alpha\beta}$ includes couplings associated with Giudice-Masiero interactions — the Higgs-sector coupling Z, considered in Chapter 2 and in the first part of this chapter, is one such coupling. Furthermore, the shift symmetry that was invoked to set $Z = 1$ at the string scale is a prime example of a situation in which $Z_{\alpha\beta}$ and $\tilde{K}_{\overline{\alpha}\beta}$ have a common origin.

[7]The convention here is that indices $I, J, \ldots$ run over both hidden and observable fields.

[8]To be precise, $(m_0^2)_{\overline{\alpha}\beta} = \mu'_{\alpha\beta}\tilde{K}^{\alpha\overline{\beta}}\overline{\mu'}_{\overline{\beta}\overline{\alpha}}$, where $\mu'_{\alpha\beta}$ is the effective μ parameter of (3.64).

spectively:

$$\begin{aligned} m'^2_{\overline{\alpha}\beta} &= \Big(m^2_{3/2} + V_0\Big)\tilde{K}_{\overline{\alpha}\beta} \\ &\quad - \overline{F}^{\bar{i}}\Big(\partial_{\bar{i}}\partial_j\tilde{K}_{\overline{\alpha}\beta} - \partial_{\bar{i}}\tilde{K}_{\overline{\alpha}\gamma}\tilde{K}^{\gamma\bar{\delta}}\partial_j\tilde{K}_{\bar{\delta}\beta}\Big)F^j \ ; \end{aligned} \tag{3.55}$$

$$\begin{aligned} A'_{\alpha\beta\gamma} &= \frac{\overline{W}}{|W|}e^{K/2}F^i\Big[K_iY_{\alpha\beta\gamma} + \partial_iY_{\alpha\beta\gamma} \\ &\quad - \Big(\tilde{K}^{\delta\overline{\rho}}\partial_i\tilde{K}_{\overline{\rho}\alpha}Y_{\delta\beta\gamma} + (\alpha\leftrightarrow\beta) + (\alpha\leftrightarrow\gamma)\Big)\Big] \ ; \end{aligned} \tag{3.56}$$

$$\begin{aligned} B'_{\alpha\beta} &= \frac{\overline{W}}{|W|}e^{K/2}\Big\{F^i\Big[K_i\mu_{\alpha\beta} + \partial_i\mu_{\alpha\beta} \\ &\quad - \Big(\tilde{K}^{\delta\overline{\rho}}\partial_i\tilde{K}_{\overline{\rho}\alpha}\mu_{\delta\beta} + (\alpha\leftrightarrow\beta)\Big)\Big] - m_{3/2}\mu_{\alpha\beta}\Big\} \\ &\quad + \Big(2m^2_{3/2} + V_0\Big)Z_{\alpha\beta} - m_{3/2}\overline{F}^{\bar{i}}\partial_{\bar{i}}Z_{\alpha\beta} \\ &\quad + m_{3/2}F^i\Big[\partial_iZ_{\alpha\beta} - \Big(\tilde{K}^{\delta\overline{\rho}}\partial_i\tilde{K}_{\overline{\rho}\alpha}Z_{\delta\beta} + (\alpha\leftrightarrow\beta)\Big)\Big] \\ &\quad - \overline{F}^{\bar{i}}F^j\Big[\partial_{\bar{i}}\partial_jZ_{\alpha\beta} - \Big(\tilde{K}^{\delta\overline{\rho}}\partial_j\tilde{K}_{\overline{\rho}\alpha}\partial_{\bar{i}}Z_{\delta\beta} + (\alpha\leftrightarrow\beta)\Big)\Big] \ . \end{aligned} \tag{3.57}$$

For a diagonal Kähler matter metric,

$$\tilde{K}_{\overline{\alpha}\beta} = \tilde{K}_\alpha\delta_{\overline{\alpha}\beta} \ , \tag{3.58}$$

we can simplify many of the soft-term expressions. The B-term is only relevant for the Higgs fields, for which we require that only $Z_{H_1H_2} = Z_{H_2H_1} \equiv Z$ is non-zero.[9] We expect the superpotential μ term to vanish for all soft matter, since its magnitude is set by the Planck scale and a non-zero value would lift the masses up to that scale. Nevertheless, we define $\mu_{H_1H_2} = \mu_{H_2H_1} \equiv \mu$ in order to better understand the structure of the B-term calculation, before finally taking the limit $\mu \to 0$. Hence the complete soft term Lagrangian, including gaugino mass terms, becomes [63]

$$\begin{aligned} \mathcal{L}_{\text{soft}} &= \frac{1}{2}(M_a\widehat{\lambda}^a\widehat{\lambda}^a + \text{h.c.}) - m^2_\alpha\widehat{C}^{*\overline{\alpha}}\widehat{C}^\alpha \\ &\quad - \left(\frac{1}{6}A_{\alpha\beta\gamma}\widehat{Y}_{\alpha\beta\gamma}\widehat{C}^\alpha\widehat{C}^\beta\widehat{C}^\gamma + B\widehat{\mu}\widehat{H}_1\widehat{H}_2 + \text{h.c.}\right) , \end{aligned} \tag{3.59}$$

[9] However, if we wanted to introduce additional Higgs-like states to avoid overproduction of dark radiation, this would require the presence of extra $Z_{\alpha\beta}$ couplings.

where it is now convenient to use canonically normalised soft matter fields, e.g. scalar fields,

$$\widehat{C}^{\alpha} = \tilde{K}_{\alpha}^{1/2} C^{\alpha} \ , \tag{3.60}$$

and gauginos,

$$\widehat{\lambda}^{a} = (\mathrm{Re}(f_a))^{1/2} \lambda^{a} \ . \tag{3.61}$$

Here f_a is the gauge kinetic function (the index a runs over gauge groups). We have also introduced the physical Yukawa couplings,

$$\widehat{Y}_{\alpha\beta\gamma} \ = Y_{\alpha\beta\gamma} \frac{\overline{W}}{|W|} e^{K/2} (\tilde{K}_{\alpha} \tilde{K}_{\beta} \tilde{K}_{\gamma})^{-1/2} \ , \tag{3.62}$$

and the rescaled μ parameter,

$$\widehat{\mu} \ \equiv (\tilde{K}_{H_1} \tilde{K}_{H_2})^{-1/2} \mu' \ , \tag{3.63}$$

where

$$\mu' \ \equiv \frac{\overline{W}}{|W|} e^{K/2} \mu + m_{3/2} Z - \overline{F}^{\bar{i}} \partial_{\bar{i}} Z \ . \tag{3.64}$$

With these simplifying assumptions, the soft terms are given by the expressions

$$M_a = \frac{1}{2\mathrm{Re}(f_a)} F^m \partial_m f_a \ , \tag{3.65}$$

$$m_{\alpha}^2 \ = \ \Big(m_{3/2}^2 + V_0 \Big) - \overline{F}^{\bar{i}} F^j \partial_{\bar{i}} \partial_j \ln \tilde{K}_{\alpha} \ , \tag{3.66}$$

$$A_{\alpha\beta\gamma} \ = \ F^i \Big[K_i + \partial_i \ln Y_{\alpha\beta\gamma} - \partial_i \ln (\tilde{K}_{\alpha} \tilde{K}_{\beta} \tilde{K}_{\gamma}) \Big] \ , \tag{3.67}$$

$$\begin{aligned} B \ = \ & \widehat{\mu}^{-1} (\tilde{K}_{H_1} \tilde{K}_{H_2})^{-1/2} \Bigg\{ \frac{\overline{W}}{|W|} e^{K/2} \mu \Big(F^i \Big[K_i + \partial_i \ln \mu \\ & - \partial_i \ln (\tilde{K}_{H_1} \tilde{K}_{H_2}) \Big] - m_{3/2} \Big) \\ & + \Big(2 m_{3/2}^2 + V_0 \Big) Z - m_{3/2} \overline{F}^{\bar{i}} \partial_{\bar{i}} Z \\ & + m_{3/2} F^i \Big[\partial_i Z - Z \partial_i \ln (\tilde{K}_{H_1} \tilde{K}_{H_2}) \Big] \\ & - \overline{F}^{\bar{i}} F^j \Big[\partial_{\bar{i}} \partial_j Z - \partial_{\bar{i}} Z \partial_j \ln (\tilde{K}_{H_1} \tilde{K}_{H_2}) \Big] \Bigg\} \ . \end{aligned} \tag{3.68}$$

In the large-hierarchy model there are two possible cycles on which chiral matter could be located: the blow-up mode τ_3 and the small cycle τ_1 corresponding to the K3 fibration. The large cycle τ_2 is ruled out based on the observed values of the Standard Model gauge couplings. For each scenario we will first need to deduce the Kähler matter metric $\tilde{K}_{\overline{\alpha}\beta}$, in order to be able to compute soft terms. We consider each case in turn.

3.6 D7s wrapping the blow-up mode τ_3

The first possibility is that the Standard Model is generated on magnetised D7 branes localised on the blow-up mode of size τ_3. Since non-perturbative effects are located on this cycle, there may be a tension between the chiral nature of the Standard Model and the non-perturbative effects [64], although see [65] for arguments that this can be evaded.

To determine the Kähler matter metric we use an argument articulated in [62]. First we deduce how $\tilde{K}_{\overline{\alpha}\beta}$ depends on the volume cycles τ_1 and τ_2 by assuming that the physical Yukawa couplings $\widehat{Y}_{\alpha\beta\gamma}$ are independent of the bulk volume $\mathcal{V}$, and subsequently we use scaling arguments to extract the leading-order τ_3 dependence. We then compute the soft terms and find that they are all of order $m_{3/2}$ multiplied by a universal factor $\delta_{\rm corr}$, which depends upon the details of the compactification.

3.6.1 Computing the Kähler matter metric

We can deduce the Kähler matter metric $\tilde{K}_{\overline{\alpha}\beta}$ by considering the canonical normalisation of the Yukawa couplings,[10]

$$\widehat{Y}_{\alpha\beta\gamma} = \frac{e^{K/2} Y_{\alpha\beta\gamma}}{\left(\tilde{K}_\alpha \tilde{K}_\beta \tilde{K}_\gamma\right)^{1/2}} \ . \tag{3.69}$$

[10] We have assumed a diagonal Kähler matter metric for simplicity, $\tilde{K}_{\overline{\alpha}\beta} = \tilde{K}_\alpha \delta_{\overline{\alpha}\beta}$, since the results here do not depend on the structure of $\tilde{K}_{\overline{\alpha}\beta}$.

Here the $\widehat{Y}_{\alpha\beta\gamma}$ are physical Yukawa couplings while the $Y_{\alpha\beta\gamma}$ are the corresponding superpotential Yukawa couplings (3.50). The $Y_{\alpha\beta\gamma}$ are independent of the Kähler moduli, while the τ_i dependence of K is known.

Let us now consider the T_i dependence of the physical Yukawa couplings $\widehat{Y}_{\alpha\beta\gamma}$. These are marginal couplings generated by local interactions within the bulk, so we want them to remain finite when we decouple gravity, i.e. when we take the limit $M_{\rm P} \to \infty$. In addition, since matter fields are localised on the blow-up cycle they should be unaffected by a rescaling of the bulk volume $\mathcal{V}$. Therefore, we deduce that the physical Yukawas must be independent of $\mathcal{V} \simeq \sqrt{\tau_1}\tau_2$ at leading order in the LARGE-volume expansion.

Furthermore, even though the bulk is anisotropic, by assumption all cycles are large enough to be outside the quantum regime. Since in this case the Yukawa couplings are localised at a singularity, this ensures that they should also be independent of anisotropic rescalings of the bulk cycles. This then implies that the physical Yukawas are independent of both τ_1 and τ_2.

Therefore in the present scenario we expect the leading contribution to the matter metric to be

$$\tilde{K}_\alpha = \frac{k'_\alpha}{\mathcal{V}^{2/3}} = \frac{k'_\alpha}{(\tau_1\tau_2^2)^{1/3}} \ . \tag{3.70}$$

Note that this result contains the same $\mathcal{V}$ dependence as the simpler case where a single large cycle controls the bulk volume [62].

Now we turn to the dependence of the matter metric on the small blow-up cycle τ_3. Assuming we are in the geometric regime, the leading-order T-moduli dependence of the Kähler matter metric is given by

$$\tilde{K}_{\overline{\alpha}\beta} = \frac{\tau_3^{\lambda_\alpha}}{(\tau_1\tau_2^2)^{\frac{1}{3}}} k_{\overline{\alpha}\beta} \ . \tag{3.71}$$

The function $k_{\overline{\alpha}\beta}$ depends only on S- and U-moduli, so we treat it as a constant. The value of λ depends on whether matter originates as bulk matter, with support across the whole 4-cycle, or as a 'matter curve', with support only on a 2-dimensional subspace of the local 4-cycle.

3.6.2 Soft terms

The soft terms in this case are very similar to an analogous calculation in [66]. The gauge kinetic function f_a is simply

$$f_a = k_a T_3 \ , \tag{3.72}$$

for an appropriate constant k_a. The gaugino mass (3.65) is then[11]

$$M_a = -\frac{\delta_{\rm corr} W_0}{\mathcal{V}} \quad \forall\ a \ , \tag{3.73}$$

where $\delta_{\rm corr}$ is defined in (3.32).

The soft scalar masses and trilinear A-terms are given by (3.66) and (3.67), respectively. These are:

$$m_\alpha^2 = \frac{\lambda_\alpha (\delta_{\rm corr})^2 W_0^2}{\mathcal{V}^2} \ ; \quad A = \frac{\delta_{\rm corr} W_0}{\mathcal{V}} \ . \tag{3.74}$$

The A-terms are universal due to the constraint $\lambda_\alpha + \lambda_\beta + \lambda_\gamma = 1$, which is required in order to get the correct scaling for the Yukawa couplings.

Finally, we turn to the B-term. We do not specify the geometric origin of the Higgs doublets, so for generality we express the scaling of their Kähler matter metric components as

$$\tilde{K}_{H_i} = \frac{\tau_3^{\lambda_{H_i}}}{(\tau_1 \tau_2^2)^{\frac{1}{3}}} k_{H_i} \ , \quad i = 1, 2 \ . \tag{3.75}$$

The function $Z(T_i, T_{\bar{i}}^*)$ is in general unknown and hard to compute, as it is not protected by holomorphy. However, we can proceed by making the assumption that the scaling of Z with τ_3 is related to the scalings of $\tilde{K}_{H_1}$ and $\tilde{K}_{H_2}$ with τ_3, which would be the case if all these terms had the same origin in the fundamental theory. Using the fact that $Z \equiv Z_{H_1 H_2}$ and interpreting Z, $\tilde{K}_{H_1}$ and $\tilde{K}_{H_2}$ as products and squares of vielbeins, one can see that Z should scale as $\sqrt{\tilde{K}_{H_1} \tilde{K}_{H_2}}$. Therefore

$$Z = \frac{\tau_3^{\overline{\lambda}}}{(\tau_1 \tau_2^2)^{\frac{1}{3}}} z \ , \tag{3.76}$$

[11] Note that throughout these soft-term calculations we are using units in which $M_{\rm P} = 1$.

where z is independent of the Kähler moduli and $\overline{\lambda} \equiv (\lambda_{H_1} + \lambda_{H_2})/2$.

Using this information, and setting the superpotential $\mu = 0$, one can use (3.68) to calculate the B-term. The result is

$$B = \frac{(\overline{\lambda} + 1)\delta_{\rm corr} W_0}{\mathcal{V}} \ . \tag{3.77}$$

The key feature here is that the soft terms are all of the same order and all comparable to the gravitino mass, $m_{3/2} = W_0/\mathcal{V}$. Note that they are all multiplied by a factor $\delta_{\rm corr}$, which is inversely proportional to $\langle \tau_3 \rangle$. The no-scale structure is broken by F^3, the F-term corresponding to the blow-up mode, as one would expect based on simpler LARGE-volume models.

3.7 D7s wrapping the small volume cycle $\boldsymbol{\tau_1}$

We now consider the realisation of the Standard Model on D7 branes wrapping the small volume cycle of size τ_1 (corresponding to the K3 fibre). We assume that this can be done consistently with the generation of structures appropriate for realising the anisotropic stabilisation, in concordance with our aim of exploring the possible soft-term structures that can arise from anisotropic constructions.

Under this assumption, we compute the soft terms for chiral matter on the D7s wrapping τ_1. Two types of matter are possible: modes ϕ corresponding to the position of the D7 stack in transverse space; and 'longitudinal' modes, coming from the massless modes of 8-dimensional gauge multiplet fields A inside the D7 worldvolume [67]. It turns out that the anisotropy naturally generates a large hierarchy between generations of soft terms. Again we begin by computing the T-moduli dependence of the Kähler matter metric for the two types of matter. To this end, we consider first the result for a 6-torus (projected as $T^2 \times T^2 \times T^2$). From the expression for the volume $\mathcal{V}$ we then deduce how the result is modified in the present scenario. Finally, we compute soft terms.

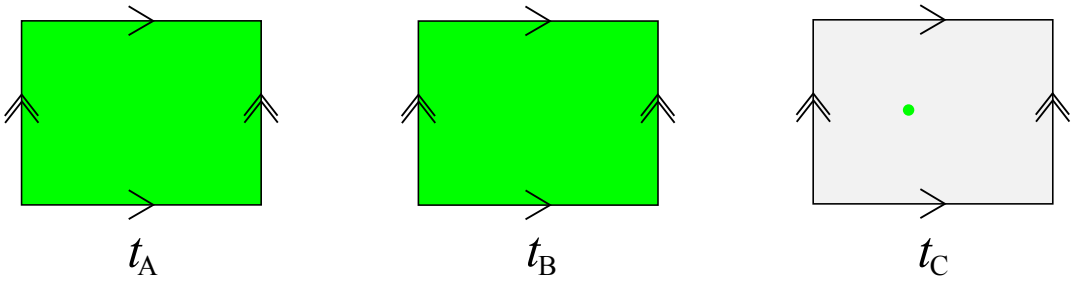

Figure 3.2: Compactification on $T^2 \times T^2 \times T^2$ with D7 branes wrapping tori A and B. The D7s are pointlike in torus C and free to move about.

3.7.1 Kähler matter metric with two components

First, a toroidal example. The bulk volume is simply given by a product of 2-cycles,

$$\mathcal{V} = t_A t_B t_C \ , \tag{3.78}$$

where the 2-cycles correspond to areas of tori, labelled A, B and C. It turns out that, for the case of D7 branes transverse to the t_C direction (see figure 3.2), the transverse and internal components of the Kähler matter metric are (see e.g. [67])

$$\tilde{K}_{\parallel} = \tilde{K}_{(7^C 7^C)_B} = \frac{1}{(2\tau_A)} \ ; \quad \tilde{K}_{\perp} = \tilde{K}_{(7^C 7^C)_C} = \frac{g_s}{2} \ , \tag{3.79}$$

where τ_A is the dual 4-cycle to t_A. The 7^C refers to a D7 brane transverse to the complex plane of torus C, while the outer subscript indicates in which plane the string modes exist. For example, the first term refers to string modes inside the D7 worldvolume, which at low energies correspond to components A of brane-worldvolume fluxes. The second term corresponds to tranverse string modes, which are related to the position of the stack of D7s on torus C. At low energies they are realised as scalars ϕ in the effective 8D theory on the brane. These components of the matter metric turn out to be independent of the T-moduli.

Now let us compare the above simple scenario to our model. Neglecting the blow-up mode, the volume is given by

$$\mathcal{V} \simeq t_1 \tau_1 \simeq t_1 t_2^2 \ , \tag{3.80}$$

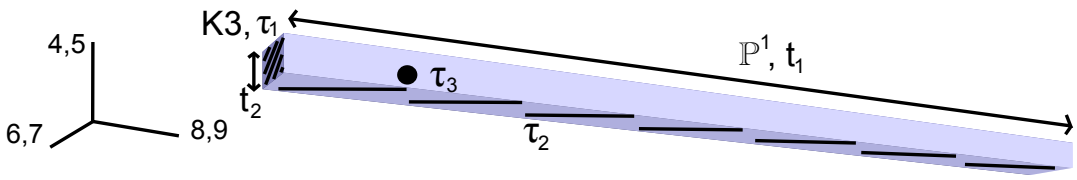

Figure 3.3: Geometrical meaning of t_1, t_2, τ_1 and τ_2.

so the obvious schematic relations between the 2-cycles and their dual 4-cycles are $\tau_1 \sim t_2^2$ and $\tau_2 \sim t_1 t_2$ (see figure 3.3). Since the D7 branes wrap τ_1 they are transverse to t_1, so this 2-cycle plays the same role as $t_{\rm C}$ above. The role of t_2 is slightly more subtle, but it essentially plays the role of $t_{\rm A} = t_{\rm B}$. Since τ_1 corresponds to the K3, t_2 is effectively the 'square root' of the K3 volume.

From this discussion, we conclude that the components of the Kähler matter metric are given by

$$\tilde{K}_{\parallel} = \frac{1}{(2\tau_2)} \; ; \quad \tilde{K}_{\perp} = \frac{g_{\rm s}}{2} \; . \tag{3.81}$$

Matter fields in a single generation — those fields with identical gauge charges — can have distinct geometric origins and thereby distinct Kähler metrics. The different volume scalings of these Kähler metrics can lead to different soft terms, as we will now discover.

3.7.2 Soft terms revisited

We can now compute soft terms for the scenario in which Standard Model D7s wrap the small volume cycle τ_1. The gaugino masses are once again given by (3.65),

$$M_a = \frac{1}{2{\rm Re}(f_a)} F^m \partial_m f_a \; , \tag{3.82}$$

but this time the gauge kinetic function, $f_a = k_a T_1$. Therefore,

$$M_a = -\frac{W_0}{\mathcal{V}} \qquad \forall \; a \; , \tag{3.83}$$

i.e. the gaugino masses have the same magnitude as the gravitino mass.

There are now two possible soft scalar masses, corresponding to transverse (ϕ) and internal D7-worldvolume (A) modes. The different matter metrics in

equation (3.81) give different soft terms,

$$m_\perp^2 = \frac{W_0^2}{\mathcal{V}^2} + \mathcal{O}(\mathcal{V}^{-3}) \ , \quad m_\parallel^2 = \mathcal{O}(\mathcal{V}^{-3}) \ . \tag{3.84}$$

We find that the transverse scalars have masses of order the gravitino mass, $m_{3/2} = W_0/\mathcal{V}$, while the internal scalars are suppressed by a factor of $1/\mathcal{V}$.

Next we turn to the A-terms. There are now four possibilities, depending on which of the three interacting scalars are transverse or internal. These turn out to be

$$\begin{aligned} A_{\perp\perp\perp} &= \frac{3W_0}{\mathcal{V}} \ , & A_{\perp\perp\parallel} &= \frac{2W_0}{\mathcal{V}} \ , \\ A_{\perp\parallel\parallel} &= \frac{W_0}{\mathcal{V}} \ , & A_{\parallel\parallel\parallel} &= \mathcal{O}(\mathcal{V}^{-2}) \ . \end{aligned} \tag{3.85}$$

Note that the A-terms are proportional (at tree-level) to the integer number of transverse ϕ matter modes involved in the interaction, so the trilinear term corresponding to the A-A-A interaction is strongly suppressed.

Finally, we compute the B-term. To this end, it is worth recalling how the B-term appears in the MSSM Lagrangian:

$$\mathcal{L}_B = -\left(B\widehat{\mu}\widehat{H_1}\widehat{H_2} \ + \ \text{h.c.} \right) \ , \tag{3.86}$$

where $\widehat{H_1}$ and $\widehat{H_2}$ are the Higgs doublets. Note in particular that the bilinear term scales as the combination $B\widehat{\mu}$, so it is possible for B to diverge at leading order while the overall bilinear term remains finite. To acknowledge this point, we carry out the calculation for arbitrary μ and take the limit $\mu \to 0$.

There are three different possible values for the B-term, depending on the geometric origin of each Higgs doublet. These correspond respectively to scenarios where: both doublets arise from transverse ϕ scalars; one doublet is a transverse ϕ mode and the other is an internal A mode; or both Higgs doublets are internal A modes. Since the Kähler matter metric depends only on τ_2 we restrict our focus to this modulus. As in section 3.6, we assume that the power dependence of Z on the relevant modulus is the geometric mean of the

dependencies of $\tilde{K}_{H_1}$ and $\tilde{K}_{H_2}$. For $\tilde{K}_{H_1} \sim \tau_2^{-\lambda_{H_1}}$, $\tilde{K}_{H_2} \sim \tau_2^{-\lambda_{H_2}}$ and $Z \sim \tau_2^{-\overline{\lambda}}$, where $\overline{\lambda} = (\lambda_{H_1} + \lambda_{H_2})/2$, we find that

$$B = \frac{2m_{3/2}\big(1-\overline{\lambda}\big)\big\{e^{K/2}\mu + \big(1-\frac{1}{2}\overline{\lambda}\big)m_{3/2}Z\big\}}{\mu'} \,, \tag{3.87}$$

where

$$\mu' \equiv \big(\tilde{K}_{H_1}\tilde{K}_{H_2}\big)^{\frac{1}{2}}\widehat{\mu} = e^{K/2}\mu + \big(1-\overline{\lambda}\big)m_{3/2}Z \,. \tag{3.88}$$

We consider each possible value of $\overline{\lambda}$ and evaluate the respective B-terms.

1. Both doublets arise from transverse ϕ scalars.

Here $\tilde{K}_{H_1}$, $\tilde{K}_{H_2}$ and Z are all independent of τ_2, so $\overline{\lambda} = 0$. We find that

$$B = 2m_{3/2} = \frac{2W_0}{\mathcal{V}} \,. \tag{3.89}$$

This result holds regardless of the value of the superpotential μ term.

2. One doublet is a transverse ϕ-mode and the other is an internal A-mode.

We now have $\tilde{K}_{H_1} \sim \tau_2^{-1}$ and $\tilde{K}_{H_2} \sim \tau_2^0$ (or vice-versa), so $Z \sim \tau_2^{-1/2}$. Therefore,

$$B = \frac{3m_{3/2}}{2} = \frac{3W_0}{2\mathcal{V}} \,. \tag{3.90}$$

3. Both Higgs doublets are internal A-modes.

Finally, we consider the scenario where $\tilde{K}_{H_1} \sim \tilde{K}_{H_2} \sim Z \sim \tau_2^{-1}$. In this case $\overline{\lambda} = 1$, which implies that B is undefined: after taking the limit $\mu \to 0$ we find that $\widehat{\mu} = 0$ at leading order. Hence the denominator of B, given by (3.88), vanishes; however the physical B-term depends on the combination $B\widehat{\mu}$. We find that for $\overline{\lambda} = 1$ the numerator of B also vanishes, so

$$B\widehat{\mu} = 0 \tag{3.91}$$

at leading order in $1/\mathcal{V}$.

For our purposes the latter two possibilities are more interesting, since they involve Higgs modes that are naturally suppressed with respect to the gravitino mass. In the final scenario the B-term itself is suppressed.

3.7.3 Low-energy consequences

At first glance, one would be tempted to conclude that there can be an inter-generational soft term splitting of order $1/\mathcal{V}$. This is interesting because various models of so-called natural supersymmetry rely on light third-generation soft terms, with heavier scalar masses for the first two generations (see e.g. [68], and for a stringy model see [69]).

However, the soft terms have been evaluated at tree-level and at the compactification scale. To obtain the soft terms observed at TeV-scale, one must integrate out the higher-energy modes via the renormalisation group flow and in doing so include loop corrections. Such radiative corrections will tend to reduce the inter-generational splitting, and since all soft terms feed into one another we expect the low-energy splitting to be no larger than a loop factor. This scenario requires $\mathcal{V} \sim \mathcal{O}(10^{14})$ for TeV-scale soft terms, so we would have a UV string scale of order $M_{\rm string} \sim 10^{11}\,\text{GeV}$. Since this is expected to be the UV scale for soft-term and gauge-coupling running, such a scenario would not be compatible with any kind of conventional grand unification.[12]

3.8 Discussion and summary

In this chapter we have considered a simple fibred extension of the Minimal LARGE Volume Scenario. Our first point of interest was to investigate the yield of dark radiation in such models — to this end, we focussed on scenarios in which the visible sector is located on D3 branes at a singularity, which sequesters the soft terms down to order $M_{\rm P}/\mathcal{V}^2$. For a compactification volume $\mathcal{V} \sim 5 \times 10^7$ the lightest modulus obtains a mass at $m_\Omega \sim 10^5\,\text{GeV}$, sufficiently heavy to avoid the Cosmological Moduli Problem. We computed the ratio of branching fractions to hidden- and visible-sector final states and found that this scenario is killed by an excess of dark radiation, with $\Delta N_{\rm eff} \gtrsim 3 \times 10^4$.

[12] However, note that this possibility has arguably been eliminated already, owing to the choice of a racetrack superpotential (3.25).

Following this, we turned instead to the anisotropic limit of fibred compactifications. We computed soft terms for this scenario, assuming now that the chiral matter of the Standard Model is located on flux-stabilised D7 branes wrapping one of the small cycles. We studied a simple model that has a compactified volume of the form

$$\mathcal{V} = \alpha\left(\sqrt{\tau}_1\tau_2 - \gamma\tau_3^{3/2}\right) \tag{3.92}$$

when expressed in terms of the real parts of Kähler moduli, which correspond to the sizes of 4-cycles in the geometry. Two of these moduli correspond to small cycles: the blow-up cycle τ_3, which is localised in the bulk, and the small volume cycle τ_1. We have considered what happens when a stack of D7s wraps each of these small cycles and computed the associated soft terms.

When the chiral matter of the Standard Model is produced by magnetised D7 branes wrapping the blow-up mode, we find soft terms that are of order $m_{3/2}$ and multiplied by a universal factor that depends upon the details of the compactification. This is a typical structure of the kind one would expect based on similar, simpler LARGE-volume models. On the other hand, when the Standard Model comes from additional D7s wrapping the small volume cycle there is a splitting between generations of soft terms, which is a new feature. This can be understood heuristically as coming directly from the anisotropy, since some modes are aligned along the large directions transverse to the D7 worldvolume, while other internal D7 modes oscillate along the small cycle directions. Some of the soft terms are of order $m_{3/2}$, while others (those corresponding to modes in the D7 worldvolume) are suppressed at tree-level by a factor of $1/\mathcal{V}$.

For the case of D7s wrapping τ_1, we compared the Calabi-Yau structure with the toroidal case and constructed the matter metric by analogy. We found two different terms, depending on the higher-dimensional origin of matter:

$$\tilde{K}_{\parallel} = \frac{1}{(2\tau_2)} \; ; \quad \tilde{K}_{\perp} = \frac{g_{\rm s}}{2} \; . \tag{3.93}$$

Note that one of these is independent of the Kähler moduli, while the other is not. The suppression of the soft terms corresponding to D7-worldvolume oscillations is a direct consequence of this fact.

Let us also mention some limitations of this result. Our interest has been in the phenomenology of anisotropy and we have simply assumed the validity of the poly-instanton approach to constructing an anisotropic compactification. It is fair to say that such approaches are at best string-inspired rather than string-derived. Furthermore, to generate the splitting in soft terms one needs to wrap an extra stack of D7 branes around the K3. It is conceivable that instanton corrections generated by these D7s could dominate over the poly-instantons and remove the anisotropy. If this turns out to be the case, then to produce a splitting between soft terms one must somehow modify the construction so that it is consistent with both anisotropy-generating poly-instantons and the wrapping of a small volume cycle by a stack of D7 branes. A fully consistent top-down construction of such anisotropic models would be welcome.

Since the fibred sequestered scenario is eliminated by an excess of dark radiation, it is pertinent to ask how the dark radiation yield would be modified in the anisotropic limit, with visible matter on D7s wrapping the fibred cycle. An important consequence of such a scenario is that the Kähler matter metric would no longer depend only on the bulk volume $\mathcal{V}$ but also on Ω, so a tree-level coupling to Higgs bosons would be restored.[13] Furthermore, since the Standard Model would now be located on the very cycle (τ_1) corresponding to the lightest modulus, a tree-level coupling to gauge bosons would be generated via the gauge kinetic function, which depends on T_1 and hence on the lightest modulus Φ_Ω. This further enhances the branching fraction to the visible sector.

The predictions for axionic dark radiation in such a scenario have been worked out in [57] and allow for $\Delta N_{\text{eff}} \simeq 0.6$ for $Z = 1$ at the string scale (in

[13]Note however that as argued above, the suppression of the Higgs bilinear is at most $\mathcal{V}^{-1}$ times a loop factor. Hence the only kinematically viable decay to the Higgs sector would be to the light 125 GeV boson observed at the LHC.

the case where the reheating temperature is sufficiently high that all Standard Model degrees of freedom are thermalised after reheating). However, it is not possible to realise TeV-scale supersymmetry in such a scenario, as to do so would push $m_{\mathcal{V}}$ down to MeV scales, leading once again to the Cosmological Moduli Problem. Therefore, this scenario makes sense only in the context of high-scale supersymmetry, with soft terms $M_{\rm soft} \gtrsim 10^8\,{\rm GeV}$ — in particular, natural supersymmetry would require that either the soft-term hierarchies discussed above are rendered stable under quantum corrections, or that the lightest states are revealed to exhibit further sequestering to higher powers of $1/\mathcal{V}$ such that a significant residual hierarchy is maintained. Given the aforementioned conceptual obstacles to realising this version of anisotropic modulus stabilisation, the prospect of simultaneously realising natural supersymmetry *and* an acceptable yield of dark radiation in this scenario, while very appealing, remains somewhat far-fetched.

Finally, we remark that if the recent claimed discovery of primordial B-modes by BICEP2 [17] holds up, estimates for the effective number of neutrino species could increase $N_{\rm eff}$ to values in the region of $(3.8 - 4) \pm 0.4$ at 68% c.l. [18–20]. Such values are significantly closer to the $\Delta N_{\rm eff} \gtrsim 1.4$ prediction of the Minimal LVS, so ultimately the minimal scenario may be saved after all.

Chapter 4

Soft X-ray Excess in the Coma Cluster from a Cosmic Axion Background

4.1 Introduction

This chapter is based on the paper [3], which was written in collaboration with Joseph P. Conlon, M.C. David Marsh, Andrew J. Powell and Lukas T. Witkowski.

In the previous chapters we have studied dark radiation production in the early Universe in the context of various string-inspired scenarios. However, we have not yet addressed the following: once this dark radiation is produced, what happens to it? In particular, does it generate any observable signals? The answer to the first question is that the axionic dark radiation does not interact with the thermal plasma, so it merely redshifts as radiation to the present day, forming a *Cosmic Axion Background* (CAB) — this process will be explained in more detail in section 4.2.

To approach the latter question we must abandon string model building for now; instead we must enter the multifarious realm of astrophysical phenomena. There is an immediate problem we must first overcome: the axionic dark radiation produced in string models typically interacts extremely weakly with Standard Model particles, since all the corresponding operators are suppressed by powers of $1/M_{\rm P}$. This implies that most means of detection will produce

impractically small signals that could not possibly lead to discoveries within our lifetimes. However, there are exceptions, and one of them is the topic to which we now turn.

This chapter presents the first systematic study of a proposed physical phenomenon, which if observed would forge a linkage between dark radiation, String Theory models of the early universe, and an excess in the spectrum of soft X-rays from galaxy clusters. Focussing on the Coma cluster, we give a detailed demonstration of how the observed cluster soft X-ray excess may emerge from axion-photon conversion of a homogeneous dark radiation $0.1 - 1\,\mathrm{keV}$ Cosmic Axion Background (CAB), which in turn arose from moduli decays in the early universe [70].

Galaxy clusters are the largest gravitationally bound objects in the universe and have historically served as powerful indicators of novel fundamental physics [71]. In addition to the dark matter component, which comprises around 80% of the cluster's mass, around 15% of the mass is in a hot ionised *intracluster medium* (ICM). ICMs typically have temperatures of $T \approx 10^8\,\mathrm{K}$ (corresponding to energies $\omega \approx 7\,\mathrm{keV}$) and particle number densities $n \sim 10^{-1} - 10^{-3}\,\mathrm{cm}^{-3}$. The ICM represents the large majority of a cluster's baryonic mass, and it generates diffuse X-ray emission through thermal bremsstrahlung.

To a good approximation, a thermal bremsstrahlung spectrum gives a constant emissivity per unit energy at low energies. However, observations of a large number of galaxy clusters have found evidence, at low energies around $E \lesssim 0.4\,\mathrm{keV}$, for excess emission above that from the hot ICM. This soft excess was initially observed in the Virgo and Coma clusters in 1996 [72–74] and has since been found in many other clusters [75, 76]. The observed X-ray emission from the Coma cluster is shown in Figure 4.1: at low energies there is a clear excess over the expected thermal bremmstrahlung profile.

There are two candidate astrophysical explanations: emission from a warm $T \approx 0.1$ keV gas; and inverse-Compton scattering of $\gamma \sim 300 - 600$ non-thermal electrons on the Cosmic Microwave Background (CMB). When placed under

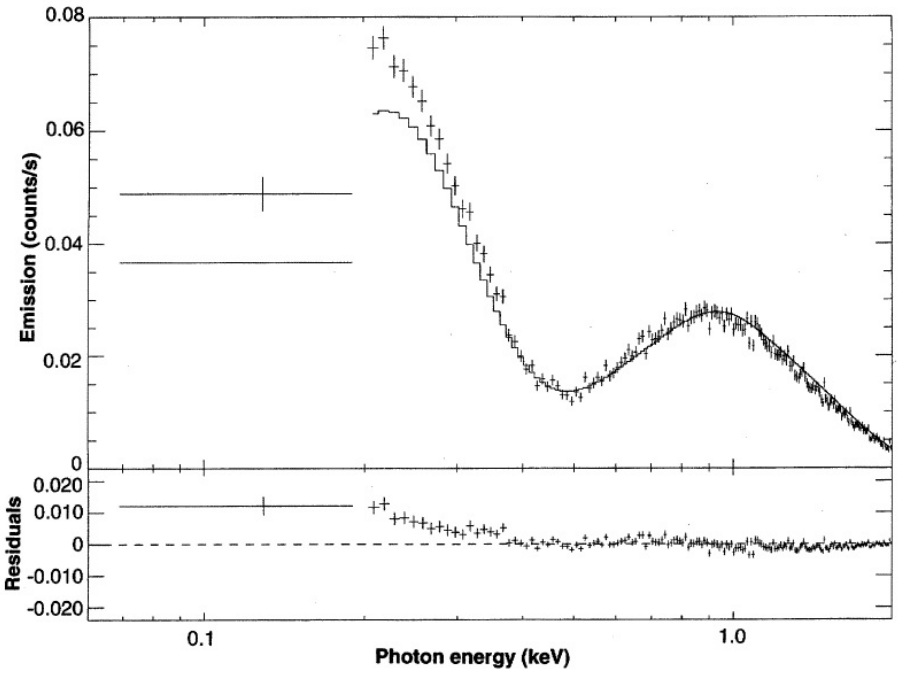

Fig. 2. Performance of the best fit MEKA single-temperature model (solid line) in a simultaneous fit to the EUVE DS and ROSAT PSPC data (the former is the first data point). The count rates correspond to those of the detected emission, and the residual is the difference between measured and model count rates.

Figure 4.1: The soft X-ray excess in the Coma cluster observed by Lieu et al. [73].

close scrutiny, both of these explanations encounter problems. The former explanation has difficulty with rapid cooling times of a warm gas and the lack of associated O_{VII} line emission; meanwhile, the latter has difficulty remaining consistent with the observed level of synchrotron radio emission as well as the failure to detect clusters in gamma rays. An in-depth discussion of both of these explanations, and their shortcomings, is given in [3].

In [70] the cluster soft excess was proposed to arise from conversion of a primordial Cosmic Axion Background into photons in the magnetic field of galaxy clusters. The Cosmic Axion Background has a non-thermal spectrum determined by the expansion of the universe during the time of moduli decay [77]. For moduli masses $m_\Phi \approx 10^6\,\mathrm{GeV}$ the present energy of these axions is $E_a \sim 0.1 - 1\,\mathrm{keV}$. The existence of such a CAB can be tested indirectly through its contribution to dark radiation, which in turn can be probed either by measurements of the CMB or through measurements of primordial BBN

abundances. The current hints at the 1-3 sigma level for a non-zero value of $\Delta N_{\rm eff}$ are not inconsistent with the presence of a CAB.

We stress that our focus in this chapter will be on *axion-like* particles. QCD axions have a particular relationship between their mass and the strength of their coupling to QCD. In this chapter we consider particles with general masses and axionic couplings to electromagnetism. We will normally take the ALP mass to be zero, although in practice the physics is unaffected for any mass $m_a \lesssim 10^{-12}\,\mathrm{eV}$. We also note that the physics we subsequently discuss here is not applicable to the QCD axion: the efficiency of conversion depends on the difference between the axion mass and the (effective) photon mass. For the QCD axion, its mass is too large to allow efficient conversion.

In the presence of a magnetic field, axions or axion-like particles can convert directly into photons via the coupling[1]

$$\mathcal{L}_{a\gamma\gamma} = \frac{1}{4M} a F_{\mu\nu}\tilde{F}^{\mu\nu} = \frac{1}{M} a\mathbf{E}\cdot\mathbf{B} \equiv g_{a\gamma\gamma} a\mathbf{E}\cdot\mathbf{B}\,. \tag{4.1}$$

In the enlightening case of sufficiently high axion energies or small ambient electron densities, the conversion probability for a fixed domain is given by

$$P_{a\to\gamma} = \frac{1}{4}\left(\frac{B_\perp L}{M}\right)^2\,, \tag{4.2}$$

where $B_\perp$ denotes the magnetic field component transverse to the axion velocity and L denotes the corresponding coherence length [78]. In related work, axion-photon conversion in cluster magnetic fields has been shown to have a detectable effect on the observed luminosities of Active Galactic Nuclei [79–81]. In our case, the conversion allows for the potential detection of a CAB through the cluster soft X-ray excess produced by axion-photon conversion.

The magnetic fields supported by galaxy clusters are typically modest in magnitude ($B \approx \mu$G) but are extended over megaparsec distances and have kiloparsec coherence scales, allowing observationally significant axion-photon

[1]Note that this coupling is present only in string compactifications where the lightest modulus originates, at least partly, from the cycle holding the visible sector.

conversion probabilities. In [70] a crude single-domain model with a magnetic field of fixed magnitude and coherence length was used to estimate the axion-photon coupling M that would be required to reproduce the soft excess in Coma from a CAB. It was found that the observed abundancce of dark radiation would be consistent with a value of $M \approx 10^{13}\,\mathrm{GeV}$.

The investigation presented here continues the study of axion-photon conversion in the Coma cluster using a far more detailed model of the Coma magnetic field. This model was constructed in [82] to fit rotation measure (RM) observations of seven polarised light sources, using the Coma cluster as a Faraday screen. The model describes the central Mpc^3 of Coma (see also [83] for a magnetic field model describing the region 1.5 Mpc to the southwest of the cluster centre). Using this stochastic model, we construct a numerical simulation of the magnetic field in the central region of the cluster, propagate axions through it, and quantitatively study the resulting predictions for the soft excess morphology.

This chapter is organised as follows. In section 4.2 I describe how a Cosmic Axion Background arises naturally in string models of the early universe. Following that, in section 4.3 I discuss observations of magnetic fields in galaxy clusters and review the magnetic field model proposed in [82] for the Coma cluster. In section 4.4 I detail the numerical method we used to simulate axion-photon conversion in the Coma cluster. The results of the simulation, and a comparison of the simulations to observations of the soft excess, are presented in section 4.5. Finally, I conclude in section 4.6 and discuss prospects for further work.

4.2 A Cosmic Axion Background

As we saw in Chapter 2 for the LARGE Volume Scenario, two-body decays of a modulus field in into axions are induced by a Lagrangian coupling of the form $\frac{\Phi}{M_P}\partial_\mu a \partial^\mu a$. This produces axions that have an initial energy $E_a = m_\Phi/2$. Since

these axions are weakly interacting (see, for example, [84]) they do not thermalise; instead, the vast majority propagate freely to the present day, where they form a homogeneous and isotropic Cosmic Axion Background. Furthermore, being relativistic, these axions contribute to the dark radiation energy density of the Universe.

Let us estimate the present-day energy of the axions in the CAB [77] in the instantaneous-decay approximation, under which all Φ particles decay at a time

$$\tau = \Gamma^{-1} = 8\pi \frac{M_{\rm P}^2}{m_\Phi^3} \, . \tag{4.3}$$

Since the universe is matter dominated until the point of modulus decay, the Hubble constant at the time of decay is $H_{\rm decay} = 2/3\tau$, with

$$H(\tau) \equiv H_{\rm decay} = \frac{1}{12\pi} \frac{m_\Phi^3}{M_{\rm P}^2} \, . \tag{4.4}$$

We assume Φ decays to the axion with branching ratio B_a and to the visible sector with branching ratio $B_{\rm SM} = (1 - B_a)$. The initial Standard Model energy density is

$$\rho_{\rm SM} = (1 - B_a) \times 3 H_{\rm decay}^2 M_{\rm P}^2 \, . \tag{4.5}$$

Furthermore, we assume instant thermalisation so that

$$\frac{\pi^2}{30} g_*(T_{\rm rh}) T_{\rm rh}^4 = (1 - B_a) \times 3 H_{\rm decay}^2 M_{\rm P}^2 \, . \tag{4.6}$$

This gives a reheating temperature of

$$T_{\rm rh} = \left(\frac{5(1 - B_a)}{8\pi^4 g_*(T_{\rm rh})} \right)^{1/4} \frac{m_\Phi^{3/2}}{M_{\rm P}^{1/2}} \, . \tag{4.7}$$

The initial axion energy is $E_a(T_{\rm rh}) = m_\Phi/2$. As the Universe expands, the axion energies redshift directly as $a(T)^{-1}$, whereas the photon energies redshift as $g_*^{-1/3} a(T)^{-1}$. Hence

$$\left(\frac{T_\gamma}{E_a} \right)_{\rm CMB} = \left(\frac{g_*(T_{\rm rh})}{10.75} \right)^{1/3} \left(\frac{11}{4} \right)^{1/3} \left(\frac{T_\gamma}{E_a} \right)_{\rm rh} \, . \tag{4.8}$$

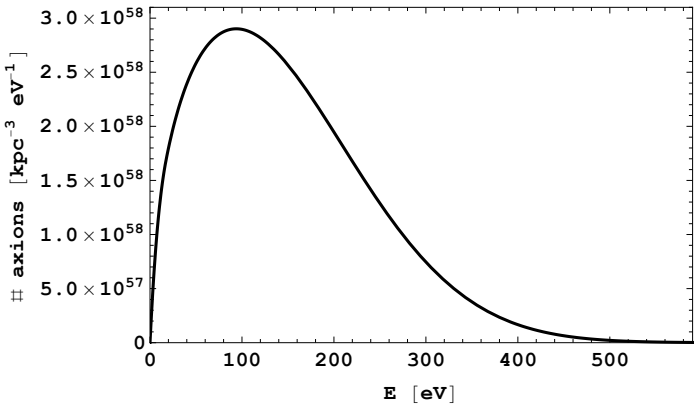

Figure 4.2: A typical axion number density per kpc^3 for a Cosmic Axion Background with $\langle E_{CAB} \rangle = 150\,\mathrm{eV}$, which contributes to dark radiation with $\Delta N_{\mathrm{eff}} = 0.5$. The precise location of the energy peak depends on the value of m_Φ.

This takes into account that there are two distinct boosts to the photon temperature as species become non-relativistic: one from the time of reheating to the time of neutrino decoupling, and the second from the time of neutrino decoupling to the present. We evaluate this to find

$$\left(\frac{E_a}{T_\gamma}\right)_{\mathrm{CMB}} = 2.78(1-B_a)^{-1/4}\left(g_*(T_{\mathrm{rh}})\right)^{-1/12}\left(\frac{M_{\mathrm{P}}}{m_\Phi}\right)^{1/2} . \tag{4.9}$$

For moduli masses $m \approx 10^6\,\mathrm{GeV}$, the present-day energy of the CAB is approximately $E_a \sim 10^6\,T_{\mathrm{CMB}} \approx 200\,\mathrm{eV}$.

To find the exact spectral shape of the CAB, we must account for the fact that moduli do not decay instantaneously, and meanwhile the expansion rate of the Universe changes as it transitions from matter (modulus) domination prior to reheating into radiation domination after all moduli have decayed. Moduli that decay early give rise to present-day axions with lower energies as they have had more time to redshift, whereas more energetic axions arise from late-decaying moduli. The spectral shape was computed numerically in [77] and may be described as 'quasi-thermal', with an exponential fall-off at high energies (c.f. figure 4.2). The overall magnitude is normalised to the axionic contribution to ΔN_{eff}, and the peak location is determined by the mass of the modulus and its lifetime.

While a CAB can be probed indirectly through studies of dark radiation, it can be observed directly only through its couplings to visible-sector matter and gauge bosons, as mediated, for example, by the operator

$$\frac{a}{M}\mathbf{E}\cdot\mathbf{B}\ .$$

In the presence of a magnetic field this induces 'oscillations' of axions into photons, in a process analogous to neutrino oscillations [78,85]. The observational consequences of this conversion of the CAB have been considered in [70,86,87]. Axions may also play a role by scattering off ambient particles in the thermal plasma, which was considered in [77].

By giving the value of M, the total axionic energy density and the central CAB energy, we have specified an entirely predictive model. In such a model, the spectrum and number of photons arising from axion-photon conversion in any astrophysical magnetic field can be computed.

4.2.1 What would a CAB tell us?

It is instructive to ask what could be learnt from the existence of a Cosmic Axion Background at a given energy E_a. We are going to assume that this is generated by the primordial non-renormalisable decays of a field Φ of mass m_Φ and coupling constant Λ, decaying at a rate

$$\Gamma = \frac{1}{8\pi}\frac{m_\Phi^3}{\Lambda^2}\ . \tag{4.10}$$

What would observations of a CAB tell us about m_Φ and Λ? In the following discussion we will make use of the ratio $E_a/T_{\rm CMB}$ (assumed to be measured) and the requirement that the reheating temperature must be greater than the BBN temperatures. Again we assume the instantaneous decay approximation,

$$\tau = \Gamma^{-1} = 8\pi\frac{\Lambda^2}{m_\Phi^3}\ . \tag{4.11}$$

While continual decays give a more refined analysis, here the instantaneous decay approximation is sufficient to capture the key physics.

Analogously to the above calculation, with this parametrisation we find that the reheating temperature is

$$T_{\rm rh} = \left(\frac{5(1-B_a)}{8\pi^4 g_*(T_{\rm rh})}\right)^{1/4} \frac{m_\Phi^{3/2} M_{\rm P}^{1/2}}{\Lambda} \,. \tag{4.12}$$

It follows that the present-day axion energy is now given by

$$\left(\frac{E_a}{T_\gamma}\right)_{\rm CMB} = 2.78(1-B_a)^{-1/4} g_*^{-1/12}(T_{\rm rh}) \frac{\Lambda}{m_\Phi^{1/2} M_{\rm P}^{1/2}} \,. \tag{4.13}$$

If we suppose a CAB is measured, then we fix $E_a/T_\gamma = \lambda$ as a measured parameter. What does this tell us? Note that we can write

$$T_{\rm rh} = 0.36 \left(\frac{10.75}{g_*(T_{\rm rh})}\right)^{1/3} \frac{m_\Phi}{\lambda} \,. \tag{4.14}$$

We now approximate $g_* \approx 10.75, B_a \approx 0$, and impose $T_{\rm rh} > 3\,{\rm MeV}$ for consistency with BBN. This gives

$$m_\Phi > 10\lambda\,{\rm MeV} \,, \tag{4.15}$$

or equivalently,

$$\Lambda \gtrsim 7 \times 10^{16} \left(\frac{\lambda}{10^6}\right)^{3/2} {\rm GeV} \,. \tag{4.16}$$

Thus the assumed observation of a CAB with energies in the few hundred eV range would imply the existence of an extremely weakly coupled particle whose interactions are suppressed by a scale $\Lambda \gtrsim 7 \times 10^{16}\,{\rm GeV}$. If we also impose $M_{\rm P} \geq \Lambda$, then we can bracket the mass and coupling of Φ:

$$\left(\frac{10^6}{\lambda}\right)^2 1.2 \times 10^7\,{\rm GeV} \gtrsim m_\Phi \gtrsim \left(\frac{\lambda}{10^6}\right) 10^4\,{\rm GeV} \,, \tag{4.17}$$

$$7 \times 10^{16}\,{\rm GeV} \lesssim \Lambda \lesssim M_{\rm P} \,. \tag{4.18}$$

An observation of a CAB can then be used to also show the existence of heavy massive particles that interact only through couplings suppressed by a scale close to the four-dimensional Planck scale — precisely the properties string compactifications predict for moduli.

4.3 Cluster magnetic fields

In this section we will discuss magnetic fields in galaxy clusters. First we briefly review the observational methods used to infer the existence of cluster magnetic fields, and then we review the magnetic field model of [82] used for the Coma cluster.

4.3.1 Magnetic fields in galaxy clusters

It is by now well-established that galaxy clusters support magnetic fields with typical field strengths of $\mathcal{O}(B) \sim 1\text{–}10\,\mu\mathrm{G}$. Observational studies of cluster magnetic fields are making steady progress, and here we briefly review the methods used to infer their existence and the resulting estimates for the magnetic field in the Coma cluster.

The first evidence for the existence of cluster magnetic fields was obtained from observations of the radio halo of the Coma cluster. This large region of diffuse radio emission extends to radii $> 1\,\mathrm{Mpc}$ from the centre of the cluster. The radiation from the halo cannot plausibly be associated with the integrated luminosity of the constituent galaxies — the only viable explanation is that it is synchrotron radiation from a diffuse population of relativistic electrons in the cluster magnetic field [88].

For the Coma radio halo, large-scale diffuse emission across the cluster has been measured at frequencies between 30 MHz and 4.5 GHz (for example see [89–91]). The total level of synchrotron emission correlates with the strength of the magnetic field, and the degree of polarisation serves as an indicator of field uniformity and structure. However, the actual magnitude of the magnetic field cannot be determined absolutely from synchrotron emissivity because of the degeneracy with the size of the electron population.

An estimate of the magnetic field strength can be made using 'equipartition' arguments, in which the total energy content of the synchrotron-emitting relativistic particles and magnetic field is minimised. Since such arguments

are always based on assumptions that may not be easily verifiable, equipartition arguments for magnetic field strengths can only give a rough indication of the average magnetic field across the radio halo. With this method, the radio emission may be attributed to the large-scale distribution of non-thermal relativistic electrons with GeV energies (i.e. with boost factor $\gamma \approx 2000$) subject to $\approx 1\,\mu$G magnetic fields. In particular, in [92] the Coma magnetic field averaged over the central $1\,\mathrm{Mpc}^3$ was estimated to be $B \sim 0.7 - 1.9\,\mu$G based on equipartition arguments.

The relativistic electrons responsible for the Coma radio halo will also inverse-Compton (IC) scatter off CMB photons to produce hard X-ray photons with frequencies around

$$\nu_{\mathrm{IC}} = \frac{4}{3}\gamma^2\nu_0 \sim \left(\frac{\gamma}{2000}\right)^2 4\,\mathrm{keV}\ . \tag{4.19}$$

More energetic electrons would similarly scatter CMB photons into gamma-rays. Thus in principle an observation of a hard X-ray inverse-Compton signal could be used to break the degeneracy between electron density and magnetic field size, allowing for a direct determination of the cluster magnetic field. In reference [93] this argument was used to estimate the Coma magnetic field as $B \approx 0.2\,\mu$G. However, more recent analysis of hard X-ray observations by numerous experiments shows no evidence of a non-thermal hard X-ray component in Coma, in which case the IC method leads only to lower limits on the magnetic field strength: $B > 0.2\,\mu$G for the Coma radio halo and $B > 1\,\mu$G for the Coma radio relic [94].

A fundamentally different method for estimating cluster magnetic fields comes from *Faraday rotation*. The magnetised ICM plasma induces different phase velocities for right-handed and left-handed photons and thus becomes birefringent. For linearly polarised light produced from e.g. synchrotron emission from localised radio sources, this leads to an effective rotation of the plane of polarisation of the wave as a function of wavelength. This effect is conve-

niently estimated in terms of a *rotation measure* (RM), defined by

$$\Psi_{\rm obs}(\lambda) = \Psi_0 + \lambda^2 \, {\rm RM} \; . \tag{4.20}$$

The rotation measure is given by the line-of-sight integral of the parallel component of the magnetic field multiplied by the electron density,

$${\rm RM} = \frac{e^3}{2\pi m_e^2} \int_{\rm l.o.s.} n_e(l) B_{\parallel}(l) \, {\rm d}l \; , \tag{4.21}$$

where, by convention, a magnetic field pointing towards the observer gives rise to a positive RM. Since the electron density distribution may be inferred from X-ray observations of the thermal ICM, studies of rotation measures provide a sensitive probe of the magnitude of the cluster magnetic field.

Thus, in principle, by measuring $\Psi_{\rm obs}$ at several frequencies for a given radio source, the value of RM may be inferred. The rotation measures typically exhibit a patchy structure across a radio source, and by studying the statistics of the RM distributions the scale over which the ICM magnetic field becomes tangled can be estimated. Finally, by considering a number of radio sources emitting linearly polarised light in and behind a galaxy cluster, the magnitude of the magnetic field, as well as its radial dependence, may be estimated. For a recent review, see [95].[2]

A number of studies of Faraday rotation measures in the Coma cluster have been performed. In [97] 18 radio sources were analysed and a significant enhancement of the RM towards the centre of the cluster was found. In order to estimate the magnetic field strength a simple model of the magnetic field reversal was used, in which the magnetic field and electron density were assumed to be constant in magnitude throughout the ICM, but the magnetic field orientation was assumed to perform a random walk with a fixed step size, Λ_B, corresponding to the magnetic field autocorrelation length. Such a model

[2]For a contrary view arguing that the rotation measure is attributed to the source radio galaxy and not the ICM as a whole, see [96].

always results in $\langle \mathrm{RM} \rangle = 0$, but with a variance proportional to the square of the magnetic field strength,

$$\sigma^2_{\mathrm{RM}} = 812 \Lambda_B \int_{\mathrm{l.o.s.}} \left(n_e(l) B_{\parallel}(l) \right)^2 \mathrm{d}l \ , \tag{4.22}$$

in units of radians^2/m^4. Using this model, the magnetic field strength was estimated as $B \approx 2\,\mu$G, with a tangling scale of $13 - 40\,$kpc.

In [98] RMs from the extended radio galaxy NGC 4869 in the Coma cluster were analysed, resulting in a field strength estimate of $B \lesssim 8.5\,\mu$G. Furthermore, the scale over which the magnetic field changes orientation was inferred to be $< 1\,$kpc. Since the mean of the rotation measure from the radio source was shown not to vanish, the simple random walk model was amended with a constant component of strength $\approx 0.2\,\mu$G uniform over $\approx 200\,$kpc.

More recently, better but computationally more expensive software tools have been designed to constrain the cluster magnetic field by simulating mock RM images from a magnetic field with a given power spectrum and by comparing the results to RMs obtained from radio observations [99, 100]. These allow a treatment of multi-scale magnetic fields. As we will review shortly,there are still some parameter degeneracies that complicate the final interpretation of this type of analysis, but the central magnetic field in Coma can be constrained to $B \sim 3 - 7\,\mu$G. An alternative semi-analytic method utilising Bayesian inference has also been developed [101].

In summary, observational evidence for cluster magnetic fields has been obtained by several independent methods, with observations of RMs from Faraday rotation giving the most direct estimate. These methods involve different theoretical assumptions and measure slightly different quantities (for example, average magnetic field in the case of synchrotron luminosity versus line-of-sight magnetic field for Faraday rotation). It is therefore not surprising that the resulting estimated field strength can differ by a factor of a few.

4.3.2 Coma magnetic field model

We now review the stochastic Coma magnetic field model of [82], which is based on the approach first proposed in [99]. In this model, the magnetic field in the Coma cluster is simulated as a multi-scale, tangled field with a field strength that scales with the electron density of the cluster. For certain model parameters, mock RMs derived from this magnetic field model were shown to be in good agreement with the RMs of radio sources observed in the central region of the Coma cluster with the Very Large Array (VLA) [82]. We note that while this model is a more sophisticated refinement of earlier models of the cluster magnetic field, it is still a model and cannot be expected to fully capture all features of a turbulent cluster magnetic field. Rather, this model presents a tractable approximation that has been shown to successfully reproduce some quantitative features of the true cluster field.

In the stochastic model of [82], the cluster magnetic field is constructed with a specified power spectrum. This is achieved via the generation of a random vector potential with a power spectrum

$$\langle |\tilde{A}_k|^2 \rangle \sim |k|^{-n} \, . \tag{4.23}$$

Such a vector potential may be constructed in momentum space by randomly drawing the magnitude of each component from a Rayleigh distribution,

$$p(\tilde{A}_k) = \frac{\tilde{A}_k}{|k|^{-n}} \exp\left(-\frac{\tilde{A}_k^2}{2|k|^{-n}} \right) , \tag{4.24}$$

where we have suppressed the vector index on $\tilde{A}_k$. The complex phase of each Fourier component of the vector potential is taken to be uniformly distributed between 0 and 2π. The momentum space magnetic field is then calculated as

$$\tilde{B}(k) = ik \times \tilde{A}(k) \tag{4.25}$$

and has a power-law power spectrum

$$P_{\tilde{B}} = \frac{1}{(2\pi)^3} \langle |\tilde{B}(k)|^2 \rangle \sim |k|^{-n+2} \, . \tag{4.26}$$

A tractable numerical simulation of this field requires the power spectrum to be truncated in the IR and UV. This is achieved by restricting the momenta to some range

$$k_{\min} \leq k \leq k_{\max} \ , \tag{4.27}$$

where in real space this corresponds to fields with structure only on scales larger than $\Lambda_{\min} = 2\pi/k_{\max}$ and smaller than $\Lambda_{\max} = 2\pi/k_{\min}$. The 'tangled' position-space magnetic field — which will automatically be divergence-free with normally distributed components, $B^i_{\text{gen.}}(x)$ — may then be obtained by Fourier transformation of $\tilde{B}(k)$. The real-space variance of the generated magnetic field is then given as usual by

$$\sigma_i^2 = \frac{1}{2\pi^2} \int_{k_{\min}}^{k_{\max}} \mathrm{d}k \, k^2 P_{\tilde{B}^i} \ . \tag{4.28}$$

While the generated magnetic field $\vec{B}(x)$ exhibits structure over a range of scales, it does not reproduce one of the key properties of cluster magnetic fields: the attenuation of the field strength with radius. Following [82], we note that such an attenuation can be modelled by enforcing that the magnetic field scales with the gas density of the hot intra-cluster medium. The density of the ICM in the central region of Coma is well described by the β-model,

$$n_e(r) = n_0 \left(1 + \frac{r^2}{r_c^2}\right)^{-\frac{3}{2}\beta} \ , \tag{4.29}$$

where the central electron density n_0, the core radius r_c, and β have been determined to be $3.44 \times 10^{-3}\mathrm{cm}^{-3}$, 291 kpc, and 0.75, respectively [102].

A more realistic model of the magnetic field may then be obtained by modulating $B^i_{\text{gen.}}(x)$ through multiplication by some function of the intracluster electron density, $f(n_e) = \mathcal{C} B_0 \left(\frac{n_e(r)}{n_0}\right)^{\eta}$. The constant $\mathcal{C}$ is chosen so as to normalise the average magnetic field across the core of the cluster to some parameter value B_0. The values η and B_0 are then two additional parameters of the model. By comparing simulated RMs from the above model with rotation measures inferred from VLA observations, the authors of [82] found the

best fit values $\eta = 0.5$ and $B_0 = 4.7\,\mu$G, but values in the ranges $\eta = 0.4$ to $\eta = 0.7$, with $B_0 = 3.9\,\mu$G and $B_0 = 5.4\,\mu$G, respectively, gave fits within 1σ of observations.

We note that the total cluster magnetic field,

$$\vec{B}^{\text{tot.}} := \mathcal{C} \cdot B_0 \cdot \left(\frac{n_e(r)}{n_0}\right)^{\eta} \vec{B}_{\text{gen.}}(r, \theta, \phi) \,, \tag{4.30}$$

is no longer divergence-free but receives local contributions from a fictitious magnetic monopole density proportional to $\vec{\nabla} n_e \cdot \vec{B}_{\text{gen.}}$. This contribution, however, is always proportional to $B_0 \frac{L}{r_c}$, where L is the coherence length of the magnetic field, and is negligible for $L \ll r_c$.

It is important to note that while the parameters n, Λ_{min}, Λ_{max}, η and B_0 can be constrained by fitting to rotation measures [82], there is an effective degeneracy between n and Λ_{max}. Larger n can be compensated for by lowering Λ_{max} and vice versa, giving an equally good fit to RMs obtained from Faraday rotation. The value $n = 17/3$ corresponds to a Kolmogorov-like turbulent power-law slope for the one-dimensional power spectrum of the magnetic field (defined here as $\mathcal{P}(k) \sim 2\pi k^2 |\tilde{B}_k|^2 \propto k^{-n+4}$) and was the headline value adopted in [82]. This power-law slope corresponds to a best fit value of $\Lambda_{\text{max}} = 34\,\text{kpc}$, with Λ_{min} found to be $2\,\text{kpc}$. However, as discussed in [82], the Faraday rotation measurements are degenerate along a curve in $(n, \Lambda_{\text{max}})$ space, giving a flatter spectrum as Λ_{max} is increased. Equally good fits to Faraday rotation measures are provided by a flat one-dimensional power spectrum, i.e. $n = 4$, with Λ_{max} increased to $100\,\text{kpc}$. These spectra have more power on small scales compared to the Kolmogorov spectrum.

4.4 The soft excess in Coma from the CAB

We now describe the implementation of a numerical simulation of axion-photon conversion of the CAB in magnetic fields generated stochastically using the magnetic field models described in section 4.3.

The simulation of axion-photon conversion in the Coma cluster can be divided into three steps: first, a stochastic magnetic field of the type consistent with observations of Faraday rotation measures is generated on a large lattice; second, an initial axion state of a particular energy is quantum mechanically propagated through this lattice; and finally, by normalising the initial axion distribution to the CAB spectrum derived in [77], the resulting photon luminosities and spectrum are obtained.

4.4.1 Magnetic field generation

Following the detailed prescription reviewed in section 4.3.2, we have generated a numerical model of the Coma magnetic field, on a 2000^3 grid with an $s = 0.5\,\mathrm{kpc}$ unit cell size, using C++. This way the Nyquist criterion, that the sampling rate of a dataset must be greater (ideally much greater) than twice the frequency of the dataset, is satisfied for fields with structure only on scales larger than $\Lambda_{\mathrm{min}} > 2s = 1\,\mathrm{kpc}$. We note that such a small unit cell size places a limit on the size of the field we can generate, making it impractical to go beyond $\approx 1\,\mathrm{Mpc}^3$.

As outlined in section 4.3.2, the values of the Fourier coefficients of the vector potential are generated randomly for all modes in the range of equation (4.27). After computing the momentum space magnetic field, the real space representation is obtained by performing a discrete Fourier transform using FFTW 3.3.3 routines [103].

The real-space magnetic field is modulated as in equation (4.30) so as to exhibit attenuation over cluster scales. The normalisation constant $\mathcal{C}$ is chosen so that the average magnitude of the magnetic field within the core radius, r_c, of the cluster is equal to the parameter B_0. In detail, this gives

$$\mathcal{C} = \frac{N_{r<r_c}}{\sum_{r<r_c} B_{\mathrm{gen.}} (\frac{n_e}{n_0})^{\eta}} \,, \tag{4.31}$$

where $N_{r<r_c}$ denotes the number of lattice points at radii less than the cluster radius.

As discussed in section 4.3.2, the observation of rotation measures from Faraday rotation does not completely determine the parameters of the stochastic model but rather restricts their values to certain degeneracy classes. In this analysis we consider three sets of magnetic field parameters, which are listed in table 4.1 on page 95.

4.4.2 Axion-photon propagation I: homogeneous solution

In the presence of an external magnetic field, axions and photons mix via the term

$$\mathcal{L} \supset \frac{1}{8M} a F_{\mu\nu} \tilde{F}^{\mu\nu} \equiv \frac{1}{M} a \vec{E} \cdot \vec{B} \equiv g_{a\gamma\gamma} a \vec{E} \cdot \vec{B} \, . \tag{4.32}$$

From the wave equation for particles propagating in the z-direction, the corresponding linearised equation of motion for the axion-photon system is [104]

$$\left(\omega + \begin{pmatrix} \Delta_\gamma & \Delta_\mathrm{F} & \Delta_{\gamma a x} \\ \Delta_\mathrm{F} & \Delta_\gamma & \Delta_{\gamma a y} \\ \Delta_{\gamma a x} & \Delta_{\gamma a y} & \Delta_a \end{pmatrix} - i\partial_z \right) \begin{pmatrix} |\gamma_x\rangle \\ |\gamma_y\rangle \\ |a\rangle \end{pmatrix} = 0 \, . \tag{4.33}$$

Here ω denotes the energy of the photon and axion modes and Δ_F denotes the Faraday rotation of photon polarisation states due to the cluster magnetic field. Since this mixing is between photons only, in the limit of small axion-photon mixing this effect is negligible and we will henceforth set it to zero. The refractive index for photons in the plasma is given by $\Delta_\gamma = -\omega_\mathrm{pl}^2/2\omega$, where $\omega_\mathrm{pl} = \sqrt{\frac{4\pi\alpha n_e}{m_e}}$ denotes the plasma frequency of the ICM. The axion-photon mixing is induced by the matrix element $\Delta_{\gamma a i} = B_i/2M$, and the mass of the axion determines the final diagonal matrix element, $\Delta_a = -m_a^2/\omega$. Formally we may write the general solution to equation (4.33) as

$$\begin{pmatrix} |\gamma_x\rangle \\ |\gamma_y\rangle \\ |a\rangle \end{pmatrix} (L) = \mathcal{T}_z \left[\exp\left(-i\omega L \mathbb{I} \; - i \int_0^L \mathcal{M}(z) \mathrm{d}z \right) \right] \begin{pmatrix} |\gamma_x\rangle \\ |\gamma_y\rangle \\ |a\rangle \end{pmatrix} (0) \, , \tag{4.34}$$

with

$$\mathcal{M}(z) = \begin{pmatrix} \Delta_\gamma(z) & 0 & \Delta_{\gamma a x}(z) \\ 0 & \Delta_\gamma(z) & \Delta_{\gamma a y}(z) \\ \Delta_{\gamma a x}(z) & \Delta_{\gamma a y}(z) & \Delta_a(z) \end{pmatrix} \, . \tag{4.35}$$

In direct analogy with the standard treatment of the Schrödinger equation in quantum mechanics, we have introduced the 'z-ordering' operator $\mathcal{T}_z$ in (4.34).

Before numerically integrating equation (4.33) for our inhomogeneous magnetic field model, it is illuminating to first consider the simpler case of a homogeneous electron density and magnetic field in some domain of size L (along the z-direction). In this case, the homogeneity makes the z ordering and the integral over dz trivial. Furthermore, since only photons with polarisation parallel to the magnetic field couple to axions, a simple rotation in the x-y plane reduces the non-trivial part of the problem to that of a 2-body system of $\left|\gamma_{\parallel}\right\rangle$ and $|a\rangle$. The non-trivial part of the z-evolution generator $\mathcal{M}$ can then be diagonalised by an orthogonal rotation by an angle θ, which satisfies

$$\tan\left(2\theta\right) = \frac{2\Delta_{a\gamma}}{\Delta_a - \Delta_\gamma}\,, \tag{4.36}$$

where now $\Delta_{a\gamma} = B/2M$.

The eigenvalues of $\mathcal{M}$ are $\lambda_\pm = \bar{\lambda} \pm \delta\lambda$, where $\bar{\lambda} = \frac{\Delta_a + \Delta_\gamma}{2}$ and

$$\delta\lambda = \frac{1}{2}\sqrt{(\Delta_a - \Delta_\gamma)^2 + 4\Delta_{a\gamma}^2}\,. \tag{4.37}$$

The z-propagation is now trivial and, expressed in the original basis, results in the oscillation of an initially pure axion state, $|i\rangle = (0,0,1)^T$, into the final state

$$\begin{pmatrix} \left|\gamma_\perp\right\rangle \\ \left|\gamma_{\parallel}\right\rangle \\ |a\rangle \end{pmatrix}(L) = \begin{pmatrix} 0 \\ e^{-i(\vartheta+\frac{\pi}{2})}\sin(2\theta)\sin(L\delta\lambda) \\ e^{-i\vartheta}\left(\cos(L\delta\lambda) + i\sin(L\delta\lambda)\left(1-2\sin^2\theta\right)\right) \end{pmatrix}\,, \tag{4.38}$$

where ϑ is a phase that will be unimportant for our discussion. Thus, in a single domain with a homogeneous magnetic field, the probability that an axion converts into a photon is given by

$$P(a\to\gamma) = \sin^2(2\theta)\sin^2\left(L\delta\lambda\right) = \sin^2(2\theta)\sin^2\left(\frac{\Delta}{\cos 2\theta}\right), \tag{4.39}$$

where $\tan 2\theta = \frac{2B_\perp\omega}{Mm_{\rm eff}^2}$, $\Delta = \frac{m_{\rm eff}^2 L}{4\omega}$ and $m_{\rm eff}^2 = m_a^2 - \omega_{\rm pl}^2$.

For a single domain with a coherent magnetic field, the axion-photon conversion probability is completely determined by the angles θ and Δ. For the

values of electron density and magnetic field relevant for galaxy clusters, and for the values of ω and M that we will consider, the θ angle is always in the small-angle approximation,

$$\theta \approx \frac{B_\perp \omega}{M m_{\rm eff}^2} = 8.1 \times 10^{-5} \left(\frac{n_0}{n_e}\right) \left(\frac{B_\perp}{1\,\mu{\rm G}}\right) \left(\frac{\omega}{200\,{\rm eV}}\right) \left(\frac{10^{13}\,{\rm GeV}}{M}\right) . \quad (4.40)$$

Here, as in (4.29), n_0 denotes the central electron density in the Coma cluster, $n_0 = 3.44 \times 10^{-3}\,{\rm cm}^{-3}$. By contrast, the angle Δ is not always small in clusters,

$$\Delta = 0.93 \left(\frac{n_e}{n_0}\right) \left(\frac{200\,{\rm eV}}{\omega}\right) \left(\frac{L}{1\,{\rm kpc}}\right) . \quad (4.41)$$

We will find that much of the structure of CAB conversion in galaxy clusters can be understood in terms of the transition of Δ between the small-angle and large-angle regimes.

Finally, for $\Delta \ll 1$ and $\theta \ll 1$, the axion-photon conversion probability takes the simple form

$$P(a \to \gamma) = 2.3 \times 10^{-8} \left(\frac{B_\perp}{1\,\mu{\rm G}} \frac{L}{1\,{\rm kpc}} \frac{10^{13}\,{\rm GeV}}{M}\right)^2 . \quad (4.42)$$

While equations (4.39) and (4.42) are not directly applicable to axion-photon conversion in clusters, we will still find them very useful for understanding the general qualitative properties of axion-photon conversion.

4.4.3 Axion-photon propagation II: inhomogeneous magnetic fields

The axion-photon conversion probabilities are computed by numerically simulating the propagation of an axion through our discretised implementation of the magnetic field model discussed in section 4.3. Since the lattice spacing of 0.5 kpc is much smaller than the cluster core radius $r_c = 291\,{\rm kpc}$, the electron density varies slowly over each zone of constant magnetic field and may consistently be approximated as constant within each lattice zone. Thus within each zone the unitary "z-evolution" matrix is constant, and equation (4.34) can be

solved recursively from the nth lattice point to the next,

$$\begin{pmatrix} |\gamma_x\rangle \\ |\gamma_y\rangle \\ |a\rangle \end{pmatrix}_{n+1} = \exp\left(-i\omega s\mathbb{I} - i \begin{pmatrix} \Delta_{\gamma,n} & 0 & \Delta_{\gamma ax,n} \\ 0 & \Delta_{\gamma,n} & \Delta_{\gamma ay,n} \\ \Delta_{\gamma ax,n} & \Delta_{\gamma ay,n} & \Delta_{a,n} \end{pmatrix} s \right) \begin{pmatrix} |\gamma_x\rangle \\ |\gamma_y\rangle \\ |a\rangle \end{pmatrix}_n , \tag{4.43}$$

where we have again denoted the lattice spacing by s. This way, an initial pure axion state will develop non-vanishing photon components as the state propagates through the cluster.

The solution to equation (4.43) is obtained, just as in the single-domain case, by first rotating to a basis in which the magnetic field is aligned with one of the coordinate axes and then diagonalising the non-trivial part of the z-propagation generator. This way, the axion-photon propagation can be solved exactly for each lattice point. The propagation of the full 3-body system through the lattice is then achieved recursively by diagonalising, propagating the new fields to the next grid point, and finally rotating back to obtain the state with respect to the original reference basis. Thus the state at the $(n+1)$th step is given by

$$|n+1\rangle = U_{1,n}^{\mathrm{T}} U_{2,n}^{\mathrm{T}} \mathcal{M}_n U_{2,n} U_{1,n} |n\rangle , \tag{4.44}$$

where $U_{1,n}$ denotes the rotation required to align a coordinate axis with the local magnetic field direction, and $U_{2,n}$ denotes the diagonalisation of the unitary z-evolution operator at the nth step.

The probability of the axion converting into a photon is then computed as the sum of the squares of the $|\gamma_x\rangle$ and $|\gamma_y\rangle$ components of the final state. This procedure is done for each of the 2000^2 grid points in the x-y plane for 14 energies in the $25\,\mathrm{eV} - 2\,\mathrm{keV}$ range and for a vanishing axion mass. By setting the axion mass to zero we make the approximation that m_{eff}^2 is dominated by the plasma frequency. The plasma frequency is

$$\omega_{\mathrm{pl}} = 1.2 \times 10^{-12} \sqrt{\frac{n_e}{10^{-3}\mathrm{cm}^{-3}}}\,\mathrm{eV} \tag{4.45}$$

and is never much less than $\approx 10^{-12}\,\mathrm{eV}$ in the system we are considering. Therefore, axion masses $m_a \leq 10^{-13}\,\mathrm{eV}$ behave equivalently to a vanishing

axion mass. For masses $m_a \gg 10^{-12}\,\mathrm{eV}$ (including the case of a QCD axion), $\theta \sim 1/m_a^2$ and $\Delta \sim m_a^2$, so it is reasonable to expect that the conversion probabilities become suppressed relative to those we have obtained by a factor of $(10^{-13}\,\mathrm{eV}/m_a)^4$. For an axion mass $m_a \approx 10^{-12}\,\mathrm{eV}$, detailed simulation would be required to study the resulting morphology and how it differs from the zero-mass case.

4.4.4 Analysing the simulation data

The simulation generates a 2000^2 grid of $a \to \gamma$ conversion probabilities, each representing the probability of a single axion at energy ω, traversing Coma through a unit of cross-sectional area $(0.5\,\mathrm{kpc})^2$, converting into a photon of the same energy. We need to convert these probabilities into intrinsic source luminosities. Coma is at a well-determined redshift of $z = 0.023$. We use the parameters from the magnetic field model of [82] with $H_0 = 71\,\mathrm{km\,s^{-1}\,Mpc^{-1}}$, corresponding to an angular scale of 0.460 kpc per arcsecond and a luminosity distance of 98.9 Mpc.[3] We note that the soft excess analysis of [75] assumed a Hubble constant of $H_0 = 75\,\mathrm{km\,s^{-1}\,Mpc^{-1}}$, which corresponds instead to an angular scale of 0.434 kpc per arcsecond and a luminosity distance to Coma of 93.6 Mpc. However, these differences are small enough to be neglected compared to the other statistical and systematic uncertainties in the extraction of the soft excess.

The overall CAB energy density is $\rho_{\mathrm{CAB}} = \Delta N_{\mathrm{eff}} \frac{7}{8} \left(\frac{4}{11}\right)^{4/3} \rho_{\mathrm{CMB}}$. Associated with this is a CAB number density $\mathrm{d}N_a/\mathrm{d}E$ set by the spectral shape, such that

$$\int \mathrm{d}E\, E\, \frac{\mathrm{d}N_a}{\mathrm{d}E} = \rho_{\mathrm{CAB}}\ .$$

In terms of these the intrinsic excess luminosity associated with axion-photon conversion is given by

$$\mathcal{L}_{\mathrm{excess}} = D_{\mathrm{Coma}}^2 \int \mathrm{d}\Omega \mathrm{d}E\, E\, \frac{\mathrm{d}N_a}{\mathrm{d}E}\, c P_{a\to\gamma}(\Omega, E)\ , \tag{4.46}$$

[3] See [105] for a redshift-distance converter.

	Model 1	Model 2	Model 3
$\Lambda_{\min}$	$2\,\mathrm{kpc}$	$2\,\mathrm{kpc}$	$2\,\mathrm{kpc}$
$\Lambda_{\max}$	$34\,\mathrm{kpc}$	$5\,\mathrm{kpc}$	$100\,\mathrm{kpc}$
n	$17/3$	$17/3$	4
B_0	$3.9 - 5.4\,\mu\mathrm{G}$	$5.4\,\mu\mathrm{G}$	$5.4\,\mu\mathrm{G}$
η	$0.4 - 0.7$	0.7	0.7

Table 4.1: The parameter values for the three simulations used. The first simulation (Model 1) is a Kolomogorov spectrum that fits the Faraday rotation data. The best fit values of B_0 and η are $4.7\,\mu$G and 0.5, respectively; the range considered in Model 1 corresponds to the 1σ allowed values of these two parameters. The second simulation (Model 2) is designed to show the effect of concentrating all power on small scales but is not a fit to Faraday rotation data. The third simulation (Model 3) is a flat spectrum (in k-space) that fits Faraday rotation data and has most power on small scales.

where D_{Coma} is the physical distance to Coma and $\mathrm{d}\Omega$ is a solid angle element (measured in arcmin^2). We will restrict the energy integral to the $0.2 - 0.4\,\mathrm{keV}$ range, in accordance with [75].

4.5 Results

Here we discuss the results of the numerical simulation of the conversion probabilities, and we present a detailed description of the predictions for the cluster soft excess in the CAB conversion scenario. We discuss both particular and generic features of the generated photon flux, and we compare our results for axion-photon conversion of the CAB to the observed soft excess luminosities in Coma [75].

4.5.1 General features of axion-photon conversion

While several properties of the simulated conversion probabilities and soft X-ray luminosities are sensitive to the detailed magnetic field model, there are also general features that are shared by all models we have considered. We highlight these properties by using Model 1 of table 4.1 as our main example. In this model, the stochastic magnetic field is generated with a Kolmogorov power

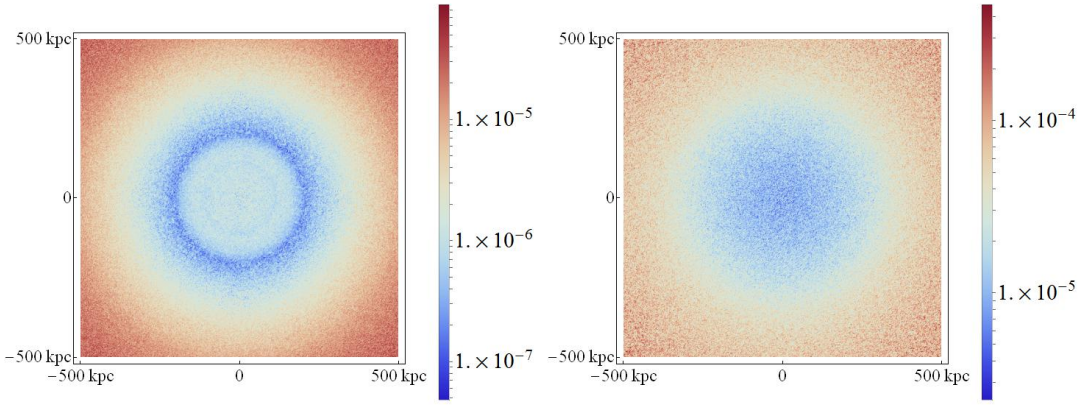

(a) 25 eV (b) 50 eV

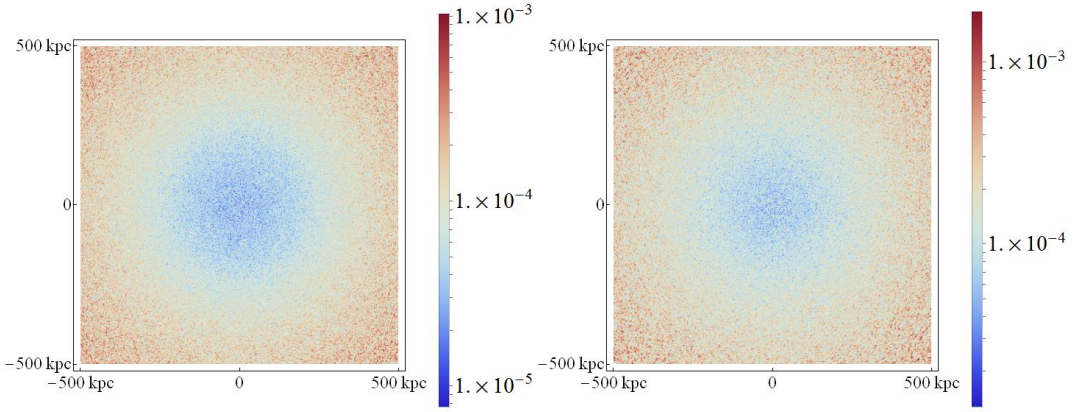

(c) 75 eV (d) 100 eV

Figure 4.3: Conversion probabilities for energies 25 eV to 100 eV for Model 1, with $\eta = 0.5$, $B_0 = 4.7\,\mu$G and $M = 7 \times 10^{12}$ GeV. Note that different colour schemes have been used in each plot.

spectrum ($n = 17/3$), with coherence lengths in the range $2 - 34$ kpc. The best-fit values of the scaling of the total magnetic field with electron density, η, and the central value of the magnetic field, B_0, are then $\eta = 0.5$ and $B_0 = 4.7\,\mu$G, respectively.

The simulated conversion probability maps for this model are shown in figures 4.3, 4.4 and 4.5 with a pixel size of $(2\,\text{kpc})^2$. Figure 4.6 shows the conversion probabilities as a function of the impact parameter, for 8 energies from 25 keV to 2 keV.

These figures illustrate two key features of the results that are ubiquitous

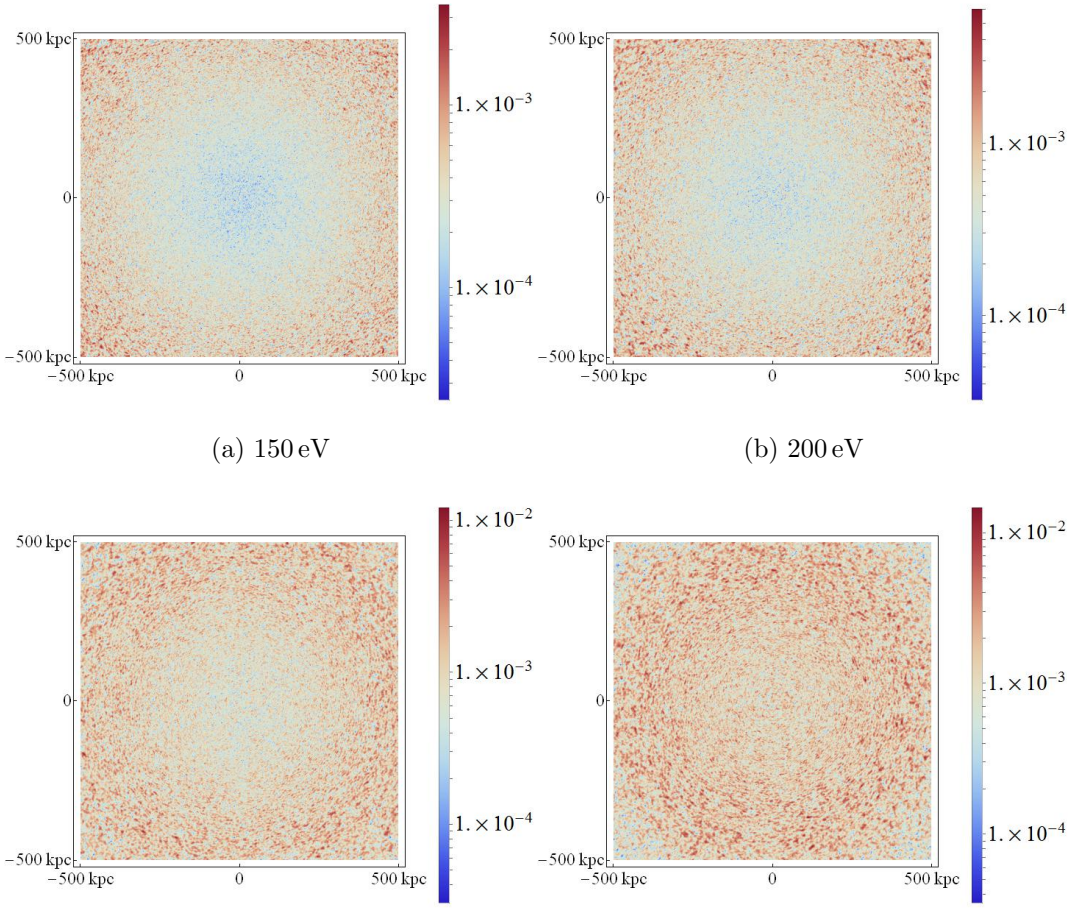

(a) 150 eV (b) 200 eV

(c) 300 eV (d) 400 eV

Figure 4.4: Conversion probabilities for energies 150 eV to 400 eV for Model 1, with $\eta = 0.5$, $B_0 = 4.7\,\mu$G and $M = 7 \times 10^{12}$ GeV. Note that different colour schemes have been used in each plot.

in all the magnetic field models we have studied. First, the overall conversion probabilities increase with energy, up to a maximal energy at which they saturate.

Second, the morphology of the conversion probabilities is quite distinct at low and high energies. At low energies, the conversion probabilities are lowest for axions that pass through the very centre of the cluster. As a function of increasing impact parameter, the conversion probabilities increase, reach a maximum at some intermediate radius, before again decreasing towards the edge of the cluster. This behaviour is clearly visible in the 400 eV plot (figure 4.4d)

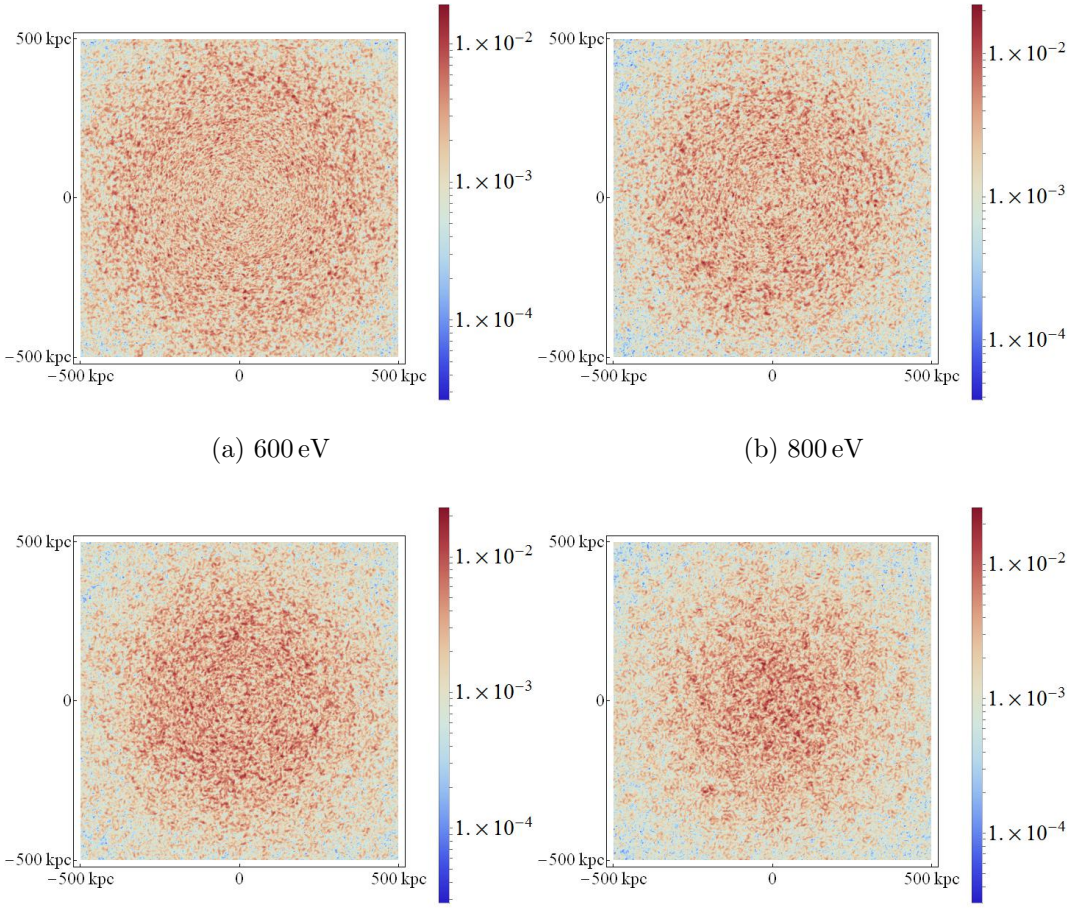

(a) 600 eV (b) 800 eV

(c) 1000 eV (d) 2000 eV

Figure 4.5: Conversion probabilities for energies 600 eV to 2 keV for Model 1, with $\eta = 0.5$, $B_0 = 4.7\,\mu$G and $M = 7 \times 10^{12}$ GeV. Note that different colour schemes have been used in each plot.

— for lower energies than this the point of maximal conversion probability lies beyond the range of the simulation. At ultra-low energies (c.f. the 25 eV plot, figure 4.3a), a curious, unanticipated ring-like structure is visible. Here the conversion probabilities increase, decrease, and then increase again. We discuss the origin of this at greater length below.

In contrast, higher energy axions have a maximal conversion probability at the centre of the cluster, with a monotonic decrease in conversion probability upon going to larger radii. A crossover between the high-energy regime of 'central dominance' and the low-energy regime of 'central deficit' can be observed

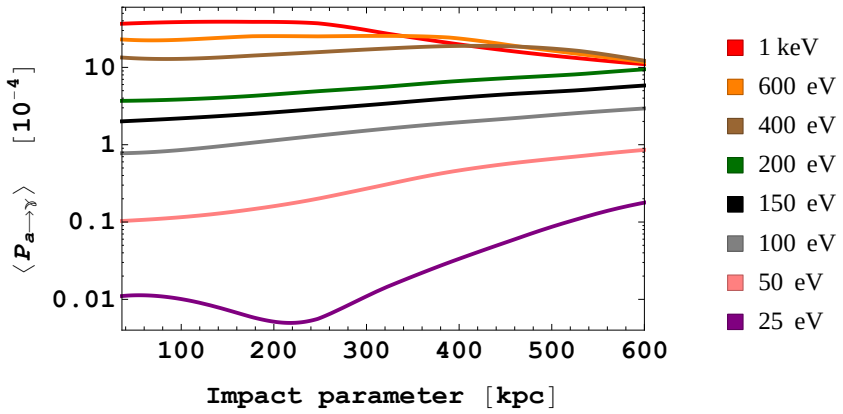

Figure 4.6: Conversion probabilities as a function of impact parameter for Model 1 with $\eta = 0.5$ and $B_0 = 4.7\,\mu$G.

for modes with energies of $400\,\text{eV} < \omega < 1\,\text{keV}$ in Model 1.

In fact, both these generic features of the conversion probabilities can be understood from the single-domain solution of equation (4.39), even though it is not fully applicable to the multi-scale fields considered here. The single domain conversion probability is (to leading order in θ) given by

$$P(a \to \gamma) \propto B_0^2 \frac{\tilde{\omega}^2}{M^2} \tilde{n}(r)^{2(\eta-1)} \sin^2\left(0.93 \frac{\tilde{L}\tilde{n}(r)}{\tilde{\omega}}\right) , \tag{4.47}$$

where $\tilde{n}(r) = n_e(r)/n_0$, $\tilde{L} = L/(1\,\text{kpc})$ and $\tilde{\omega} = \omega/(200\,\text{eV})$. Here we have factored out the dependence of the total magnetic field on the electron density, as in equation (4.30). The fractional electron density $\tilde{n}(r)$ is completely determined by the β-model, c.f. equation (4.29), and decreases from unity at the cluster centre to ≈ 0.15 at $r = 600\,\text{kpc}$.

We now note that for either sufficiently large ω or sufficiently small $\tilde{n}(r)$, the argument of the sin function becomes small. In the small-Δ approximation the conversion probabilities are given by

$$P(a \to \gamma)_{\text{single domain}} \propto \frac{B_0^2 L^2}{M^2} \tilde{n}_e^{\eta}(r) , \tag{4.48}$$

$$P(a \to \gamma)_{\text{per unit length}} \propto \frac{B_0^2 L}{M^2} \tilde{n}_e^{\eta}(r) . \tag{4.49}$$

Thus, according to the single-domain formula, the small-θ *and* small-Δ approximations should be valid sufficiently far away from the cluster centre for all energies above a certain cut-off. Evidently, at large radii the small-angle approximation appears as an 'attractor', with a radial dependence completely determined by the modulation of the magnetic field with $\tilde{n}(r)^{\eta}$.

As the impact parameter is decreased and $\tilde{n}(r)$ increases, some modes will cease to be well described by the small-Δ approximation and will rather require the full equation (4.47). Such modes will leave the small-angle 'attractor' solution. According to the single-domain formula, modes with sufficiently low energies may undergo several 2π rotations of Δ as the impact parameter is decreased towards the centre of the cluster, and these modes in particular will exhibit rings of decreased probabilities as Δ comes close to an integer multiple of π.

However, for an axion traversing multiple magnetic field domains with slightly varying electron densities and coherence lengths, some of the detailed features of the single-domain probabilities can be expected to be 'washed out'. In particular, in the large-Δ regime it is reasonable to approximate $\langle \sin^2 \Delta \rangle = \frac{1}{2}$ for axions traversing multiple domains of slightly varying size. Then for $B \propto B_0 n_e^{\eta}$, we have

$$P(a \to \gamma)_{\text{single domain}} \propto \frac{B_0^2 \tilde{\omega}^2}{M^2} \tilde{n}_e^{2(\eta-1)} , \tag{4.50}$$

$$P(a \to \gamma)_{\text{per unit length}} \propto \frac{B_0^2 \tilde{\omega}^2}{LM^2} \tilde{n}_e^{2(\eta-1)} . \tag{4.51}$$

Since we consider $\eta < 1$ in all cases, this gives increasing conversion probabilities as the electron density decreases with radii. This increase will continue until the small-Δ regime is reached, where the conversion probability is again described by equation (4.48).

We now note that several of the features predicted from the single-domain formula also appear in the radial probabilities emerging from the full numerical simulation with multi-scale magnetic fields, c.f. figures 4.6 and 4.7a. From

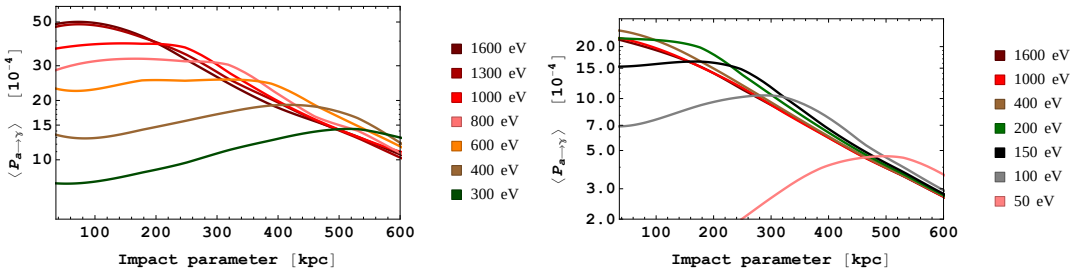

(a) Model 1 (b) Model 2

Figure 4.7: At large impact parameter the conversion probabilities tend towards the small angle approximation, as illustrated here for Model 1 and Model 2.

these figures, we see that modes with $\omega \gtrsim 400\,\mathrm{eV}$ have equal conversion probabilities at large radii (small $\tilde{n}(r)$), consistent with these modes entering the small-Δ approximation. At smaller impact parameter (corresponding to larger maximal $\tilde{n}(r)$), the lower-energy modes begin to decouple from the small-Δ approximation; this results in a decrease in the probabilities, which is perfectly consistent with the single-domain result. Only the highest-energy modes stay in the attractor curve for any impact parameter, as illustrated in figure 4.7a by the modes with $\omega = 1300\,\mathrm{eV}$ and $\omega = 1600\,\mathrm{eV}$.

The single-domain analysis also predicts the presence of regions with highly suppressed conversion probabilities as Δ approaches an integer multiple of π, and we note that this feature most likely explains the ring structure of the conversion probability in the 25 eV plot.

We can use the qualitative consistency of the conversion probabilities with the single-domain result to generate a heuristic estimate of an 'effective coherence length' of the magnetic field. For the high-energy modes in figure 4.7a we have argued that $\Delta \ll 1$ at large impact parameter, and we may heuristically associate the radius of maximum conversion probability, $r_{\max}(\omega)$, for each mode with the phase $\Delta = \pi/2$ in the single-domain formula. By furthermore noting that the largest contribution to the conversion probability for modes close to the small-Δ approximation will come from the region closest to the

cluster centre, we have

$$\frac{\pi}{2} = 0.93 \frac{\tilde{L}\tilde{n}(r_c(\omega))}{\tilde{\omega}} \,. \tag{4.52}$$

From this formula, we can extract an 'effective coherence length' $\tilde{L}$ for each mode that has a peaking conversion probability within the range studied. For Model 1 this range corresponds to modes with energies $300\,\mathrm{eV} \leq \omega \leq 1\,\mathrm{keV}$, as indicated in figure 4.7a. The decoupling of all modes is consistent with the single-domain estimate for effective coherence lengths in the $13 - 15\,\mathrm{kpc}$ range. In comparison, the full numerical simulation involves magnetic fields coherent over all scales from 2 kpc to 34 kpc, with a mean coherence length of $\approx 10\,\mathrm{kpc}$.

The single-domain intuition also holds for other magnetic field models. From figure 4.7b, we note that Model 2 may be associated with an 'effective coherence length' of the magnetic field in the $2.0 - 2.2\,\mathrm{kpc}$ range, based on the peak positions of modes with $50\,\mathrm{eV} < \omega < 200\,\mathrm{eV}$. The full multi-scale model has coherence lengths in the $2 - 5\,\mathrm{kpc}$ range, with a mean value of 3.2 kpc. These estimates indicate that the physical picture of axion-photon conversion motivated by the single-domain analysis is also quite accurate for more complicated magnetic field configurations such as the multi-scale configurations considered in this chapter.

Model 3 is distinguished by having the largest range of scales in the magnetic field, from $2 - 100\,\mathrm{kpc}$. As we see in figure 4.8, for this model the conversion probabilities have not converged to a small-angle approximation at large radius ($500 - 600\,\mathrm{kpc}$). We can again understand this behaviour using the single-domain formula.

The greater range of coherence lengths implies that even axions traversing the cluster at large impact parameter are likely to encounter domains in which the small-Δ approximation is not valid. Increasing ω always has the effect of decreasing Δ and thereby bringing a larger fraction of the traversed distance into the small-angle approximation, which results in an increased overall conversion probability according to equations (4.49) and (4.51). This explains the

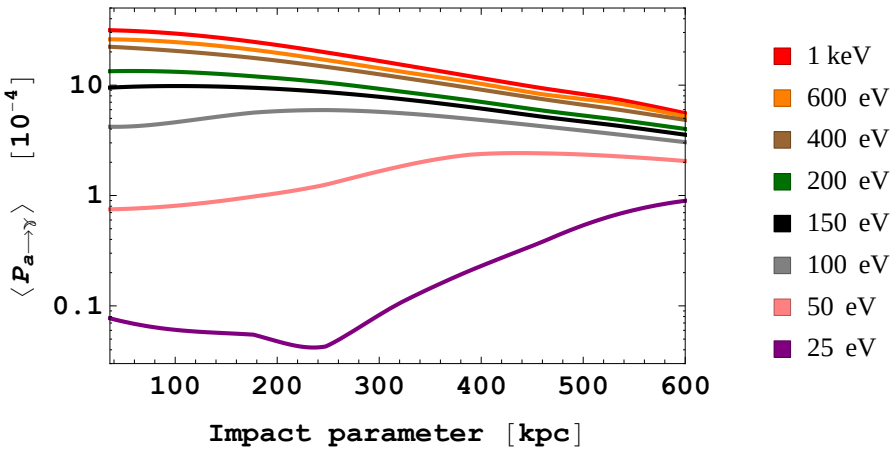

Figure 4.8: Mean conversion probability as a function of radius from the centre of Coma, for Model 3 of table 4.1 and with $M = 5.7 \times 10^{12}$ GeV.

increase in conversion probabilities with ω in Model 3, even at the largest radii.

A further difference in figure 4.8 compared to figures 4.7a or 4.7b can also be understood. For Model 3, at large radii the conversion probabilities are roughly similar for the higher energy modes, with consistent small increases upon going to higher energy. This behaviour is absent for Models 1 and 2. We can understand this through the different power spectra of the models. For the Kolmogorov spectra of models 1 and 2, power dominantly lies in the largest coherence lengths. The conversion probabilities are then highly suppressed for axion modes that have insufficient energy to reach the small-Δ regime, given this range of coherence lengths. For the truncated spectrum of Model 2 and the flat spectrum of Model 3, more power of the magnetic field is allocated to shorter scales, and even lower energy modes can reach the small-Δ approximation. Owing to the wide range of coherence length in the Model 3 magnetic field, axions traversing the cluster will still pass through regions which are not well described by a small-Δ approximation — even for relatively high energy modes. As the axion mode energy is increased, only a small additional fraction of the large coherence lengths are brought into the small-Δ approximation, which explains the gradual approach to the small-Δ approximation in this case.

Let us finally for the sake of clarity remark on features of the conversion probabilities that are not well-captured by the single-domain formula. As Δ approaches $\pi/2$, the single-domain formula predicts a relative decrease in the conversion probability with respect to the small-Δ approximation, yet the full numerical simulations exhibit conversion probabilities with a clear trend of 'overshooting' the small-angle attractor at this point.

A final general comment about the simulations: it is useful to know how much variation one can expect purely from repeating a simulation with identical magnetic field parameters. By repeating simulations with the Model 1 parameters, we found that the averaged conversion probabilities within each annulus varied by at most 9%, where in most cases the difference was less than 5%. We note that the most significant variations occurred for larger energies. We thus conclude that our magnetic field model does not generate large fluctuations in conversion probabilities. However, to account for this when we plot comparisons between simulated and observed luminosities, we include a statistical error of 10% on our values.

4.5.2 Comparison with observed luminosities

We may now compare the predictions of axion-photon conversion of a CAB in the Coma cluster to the actual observations of the soft excess by ROSAT, based on the analysis of Bonamente et al. [75]. Specifically, we will focus on the overall unabsorbed excess luminosity in the $0.2 - 0.4\,\mathrm{keV}$ band for various different annular regions around the centre of Coma.

The precise spectral shape of the soft excess is poorly known. In light of this fact, the analysis of [75] quotes results for two different spectral fits to the *excess* emission only (where the background thermal bremmstrahlung emission from the hot ICM has already been subtracted): the first employs a power-law spectrum with photon index 1.75 (so that the excess flux is $\mathrm{d}N_\gamma/\mathrm{d}E \sim \nu^{-1.75}$), and the second is based on a thermal spectrum with $T = 80\,\mathrm{eV}$. These results — which differ from each other by an overall factor of ≈ 2.4 — are shown in

Region (arcminute)	$L_{NT}(10^{41}\text{erg s}^{-1})$	$L_{thermal}(10^{41}\text{erg s}^{-1})$
0 - 3	11	4.6
3 - 6	22	9.1
6 - 9	26	10
9 - 12	25	10
12 - 18	47	21

Table 4.2: The results of [75] for excess luminosity from the Coma cluster.

table 4.2. While neither of these spectral models are in exact agreement with the shape of the photon spectrum obtained from CAB conversion (which we will discuss in more detail at the end of this section), the thermal bremsstrahlung spectrum has an exponentially decreasing tail in the $0.2-0.4\,\text{keV}$ range, as does the CAB spectrum for mean axion energies $\langle E_{\text{CAB}}\rangle \lesssim 200\,\text{eV}$. We will therefore use the thermal excess luminosities of table 4.2 when comparing the predictions of our model to the data. We also note that the model uncertainty in the extraction of the soft excess mostly affects the overall luminosity and, to a much smaller degree, its spatial distribution. In our model the overall luminosity has a simple dependence on the values of M and ΔN_{eff}, and the uncertainty in the overall luminosity translates into an uncertainty in $\Delta N_{\text{eff}}/M^2$.

We will now present our main results for the CAB explanation of the soft excess in Coma. First we will discuss luminosities from axion-photon conversion in the Model 1 magnetic field (including 1σ variations of the model parameters η and B_0), and we will then turn to Model 2 and Model 3.

Model 1: Figure 4.9 shows the comparison between the observed (thermal) excess luminosity and that produced by the baseline model of [82] as well as two other models related by 1σ variations of the model parameters. The integrated luminosity in the $0.2-0.4\,\text{keV}$ range has been normalised to the total luminosity of the soft excess in the same range by varying M independently for each model. In all cases $\Delta N_{\text{eff}} = 0.5$ has been assumed, but we emphasise that alternate values for these parameters that normalise luminosities can be obtained by

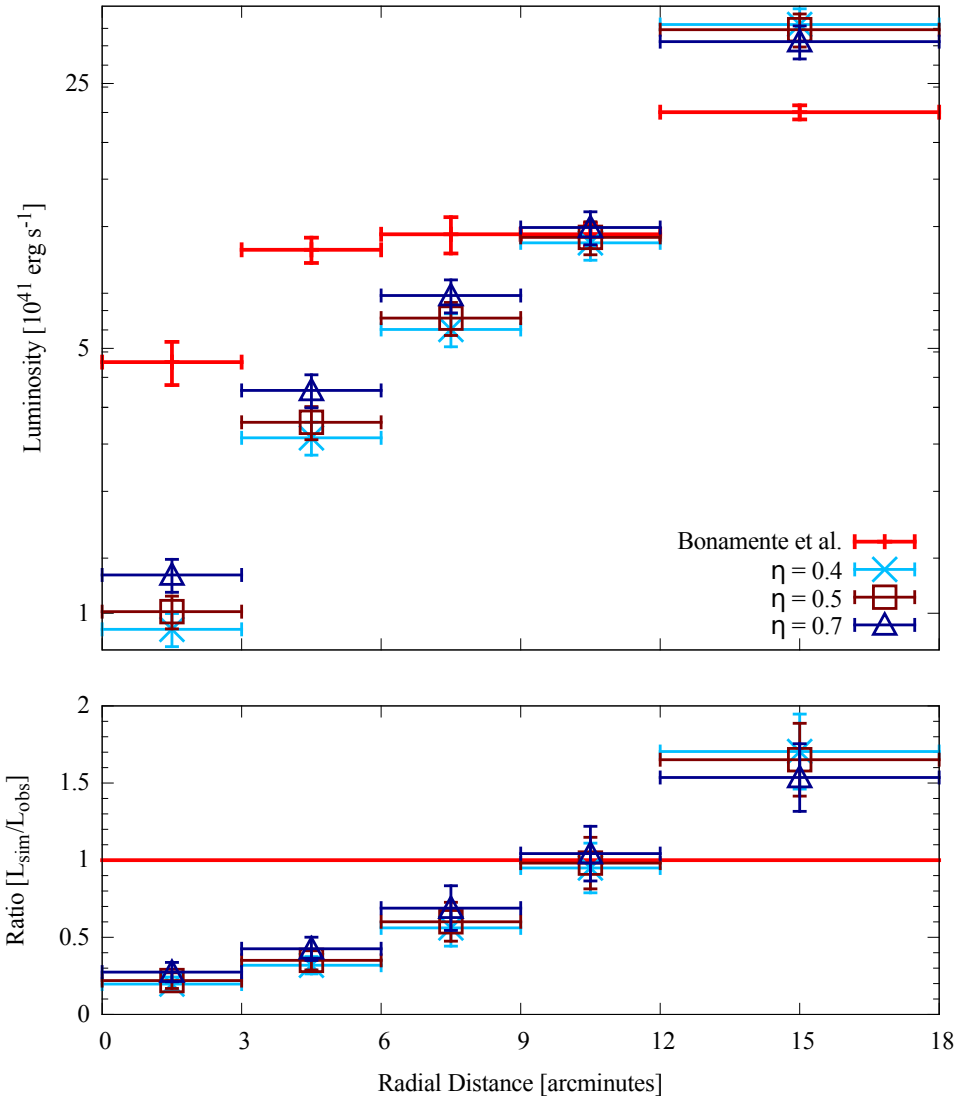

Figure 4.9: Luminosity comparison for Model 1 with different η values, compared to the data for a 'thermal' fit to the soft excess (note that the background from the hot ICM has been subtracted). For $\Delta N_{\rm eff} = 0.5$ and $\langle E_{\rm CAB} \rangle = 150\,{\rm eV}$, normalisation of the integrated luminosities gives $M = 6.1 \times 10^{12}$, 6.7×10^{12} and $6.5 \times 10^{12}\,{\rm GeV}$ for $\eta = 0.4$, 0.5 and 0.7, respectively.

scaling $\Delta N_{\rm eff} \to \lambda \Delta N_{\rm eff}$ and $M \to \sqrt{\lambda} M$.

From figure 4.9, we note that while the luminosity in each bin is within observations by a factor of a few, there is a clear tendency to underproduce photons in the centre and overproduce them in the outskirts. Axion-photon conversion in the Model 1 magnetic field therefore does not provide a particularly good description of the Coma soft excess.

The three variations of Model 1 in figure 4.9 correspond to the magnetic field model parameters that best fit the Faraday rotation measures, here denoted by $\eta = 0.5$ and its 1σ variations to $\eta = 0.4$ and $\eta = 0.7$. In all cases, axion-photon conversion under- and over-produces photons in the inner and outer regions, respectively. Understandably, increasing η so that the magnetic field falls off more rapidly with radius while simultaneously increasing B_0 to match Faraday rotation measures results in more luminosity to smaller radii relative to larger radii. We note that these variations are not large enough to make the CAB prediction of the morphology of the soft excess compatible with observations.

However, despite the poor fit of the axion-converted photon luminosities to the soft excess for Model 1, it would be premature to conclude that the conversion of the CAB cannot explain the soft excess. Even before considering systematic differences between the magnetic field models of [82] and the actual magnetic field in Coma, as discussed in section 4.3.2, Faraday rotation measures only constrain the magnetic field model up to degeneracies in the spectral index of the vector potential, n, and the Fourier mode cut-off scale $\Lambda_{\rm max}$. In Model 3, we consider a magnetic field model that provides an equally good fit to Faraday rotation measures as Model 1, but with $n = 4$ and $\Lambda_{\rm max} = 100\,{\rm kpc}$ (as opposed to $n = 17/3$ and $\Lambda_{max} = 34\,{\rm kpc}$ for Model 1). As in equation (4.26), the stochastically generated magnetic field prior to modulation by $n_e(r)$ has $\tilde{B}(k)_{\rm (gen.)} \sim k^{(-n+2)/2}$, so that for $n = 4$ the power integral $\int {\rm d}k k^2 \tilde{B}(k)^2_{\rm (gen.)}$ has constant support from $k_{\rm min}$ to $k_{\rm max}$. Equivalently, magnetic fields with $n > 4$ locate more power to smaller k-numbers and larger physical scales.

Therefore, a key difference between Model 1 and Model 3 is the distribution of effective coherence lengths. In order to highlight the effect of concentrating more power of the magnetic field on smaller scales, we first consider a toy magnetic field model, which does not provide a good fit to Faraday rotation measures.[4] This is our Model 2, to which we now turn.

[4]Note that the small scales in this model are however not necessarily unphysical. Faraday rotation constrains the magnitude and coherence lengths of the parallel component of the magnetic field along the line of sight, whereas axion conversion involves the transverse

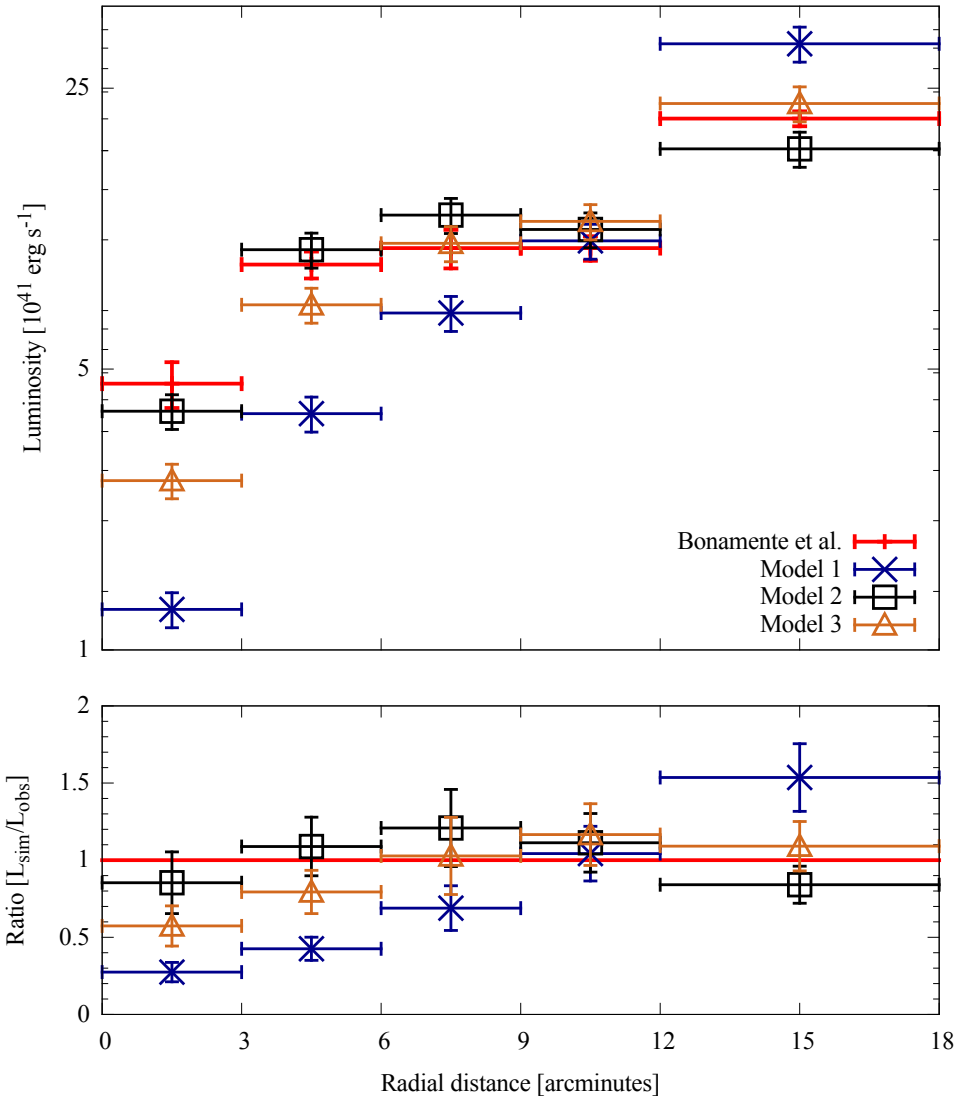

Figure 4.10: Luminosity comparison for the different models, compared to the data for a 'thermal' fit to the soft excess (note that the background from the hot ICM has been subtracted). For $\Delta N_{\rm eff} = 0.5$ and $\langle E_{\rm CAB} \rangle = 150\,{\rm eV}$, normalisation of the integrated luminosities gives $M = 6.5 \times 10^{12}$, 5.2×10^{12} and $5.7 \times 10^{12}\,{\rm GeV}$ for Models 1 ($\eta = 0.7$), 2, and 3, respectively.

Model 2: In this model the generated magnetic field, prior to modulation by a function of the electron density, only varies on scales between $2 - 5\,{\rm kpc}$. In this range the magnetic field varies with $n = 17/3$, and its modulation with electron density is obtained with $\eta = 0.7$ and $B_0 = 5.4\,\mu{\rm G}$. The simulated

components. The magnetic field models used here make these equal by assumption, but if the coherence length of the latter is actually smaller than that of the former by a factor of a few, this model could still be consistent with Faraday rotation.

photon luminosities from this model match the observational data for the soft excess very well, as is shown in figure 4.10.

Based on our earlier discussion on the radial dependence of the simulated conversion probabilities, we may interpret the improved fit as due to a decreased 'effective coherence length', resulting in modes approaching the small-Δ attractor at smaller radii, c.f. figures 4.7a and 4.7b.

Model 3: We now return to magnetic field models consistent with observations of Faraday rotation measures in Coma, but focus on models that concentrate more power on smaller scales relative to Model 1. The effective degeneracy between values of n and $\Lambda_{\rm max}$ allows n to be reduced provided $\Lambda_{\rm max}$ is increased simultaneously, as is illustrated in figure 16 of [82]. Once again, we take parameter values $\eta = 0.7$ and $B_0 = 5.4\,\mu$G. The resulting photon luminosities from CAB conversion are shown in figure 4.10 and again exhibit a good agreement with the observed soft excess.

The conclusion to draw from these results is that an explanation of the soft excess via axion-photon conversion appears to require the transverse components of the magnetic field to have more power on shorter scales than in the Kolmogorov spectra of [82]. This can be achieved either by allowing a flatter spectrum, so as to be consistent with Faraday rotation measures even for a Gaussian magnetic field, or by having different coherence lengths for transverse and parallel components of the magnetic field.

4.5.3 Constraints on the axion-photon coupling

Having established that the CAB explanation of the cluster soft excess is in reasonable agreement with observations for magnetic field models motivated by observations of Faraday rotation measures, we will now discuss how additional observational constraints give rise to a relatively limited range of possible values for M and the mean CAB energy, $\langle E_{\rm CAB}\rangle$.

Strong upper bounds on the axion-photon coupling — and thereby lower bounds on $M = g_{a\gamma\gamma}^{-1}$ — have been obtained by laboratory experiments, helioscopes, and may also be inferred from astrophysical arguments (see e.g. [106] for a recent review). For light axions, the CAST search for solar axions has set a bound $M > 10^{10}\,\mathrm{GeV}$. Proposed experiments looking either for light shining through a wall, such as ALPS-II [107], or for solar axions, such as IAXO [108], are expected to improve this bound by a factor of $10 - 15$. An astrophysical bound based on the anomalous energy losses of horizontal branch stars due to axion emission similarly gives $M > 10^{10}\,\mathrm{GeV}$ [109], with similar bounds also attainable from 'blue loop' Helium-burning massive stars [110]. Moreover, the absence of γ-ray bursts in coincidence with neutrinos from Supernova 1987A provides a bound of $M > 10^{11}\,\mathrm{GeV}$ for light axions ($m_a \lesssim 10^{-9}\,\mathrm{eV}$) [111, 112].

In addition to limits, certain values of the axion parameters have also been suggested to be hinted by anomalous astrophysical processes. Spectra from active galactic nuclei (AGN) in γ-rays extend to the multi-TeV regime, even though scattering off ambient starlight at these energies should provide attenuation through production of e^+e^- pairs. This apparent transparency of the Universe to γ-rays may possibly be explained by photons oscillating into axions relatively close to the AGN, followed by the axions traveling unimpeded through the Universe and subsequently converting back to photons in the galactic or intergalactic magnetic fields. Such a scenario is possible for $m_a \lesssim 10^{-9}\,\mathrm{eV}$ and $M \approx 10^{11} - 10^{12}\,\mathrm{GeV}$ [113–117].

Independently, there are observational hints for non-standard energy losses in white dwarfs, which may plausibly be explained by axions with $m_a <$ keV for certain values of the axion coupling to electrons [118–120]. It is reasonable to assume that the axion-photon coupling and the axion-electron coupling are suppressed by the same scale, but with an unknown and model-dependent relative coefficient. In concrete models this coefficient may range from 0.1 to 10^{-4} in favour of a stronger coupling to photons. Hence the white dwarf

hint may cautiously be interpreted as a hint for axions with $m_a <$ keV and $M \sim 10^{11} - 10^{13}\,\mathrm{GeV}$.

In the following we will consider the restrictions from the laboratory bound $M > 10^{10}\,\mathrm{GeV}$ together with the supernova γ-burst bound of $M > 10^{11}\,\mathrm{GeV}$. We will find that the CAB explanation for the soft excess is possible for light axions with $M \sim 10^{11} - 7 \times 10^{12}\,\mathrm{GeV}$, which is in the same range as suggested by the white dwarf energy loss hint and the γ-ray transparency hint.

Furthermore, while in our model axion-photon conversion in the Coma magnetic field should explain the soft X-ray excess, strong restrictions on the model parameters can be obtained by noting that higher energy photons should not be abundantly produced from axion-photon conversion: the excess is soft and does not survive to higher energies. This poses a restriction on the support of the CAB spectrum, as parametrised by the mean CAB energy. Here, we will impose that axion-photon conversion in the $0.5 - 0.6\,\mathrm{keV}$ band should not contribute to more than 10% of the thermal luminosity in this range. More accurate — and quite possibly more stringent — bounds may be obtained by detailed extraction of the soft excess based on dedicated templates for the CAB spectrum.

In figure 4.11 we show the values of M necessary to normalise the total CAB-converted luminosity to the observed soft excess, for a wide range of mean axion energies and for all three models of the magnetic field. In all cases we have considered $\Delta N_{\mathrm{eff}} = 0.5$, and for all models the parameters $\eta = 0.7$, $B_0 = 5.4\,\mu\mathrm{G}$ have been chosen.

The astrophysical and laboratory bounds on M may be translated into a lower bound on the mean CAB energy, and we find that, quite model-independently, this gives $\langle E_{\mathrm{CAB}} \rangle \gtrsim 45 - 50\,\mathrm{eV}$. Meanwhile, the bound from X-ray overproduction gives more model-dependent constraints but allows for $\langle E_{\mathrm{CAB}} \rangle \lesssim 250\,\mathrm{eV}$ for the interesting Model 3. We note that this restricts the values of λ in equation (4.18) to the range $2 \times 10^5 < \lambda < 10^6$. In sum, we can

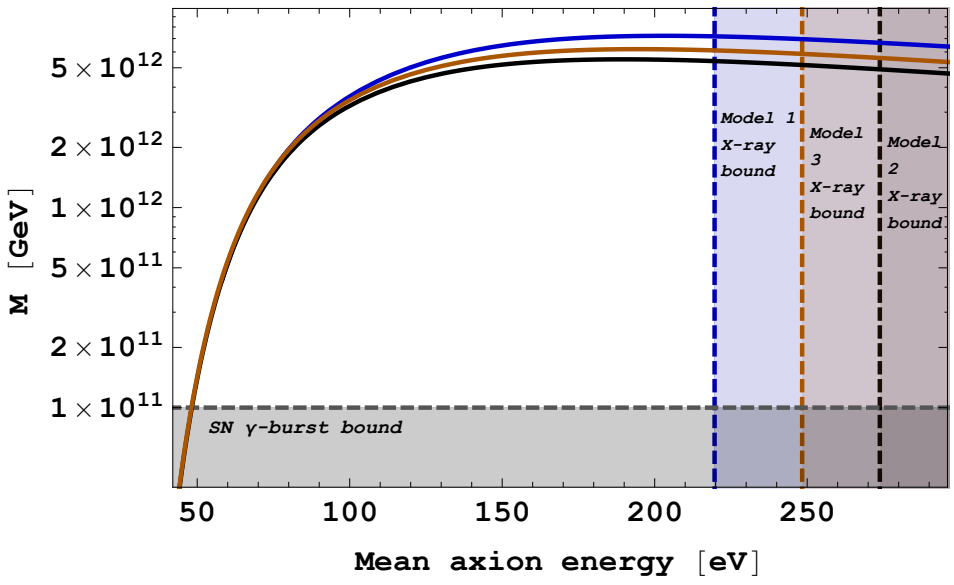

Figure 4.11: The values of M required to normalise the total soft excess from axion-photon conversion in the $0.2 - 0.4\,\mathrm{keV}$ band to the observed total excess luminosity with the central 18 arcminutes of Coma as a function of $\langle E_{\mathrm{CAB}} \rangle$, for $\Delta N_{\mathrm{eff}} = 0.5$. Model 1 is represented by the blue solid curve, Model 2 by the black curve and Model 3 by the orange curve. The supernova γ-burst bound is indicated by a dashed grey line, and the bounds from overproduction of X-rays in the $0.5 - 0.6\,\mathrm{keV}$ range are indicated by a vertical dashed line for each model.

express the interesting values for the scale M as

$$10^{11}\,\mathrm{GeV} \lesssim M \lesssim 7 \times 10^{12} \sqrt{\frac{\Delta N_{\mathrm{eff}}^{(a)}}{0.5}}\,\mathrm{GeV}\,. \tag{4.53}$$

Here we emphasise that $\Delta N_{\mathrm{eff}}^{(a)}$ denotes the extra relativistic contribution to the energy density from the axions responsible for the soft excess. If multiple species contribute to the dark radiation of the Universe, then clearly $\Delta N_{\mathrm{eff}}^{(a)} < \Delta N_{\mathrm{eff}}$.

Finally, let us comment on the spectral distribution of the soft excess photons, as predicted for axion-photon conversion of a CAB. Figure 4.12 shows the differential densities of the CAB as well as the photon spectrum arising after axion-photon conversion in the cluster magnetic field. Since low-energy axions have smaller conversion probabilities than high-energy axions, the resulting photon spectrum appears shifted to higher energies. For the particular case of $\langle E_{\mathrm{CAB}} \rangle = 150\,\mathrm{eV}$, the photon distribution has negligible support at $\omega < 21\,\mathrm{eV}$.

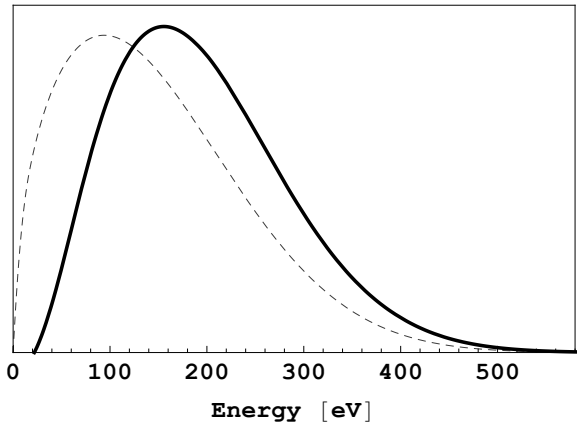

Figure 4.12: The shape of the soft X-ray spectrum from axion-photon conversion in galaxy clusters (solid line), together with the ambient CAB spectrum (dashed line) with $\langle E_{\rm CAB}\rangle = 150\,{\rm eV}$, as obtained from propagation through the Model 3 magnetic field. Both curves have been normalised independently.

In this case the functional form of the resulting photon distribution function is to a very good approximation given by

$$\frac{{\rm d}n_\gamma}{{\rm d}\omega} \sim \left(\frac{\omega - 21\,{\rm eV}}{150\,{\rm eV}}\right)^{1.21} \exp\left[-\left(\frac{\omega - 21\,{\rm eV}}{170\,{\rm eV}}\right)^{1.78}\right] \tag{4.54}$$

for $\omega \geq 21\,{\rm eV}$. The corresponding mean photon energy is $\langle E_\gamma\rangle \approx 200\,{\rm eV}$.

4.5.4 Summary of results

Let us conclude this section by summarising our results. We have found that the success of the CAB explanation for the morphology of the cluster soft excess depends on some of the details of the cluster magnetic field, and in particular on the distribution of the coherence lengths of the magnetic domains. The overall luminosity of the soft excess can easily be reproduced. However, the morphology obtained from axion-photon conversion is compatible with the observed soft excess for magnetic field models that predominantly have short (transverse) coherence lengths of a few kpc, as well as models that have uniformly distributed (transverse) coherence lengths from a few to 100 kpc. For Gaussian magnetic field models with transverse coherence lengths predominantly in

the 10 kpc range, such as our Model 1 above, the CAB explanation does not provide a close match to the observed soft excess morphology in Coma.

Interestingly, the range of axion-photon couplings required to explain the cluster soft excess (c.f equation (4.53)) is compatible with those suggested by the anomalously fast white dwarf cooling and with the anomalous transparency of the Universe in γ-rays.

4.6 Summary and outlook

In this chapter we have considered the possibility that axion-photon conversion of a string-theory-motivated Cosmic Axion Background with $0.1 - 1\,\mathrm{keV}$ energies may explain the long-standing soft X-ray excess in galaxy clusters.

We have focussed in detail on the well-studied Coma cluster, for which the soft excess has been established at high statistical significance and for which rather elaborate stochastic magnetic field models have been constructed, which have been shown to be consistent with observations of Faraday rotation measures. Using these magnetic field models, we have propagated axions through the cluster and studied the resulting morphology of soft X-ray photons.

This study has led us to three main conclusions. First, we have confirmed the assertion of [70] that the overall luminosity of the soft excess can easily be explained by axion-photon conversion. For example, a CAB with a mean energy of $\langle E_{\mathrm{CAB}} \rangle \approx 150\,\mathrm{eV}$ may explain the soft excess for an inverse axion-photon coupling of $M \sim \sqrt{\frac{\Delta N_{\mathrm{eff}}}{0.5}}\, 6 \times 10^{12}\,\mathrm{GeV}$.

Second, the CAB-induced soft excess exhibits a non-trivial morphology, which is sensitive to the distribution of coherence lengths of the transverse part of the cluster magnetic field. Within the class of Gaussian magnetic field models that are equally consistent with Faraday rotation measures [82, 99], those with a flat distribution in k-space were shown to reproduce well the observed soft excess morphology. On the contrary, for a magnetic field with a turbulent Kolmogorov spectrum (which locates power predominantly on larger,

$\mathcal{O}(10\,\mathrm{kpc})$, scales), the simulated excess flux disagrees with the observed morphology. The axionic explanation of the soft excess then requires either a flatter power spectrum or a shorter coherence length for the transverse component of the magnetic field (recall that Faraday rotation measures constrain only the magnetic field component parallel to the line of sight).

Third, the requirement that the cluster soft excess originates from a CAB strongly constrains the CAB properties. The absence of an X-ray excess at $E \gtrsim 0.5\,\mathrm{keV}$, combined with the astrophysical requirement that the axion-photon coupling satisfy $M \gtrsim 10^{11}\,\mathrm{GeV}$, constrains the mean CAB energy to the range

$$50\,\mathrm{eV} \lesssim \langle E_{\mathrm{CAB}} \rangle \lesssim 250\,\mathrm{eV}\ , \tag{4.55}$$

which in turn implies that the CAB explanation of the soft excess is viable only for

$$10^{11}\,\mathrm{GeV} \lesssim M \lesssim 7 \times 10^{12} \sqrt{\frac{\Delta N_{\mathrm{eff}}^{(a)}}{0.5}}\,\mathrm{GeV}\ . \tag{4.56}$$

The axion mass is similarly constrained to $m_a \lesssim 10^{-12}\,\mathrm{eV}$. Since the CAB spectral shape and the resulting soft X-ray spectrum are theoretically well-determined, the CAB hypothesis constitutes a sharp, well-defined, and predictive model that is subject to observational tests.

There are many further ways to extend this work and perform these tests. These include

- Studies of axion propagation through other clusters for which the magnetic field profile can be determined using Faraday rotation measures and soft excess properties have been determined. In this chapter we have determined the values of M and $\langle E_{\mathrm{CAB}} \rangle$ that are necessary to reproduce the Coma soft excess. We can apply these to other clusters in the sample of [75] to see whether, given the magnetic field model, these values of M and $\langle E_{\mathrm{CAB}} \rangle$ predict the correct magnitude for the soft excess.

- The magnetic field profile used here is by construction Gaussian and does not arise from a magnetohydrodynamical (MHD) simulation. It would be interesting to take magnetic field values found from a numerical MHD simulation of cluster formation and see whether there are any qualitative differences in the resulting axion-photon conversion probabilities, in particular in the behaviour of parallel and transverse coherence lengths.

- If a CAB exists, it continuously passes through our galaxy and converts to photons in the galactic magnetic field. It would be interesting to use models of the galactic magnetic field (for example those in [121, 122]) to determine the resulting number and distribution of soft X-ray photons, given the M and $\langle E_{\rm CAB}\rangle$ values required for the Coma cluster. This could then be compared with counts from the ROSAT 0.25 keV all-sky survey. Preliminary work in this direction has been performed in [87].

- The sample of [75] contains 38 clusters for which soft excess studies have been performed. If information can be obtained about the magnetic field and electron density in these clusters, it would be interesting to see whether this can be correlated with the presence or absence of a soft excess.

- Finally, we remark that it was shown recently in [123] that CAB conversion can also reproduce the soft excess observed in the outskirts of the Coma cluster for a similar parameter range. In particular, a model with a flat ($n = 4$) power spectrum gives values of M and $\langle E_{\rm CAB}\rangle$ that are consistent with the predictions for the central region, providing a further check of the CAB hypothesis.

The above studies will determine whether the CAB properties that can generate the soft excess in the Coma cluster remain consistent when applied to other observations.

Chapter 5

Conclusion

One of the central goals of String Phenomenology is to attempt to connect the elegant mathematical framework of String Theory to the real world. Throughout this Thesis we have seen how the possible existence of new types of relativistic matter in the Universe, known collectively as dark radiation, opens a broad avenue through which many string-inspired models can fall into the realms of testability. Constraints on the effective excess number of relativistic species, $\Delta N_{\rm eff}$, are already ruling out some models while placing stringent constraints on others. Furthermore, the bounds on $\Delta N_{\rm eff}$ are set to tighten dramatically within the next decade, so dark radiation will continue to improve as a very potent test of string-inspired scenarios.

I have focussed on a framework of string models known as the LARGE Volume Scenario, in which the compactified extra dimensions are naturally stabilised to be exponentially larger than the scale of string excitations. Some benefits of this setup are that the hierarchy associated with the large volume can bridge the gap between the Planck scale and the TeV-scale, and meanwhile the predictions for dark radiation are unambiguous and straightforward to calculate, since the post-inflationary history is determined uniquely by the decay modes of the lightest scalar modulus. In Chapter 2 I reviewed the production of dark radiation from decay of the lightest modulus — the volume modulus, corresponding to the size of the compactified extra-dimensional volume — into its axion partner. The corresponding decays to visible matter

proceed dominantly to MSSM Higgs bosons via a Giudice-Masiero interaction, whose coupling strength Z uniquely determines the yield of dark radiation. If we restrict the low-energy theory to MSSM matter content and choose $Z = 1$ at the string scale, which is true for models in which the Higgs sector is shift-symmetric, we find that the predicted dark radiation abundance is in tension with experiment.

I then considered the possible effect of quantum loop corrections as the value of Z runs from the string scale down to the scale of modulus decay at $\mathcal{O}(10^6\,\mathrm{GeV})$. However, the effect turned out to be negligible: the running due to gauge boson interactions, which enhances the branching fraction to the visible sector and pushes down the yield of dark radiation to within the observed limits, is effectively cancelled by a suppression due to top-quark loops. This effect was verified to two-loop level, and when constraints from the measured value of the Higgs boson mass were imposed, a lower bound of ΔN_{eff} was established for the Minimal LARGE Volume Scenario ($Z = 1$ at the string scale and pure-MSSM matter content in a sequestered visible sector). As experiments have been suggesting that $\Delta N_{\mathrm{eff}} \simeq 0.5$, this model is effectively ruled out — consistency with experiment requires either a larger coupling Z or the presence of additional vector-like matter (such as an extended Higgs sector).

Given this tension with experiment, in Chapter 3 I proceeded to study an extension of the LARGE Volume Scenario in which the compactification is endowed with a fibration structure. In such models the compactified volume is controlled by two moduli instead of one, and in particular the volume modulus is no longer the lightest modulus, this honour now falling upon the transverse modulus corresponding to the fibre directions in compact space. The predictions for dark radiation in this scenario are thus qualitatively different from the minimal setup; however, upon invoking sequestering of soft masses it was found that there is no longer any tree-level decay to the visible sector, giving a vast excess of dark radiation well beyond experimental bounds. In the remainder of the chapter I turned to the anisotropic limit of fibred compactifications,

in which two of the compact dimensions are stabilised much larger than the other four. Notably, this allows the visible sector to be realised on D7 branes wrapping the fibre cycle. It was found that in such a setup, string excitations within the D7 worldvolume are hierarchically lighter than transverse excitations, giving a non-standard pattern of soft terms. Furthermore, it was shown in [57] that this scenario produces less dark radiation overall than the MLVS, since decays to gauge bosons become a dominant process.

Finally, in Chapter 4 I presented an exploration of the scenario in which axionic dark radiation, redshifting to the present day to form a $\sim 0.2\,\mathrm{keV}$ Cosmic Axion Background, can convert into photons in astrophysical magnetic fields. The conversion is enhanced if the axions propagate through magnetic fields that are coherent over large distances: upon travelling through a huge structure such as a galaxy cluster, which contains magnetic fields that are coherent over kiloparsec scales, axion conversion into photons can produce an observable flux. Meanwhile, it is known that galaxy clusters emit an excess flux of low-energy ($0.1 - 1\,\mathrm{keV}$) X-rays above what is expected purely from thermal bremsstrahlung, and furthermore this soft excess is present far from the cluster core, a feature that is not well explained by the leading astrophysical explanations for the excess.

We studied the morphology of the soft excess for the Coma cluster by numerically simulating axion-photon conversion in the Coma magnetic field, using magnetic field models that are consistent with Faraday rotation measures. We found that the shape of the soft excess can be reproduced provided the magnetic field has more power concentrated on smaller scales than expected from Faraday rotation, which can be achieved via either a flatter power spectrum or from the magnetic field having different correlation lengths parallel and transverse to our line of sight. Finally, through constraints from supernova γ-ray bursts and the absence of a soft excess above $0.5\,\mathrm{keV}$, we were able to constrain the required inverse axion-photon coupling and the mean CAB energy to $10^{11}\,\mathrm{GeV} \lesssim M \lesssim 7\times10^{12}\,\mathrm{GeV}$ and $50\,\mathrm{eV} \lesssim \langle E_{\mathrm{CAB}}\rangle \lesssim 250\,\mathrm{GeV}$, respectively.

There are several directions in which to continue the work presented in this Thesis. First of all, we should explore other string-inspired models of the early Universe and investigate how much dark radiation they produce. If the BICEP2 result holds up, it would be interesting to see if these models can accommodate both the dark radiation bounds and a tensor-to-scalar ratio of $r \simeq 0.2$. Additionally, a 3.5 keV X-ray line has recently been observed in many galaxy clusters [124] as well as the Andromeda galaxy [125]. This line appears to be inconsistent with all known atomic transitions, so a possible explanation is that it constitutes a signal of dark matter decaying to photons. An alternative explanation, explored in [126–128], is that the dark matter decays to axion-like particles, which then oscillate into photons in the galactic/cluster magnetic field. This provides a further probe of CAB scenarios and a new window into physics beyond the Standard Models of Particle Physics and Cosmology.

These lines of research inject fresh ideas and perspectives into both the String Phenomenology and Cosmology communities, as well as providing new candidate explanations for a selection of mysterious astrophysical phenomena. Furthermore, continual progress in testing string models will help to move String Theory further beyond accusations of untestability and closer to the regime of empirical science. Overall, it would be fair to say that the future is bright for String Cosmology. However, with the experimental bounds on dark radiation tightening rapidly, it is equally fair to say that for many string-inspired models of the early Universe, the future is dark.

Appendix A

The anomalous dimension of Z

In this Appendix we present our calculation of the one-loop contribution to the anomalous dimension of the Giudice-Masiero coupling Z (equation (2.27)). First we compute the corrections to the vertex in section A.1, then we calculate corrections to the Higgs propagators in section 4.4.2. Finally in section A.3 we bring it all together and derive the one-loop Renormalisation Group flow equation for γ_Z.

A.1 Renormalisation of the vertex

Our first task is to compute the 1-loop correction to the vertex that corresponds to the modulus decay channel $\Phi \to H_{\rm u} H_{\rm d}$.

A.1.1 Contribution from the Higgs loop

To begin, let us consider the contribution to the modulus-Higgs-Higgs vertex from the process shown in figure A.1. The D-term potential for the Higgs fields is [37]

$$V_{D,\text{Higgs}} = \frac{(g^2+g'^2)}{8}\left(H_{\rm u}^\dagger H_{\rm u} - H_{\rm d}^\dagger H_{\rm d}\right)^2 + \frac{g^2}{2}|H_{\rm u}^\dagger H_{\rm d}|^2 \,, \tag{A.1}$$

which gives an interaction Lagrangian

$$\mathcal{L} = \frac{(g^2+g'^2)}{4}\left(H_{\rm u}^\dagger H_{\rm u}\right)\left(H_{\rm d}^\dagger H_{\rm d}\right) - \frac{g^2}{2}\left(H_{\rm u}^\dagger H_{\rm d}\right)\left(H_{\rm d}^\dagger H_{\rm u}\right) \,. \tag{A.2}$$

From this it can easily be seen that the associated tree-level vertex factor is

$$i(V_{H_{\rm u}^2 H_{\rm d}^2})^{ij}_{kl} = i\left[\frac{(g^2+g'^2)}{4}\delta^i{}_k\delta^j{}_l - \frac{g^2}{2}\delta^i{}_l\delta^j{}_k\right] \,. \tag{A.3}$$

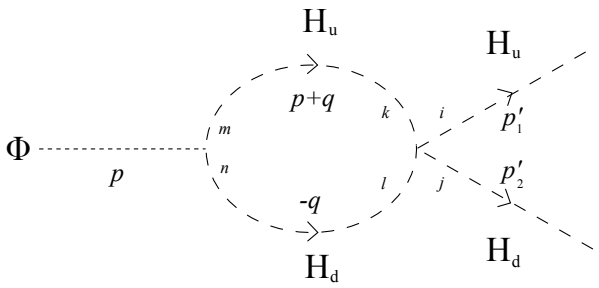

Figure A.1: 1-loop vertex diagram with quartic $H_{\rm u}^2 H_{\rm d}^2$ interaction.

The tree-level Higgs propagators are

$$(\Delta_{\rm u})^i{}_j(p) = (\Delta_{\rm d})^i{}_j(p) = \frac{\delta^i{}_j}{p^2 + m^2 - i\epsilon} \,, \tag{A.4}$$

where m is an infrared regulator, which we will set to zero at the end of the calculation. Finally, the tree-level vertex for decay of the modulus into $H_{\rm u}$ and $H_{\rm d}$ is

$$V^{ij}_{\Phi H_{\rm u} H_{\rm d}} = \epsilon^{ij} \frac{Z(-p^2)}{\sqrt{6} M_{\rm P}} \,. \tag{A.5}$$

By combining these ingredients and integrating around the loop, we find that the one-loop contribution to the vertex from the diagram of figure A.1 is

$$\begin{aligned} i\mathbf{V}^{ij}_{H^4\text{-loop}} &= \int \frac{\mathrm{d}^4 q}{(2\pi)^4} \Big(- i\Delta_{\rm u}(p+q) \Big)^k{}_m \Big(iV_{H_{\rm u}^2 H_{\rm d}^2} \Big)^{ij}_{kl} \Big(- i\Delta_{\rm d}(-q) \Big)^l{}_n \Big(iV_{\Phi H_{\rm u} H_{\rm d}} \Big)^{mn} \\ &= \epsilon^{ij} \frac{Z(-p^2)}{\sqrt{6} M_{\rm P}} \frac{(3g^2 + g'^2)}{4} \int \frac{\mathrm{d}^4 q}{(2\pi)^4} \frac{1}{\big[(p+q)^2 + m^2 - i\epsilon\big] \big[q^2 + m^2 - i\epsilon\big]} \,. \end{aligned} \tag{A.6}$$

The integrand can be rewritten using Feynman's formula,

$$\frac{1}{A_1 \dots A_n} = \int \mathrm{d}F_n \, \left(x_1 A_1 + \dots x_n A_n \right)^{-n} \,, \tag{A.7}$$

where

$$\int \mathrm{d}F_n \equiv (n-1)! \int_0^1 \mathrm{d}x_1 \dots \mathrm{d}x_n \, \delta(x_1 + \dots + x_n - 1) \,. \tag{A.8}$$

Applying this formula with $n = 2$ gives[1]

$$\frac{1}{\big[(p+q)^2 + m^2\big] \big[q^2 + m^2\big]} = \int_0^1 \mathrm{d}x \frac{1}{\big[q'^2 + D\big]^2} \,, \tag{A.9}$$

[1]We omit the $i\epsilon$ piece from now on, since it can be safely ignored after Wick-rotating the integral to Euclidean space via $q^0 \equiv i\bar{q}^0$, and also to avoid confusion with the dimensional regulator, commonly denoted by ϵ.

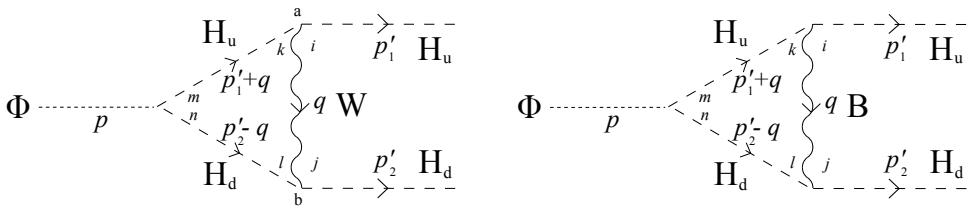

Figure A.2: 1-loop vertex diagrams with W-exchange (left) and B-exchange (right).

where $q' \equiv q + xp$ and $D \equiv x(1-x)p^2 + m^2$.

The integral can be evaluated by performing a Wick rotation and analytically continuing into d dimensions. We find that

$$\int \frac{\mathrm{d}^d q'}{(2\pi)^d} \frac{1}{\left[q'^2 + D\right]^2} = \frac{i}{16\pi^2} \left(\frac{4\pi}{D}\right)^{\epsilon/2} \Gamma\left(\frac{\epsilon}{2}\right) , \tag{A.10}$$

where $d = 4 - \epsilon$. Using $\Gamma(\epsilon/2) = 2/\epsilon + \mathcal{O}(\epsilon^0)$ and $A^{\epsilon/2} = 1 + \mathcal{O}(\epsilon)$, the overall contribution turns out to be

$$\mathbf{V}^{ij}_{H^4\text{-loop}} = \epsilon^{ij} \frac{Z(-p^2)}{\sqrt{6} M_{\mathrm{P}}} \frac{(3g^2 + g'^2)}{4} \lim_{\epsilon \to 0} \left\{ \frac{1}{8\pi^2 \epsilon} + \text{finite} \right\} . \tag{A.11}$$

A.1.2 Contributions from gauge boson exchange

The other main contributions come from the diagrams shown in figure A.2. The new ingredients required are: the tree-level gauge boson propagators,

$$\Delta^{ab}_{\mu\nu,W}(k) = \frac{\delta^{ab} P_{\mu\nu}}{k^2 + m^2 - i\epsilon} , \quad \Delta_{\mu\nu,B}(k) = \frac{P_{\mu\nu}}{k^2 + m^2 - i\epsilon} , \tag{A.12}$$

where in R_ξ gauge

$$P_{\mu\nu} = g_{\mu\nu} - (1 - \xi) \frac{k_\mu k_\nu}{k^2} ; \tag{A.13}$$

and the tree-level HHW/HHB vertex factors,

$$i(V^{\mu a}_{WH^2})^i{}_j(k, k') = i\frac{g}{2}(k + k')^\mu (\tau^a)^i{}_j , \quad i(V^{\mu}_{BH^2})^i{}_j(k, k') = i\frac{g'}{2}(k + k')^\mu Y \delta^i{}_j , \tag{A.14}$$

where k and k' are the momenta of the incoming and outgoing Higgs states respectively.

The W-exchange diagram gives a correction to the modulus decay of the form

$$
\begin{aligned}
i\mathbf{V}^{ij}_{HHW\text{-loop}} = \int \frac{\mathrm{d}^4 q}{(2\pi)^4} \Big[\Big(-i\Delta^{ab}_{\mu\nu,W}(q) \Big) \Big(iV^{\mu a}_{WH^2}(p_1+q,p_1) \Big)^i_k \Big(-i\Delta_{\mathrm{u}}(p_1+q) \Big)^k_m \\
\Big(iV_{\Phi H_{\mathrm{u}} H_{\mathrm{d}}} \Big)^{mn} \Big(-i\Delta_{\mathrm{d}}(q-p_2) \Big)^l_n \Big(iV^{\nu b}_{WH^2}(p_2-q,p_2) \Big)^j_l \Big] \\
= -\epsilon^{ij} \frac{Z(-p^2)}{\sqrt{6} M_{\mathrm{P}}} \frac{3g^2}{4} I_{\text{gauge loop}} \,, \qquad \text{(A.15)}
\end{aligned}
$$

where we have used the fact that $(\tau^a)^i{}_k \epsilon^{kl} (\tau^{a*})_l{}^j = -(\tau^a)^i{}_k (\tau^a)^k{}_l \epsilon^{lj} = -3\epsilon^{ij}$ for SU(2).[2]

The integral is given by

$$
I_{\text{gauge loop}} = I^{\mathrm{F}}_{\text{gauge loop}} - (1-\xi) I^{\xi}_{\text{gauge loop}} \,, \qquad \text{(A.16)}
$$

where $I^{\mathrm{F}}_{\text{gauge loop}}$ is the result for $\xi = 1$ (corresponding to Feynman gauge) and the gauge-dependent piece is included in $I^{\xi}_{\text{gauge loop}}$. Explicitly, one finds that

$$
\begin{aligned}
I^{\mathrm{F}}_{\text{gauge loop}} &\equiv \int \frac{\mathrm{d}^4 q}{(2\pi)^4} \frac{g_{\mu\nu}(2p_1+q)^\mu (2p_2-q)^\nu}{\big((p_1+q)^2+m^2\big)\big((p_2-q)^2+m^2\big)\big(q^2+m^2\big)} \\
&= \int \mathrm{d}F_3 \int \frac{\mathrm{d}^4 q'}{(2\pi)^4} \frac{N}{\big[q'^2 + D_3\big]^3} \,, \qquad \text{(A.17)}
\end{aligned}
$$

where

$$
q' = q + x_1 p_1 - x_2 p_2 \,, \qquad \text{(A.18)}
$$

$$
D_3 = x_1(1-x_1)p_1^2 + x_2(1-x_2)p_2^2 + 2x_1 x_2 p_1 \cdot p_2 + m^2 \,, \qquad \text{(A.19)}
$$

$$
N = -g_{\mu\nu}(q' + (2-x_1)p_1 + x_2 p_2)^\mu (q' - x_1 p_1 - (2-x_2)p_2)^\nu \,. \qquad \text{(A.20)}
$$

By Lorentz symmetry, the terms in N that are linear in q' will integrate to zero. Furthermore, the divergent piece comes from the q'^2 term in the numerator: using dimensional regularisation we find that

$$
I^{\mathrm{F}}_{\text{gauge loop}} = \lim_{\epsilon \to 0} \left\{ \frac{-i}{8\pi^2 \epsilon} + \text{finite} \right\} . \qquad \text{(A.21)}
$$

[2]Here we have employed the convention $\tau^a_{ij} = \frac{1}{2} T^a_{ij}$, where T^a_{ij} are the generators of SU(2).

A similar calculation follows for $I^{\xi}_{\text{gauge loop}}$. Introducing an additional infrared regulator so $q^2 \to q^2 + m^2$ for all such terms in the denominator, we find that

$$\begin{aligned} I^{\xi}_{\text{gauge loop}} &\equiv \int \frac{\mathrm{d}^4 q}{(2\pi)^4} \frac{q_\mu (2p_1 + q)^\mu q_\nu (2p_2 - q)^\nu}{\big(q^2 + m^2\big)\big((p_1 + q)^2 + m^2\big)\big((p_2 - q)^2 + m^2\big)\big(q^2 + m^2\big)} \\ &= \int \mathrm{d}F_4 \int \frac{\mathrm{d}^4 q'}{(2\pi)^4} \frac{N'}{\big[q'^2 + D_3\big]^4} \,, \end{aligned} \tag{A.22}$$

where

$$N' = -(q'^2)^2 + \dots \,. \tag{A.23}$$

The divergent contribution yields

$$I^{\xi}_{\text{gauge loop}} = \lim_{\epsilon \to 0} \left\{ \frac{-i}{8\pi^2 \epsilon} + \text{finite} \right\} = I^{\text{F}}_{\text{gauge loop}} + \text{finite} \,, \tag{A.24}$$

so the overall contribution to the vertex is

$$\mathbf{V}^{ij}_{HHW\text{-loop}} = \epsilon^{ij} \frac{Z(-p^2)}{\sqrt{6} M_{\text{P}}} \frac{3g^2}{4} \lim_{\epsilon \to 0} \left\{ \frac{1}{8\pi^2 \epsilon} + \text{finite} \right\} \xi \,. \tag{A.25}$$

An analogous calculation follows for the U(1) boson exchange loop (figure A.2, right). We find that

$$i\mathbf{V}^{ij}_{HHB\text{-loop}} = -\epsilon^{ij} \frac{Z(-p^2)}{\sqrt{6} M_{\text{P}}} \frac{g'^2}{4} I_{\text{gauge loop}} \,. \tag{A.26}$$

Therefore,

$$\mathbf{V}^{ij}_{HHB\text{-loop}} = \epsilon^{ij} \frac{Z(-p^2)}{\sqrt{6} M_{\text{P}}} \frac{g'^2}{4} \lim_{\epsilon \to 0} \left\{ \frac{1}{8\pi^2 \epsilon} + \text{finite} \right\} \xi \,. \tag{A.27}$$

A.1.3 One-loop result

The total one-loop correction to the $\Phi \to H_{\text{u}} H_{\text{d}}$ vertex is given by

$$\mathbf{V}^{ij}_{\Phi H_{\text{u}} H_{\text{d}}}\Big|_{1 \text{ loop}} = \mathbf{V}^{ij}_{H^4\text{-loop}} + \mathbf{V}^{ij}_{HHW\text{-loop}} + \mathbf{V}^{ij}_{HHB\text{-loop}} \,. \tag{A.28}$$

Summing up (A.11), (A.25) and (A.27) gives

$$\mathbf{V}^{ij}_{\Phi H_{\text{u}} H_{\text{d}}}\Big|_{1 \text{ loop}} = \epsilon^{ij} \frac{Z(-p^2)}{\sqrt{6} M_{\text{P}}} \lim_{\epsilon \to 0} \left\{ \frac{1}{8\pi^2 \epsilon} + \text{finite} \right\} \frac{(3g^2 + g'^2)}{4} \big(1 + \xi\big) \,. \tag{A.29}$$

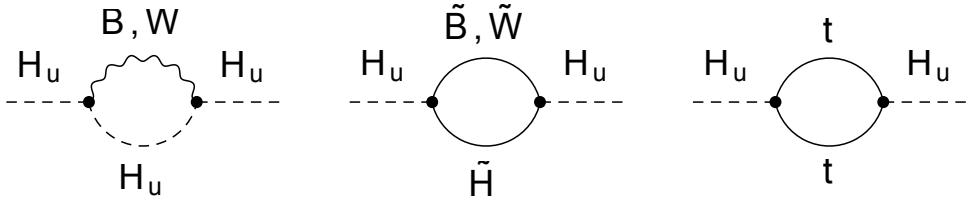

Figure A.3: The $H_u H_u$ self-energy diagrams needed to determine the wave-function renormalisation factor of H_u. Analogous diagrams exist for H_d, with the t-quark loop contribution replaced by b and τ loops.

We can account for the divergence by renormalising the vertex such that

$$\mathbf{V}^{ij}_{\Phi H_{\rm u} H_{\rm d}} \to \mathcal{Z}_Z \mathbf{V}^{ij}_{\Phi H_{\rm u} H_{\rm d}} \,, \tag{A.30}$$

where

$$\mathcal{Z}_Z = 1 + \lim_{\epsilon \to 0} \left\{ \frac{1}{8\pi^2 \epsilon} \right\} \left[- \frac{(3g^2 + g'^2)}{4} \big(1 + \xi\big) \right] + \mathcal{O}\big(g^4, g'^4, g^2 g'^2\big) \tag{A.31}$$

in the $\overline{\rm DR}$ scheme.

A.2 Anomalous dimensions of the Higgs propagators

In order to compute the observed running of the vertex we also need to consider wavefunction renormalisation of the Higgs fields. In practice, this corresponds to computing their anomalous dimensions. There are three types of diagram that contribute to Higgs field renormalisation, as illustrated for H_u in the top row of figure A.3. We evaluate each in turn.

A.2.1 Gauge boson contribution

The first relevant diagram involves the emission and absorption of a gauge boson (see figure A.3, left), which can be either a W ($\mathrm{SU}(2)_L$) or B ($\mathrm{U}(1)_Y$) boson. We define the exact Higgs propagator to be

$$\mathbf{\Delta}^i{}_j(p^2) = \frac{\delta^i{}_j}{p^2 + m^2 - i\epsilon - \Pi(p^2, m^2)} \,, \tag{A.32}$$

where $\Pi(p^2, m^2)$ is given (to one-loop order) by all the one-particle irreducible (1PI) one-loop diagrams contributing to the propagator. The mass m^2 is an infrared regulator: ultimately we only care about the contribution to Π that is proportional to $-p^2$, as this corresponds to wavefunction renormalisation, and since we are well above the soft mass scale we can simply take $m^2 \to 0$ at the end of the calculation without worrying about the details of low-energy physics.

The total correction from emission and absorption of W and B bosons is

$$\begin{aligned} & i\Pi_{\text{gauge}}\delta^i{}_j \\ &= \int \frac{\mathrm{d}^4 q}{(2\pi)^4}\Bigg[\frac{ig}{2}(2p+q)_\mu(\tau^b)^i{}_l\frac{-i\delta^l{}_k}{(p+q)^2+m^2-i\epsilon}\frac{ig}{2}(2p+q)_\nu(\tau^a)^k{}_j\frac{-i\delta^{ab}P^{\mu\nu}}{q^2+m^2-i\epsilon} \\ &\qquad +\frac{ig'Y}{2}(2p+q)_\mu\delta^i{}_l\frac{-i\delta^l{}_k}{(p+q)^2+m^2-i\epsilon}\frac{ig'Y}{2}(2p+q)_\nu\delta^k{}_j\frac{-iP^{\mu\nu}}{q^2+m^2-i\epsilon}\Bigg], \end{aligned} \tag{A.33}$$

where Y is the hypercharge of the Higgs doublet in question (in our normalisation $Y_{H_\mathrm{u}} = 1$ and $Y_{H_\mathrm{d}} = -1$). Since the hypercharge is squared in the second term, the contributions to the exact propagators of H_u and H_d are identical.

Simplifying (and omitting $i\epsilon$ in the denominator to avoid confusion) leads to a result of the form

$$i\Pi_{\text{gauge}} = \frac{i(3g^2+g'^2)}{4}\left[\int_0^1 \mathrm{d}x\, I^{\mathrm{F}}_{\text{loop}} - (1-\xi)\int \mathrm{d}F_3\, I^{\xi}_{\text{loop}}\right]. \tag{A.34}$$

Some key steps in the calculation are: $q' = q + xp$ (or equivalently $q' = q - x_3 p$ in the second integral); $D(x) = x(1-x)p^2 + m^2$; the fact that in the numerator $(p\cdot q')^2 \to \frac{1}{4}p^2 q'^2$ (in $d = 4$) while terms linear in q' vanish when integrated over $\mathrm{d}^4 q'$; and that $q'^0 \equiv i\bar{q}^0$ under a Wick rotation.

The loop integrals can again be evaluated using dimensional regularisation:

setting $d = 4 - \epsilon$ we find

$$\begin{aligned} I^{\mathrm{F}}_{\mathrm{loop}} &\equiv \int \frac{\mathrm{d}^d\bar{q}}{(2\pi)^d} \frac{(\bar{q}^2 + (2-x)^2 p^2)\tilde{\mu}^\epsilon}{\left[\bar{q}^2 + D(x)\right]^2} \\ &= \frac{1}{16\pi^2}\left[\frac{\Gamma\left(-1+\frac{\epsilon}{2}\right)\Gamma\left(3-\frac{\epsilon}{2}\right)}{\Gamma(2)\Gamma\left(2-\frac{\epsilon}{2}\right)} D(x) + \frac{\Gamma\left(\frac{\epsilon}{2}\right)}{\Gamma(2)}(2-x)^2 p^2\right]\left(\frac{4\pi\tilde{\mu}^2}{D(x)}\right)^{\epsilon/2} \\ &= \frac{1}{16\pi^2}\left[(3x^2 - 6x + 4)p^2 - 2m^2\right]\frac{2}{\epsilon} + \mathcal{O}(\epsilon^0)\ . \end{aligned} \tag{A.35}$$

which after integrating over $\mathrm{d}x$ yields

$$\int_0^1 \mathrm{d}x\, I^{\mathrm{F}}_{\mathrm{loop}} = \frac{1}{8\pi^2\epsilon}\left(2p^2 - 2m^2\right) + \mathcal{O}(\epsilon^0)\ . \tag{A.36}$$

Similarly for the second term,

$$\begin{aligned} I^{\xi}_{\mathrm{loop}} &\equiv \int \frac{\mathrm{d}^d\bar{q}}{(2\pi)^d} \frac{\left[(\bar{q}^2)^2 + \left(\frac{4}{d}(1-x_3)^2 - 2x_3(2-x_3)\right)p^2\bar{q}^2 + \mathcal{O}(\bar{q}^0)\right]\tilde{\mu}^\epsilon}{\left[\bar{q}^2 + D(x_3)\right]^3} \\ &= \frac{1}{16\pi^2}\left[\left(1 - 6x_3 + 6x_3^2\right)p^2 - 3m^2\right]\frac{2}{\epsilon} + \mathcal{O}(\epsilon^0)\ . \end{aligned} \tag{A.37}$$

Recalling (A.8) we can perform the integral over $\mathrm{d}F_3$ to get

$$\int \mathrm{d}F_3\, I^{\xi}_{\mathrm{loop}} = \frac{1}{8\pi^2\epsilon}\left(-p^2 - 3m^2\right) + \mathcal{O}(\epsilon^0)\ . \tag{A.38}$$

Plugging these results back into (A.34) and taking $m \to 0$ gives the result

$$\Pi_{\mathrm{gauge}} = -\frac{(3g^2 + g'^2)}{4}(3-\xi)\left(-p^2\right)\lim_{\epsilon\to 0}\left\{\frac{1}{8\pi^2\epsilon}\right\} + \text{finite}\ . \tag{A.39}$$

A.2.2 Gaugino-Higgsino contribution

The second contribution comes from the central diagram of figure A.3. First we need to work out the relevant vertex factors before we can combine them to evaluate the loop diagram.

Vertex factors

The $Hh\lambda_W$ and $Hh\lambda_B$ interactions come from the Kähler potential of the Higgs superfields,

$$K_H = \int \mathrm{d}^2\theta\mathrm{d}^2\bar{\theta}\ \Phi_H^\dagger \exp\left(g\tau^a V^a + g' Y V\right)\Phi_H\ , \tag{A.40}$$

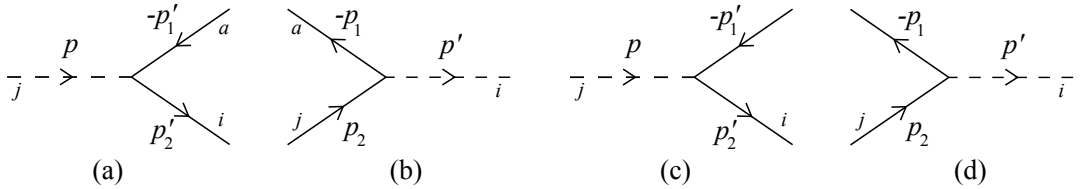

Figure A.4: Tree-level vertices: (a) $H \to h\lambda_W$; (b) $h\lambda_W \to H$; (c) $H \to h\lambda_B$; and (d) $h\lambda_B \to H$.

where the chiral Higgs superfield is

$$\Phi_H = H + \sqrt{2}\theta h + \theta\theta F_H - i\theta\sigma^\mu\bar{\theta}\partial_\mu H + \frac{i}{\sqrt{2}}\theta\theta\partial_\mu h\sigma^\mu\bar{\theta} - \frac{1}{4}\theta\theta\bar{\theta}\bar{\theta}\partial_\mu\partial^\mu H \quad \text{(A.41)}$$

and the vector gauge superfields are:

$$V^a = \theta\sigma^\mu\bar{\theta}W^a_\mu + \theta\theta\bar{\theta}\bar{\lambda}^a_W + \bar{\theta}\bar{\theta}\theta\lambda^a_W + \frac{1}{2}\theta\theta\bar{\theta}\bar{\theta}D^a \; ; \quad \text{(A.42)}$$

$$V = \theta\sigma^\mu\bar{\theta}B_\mu + \theta\theta\bar{\theta}\bar{\lambda}_B + \bar{\theta}\bar{\theta}\theta\lambda_B + \frac{1}{2}\theta\theta\bar{\theta}\bar{\theta}D \; . \quad \text{(A.43)}$$

Extracting the $\theta\theta\bar{\theta}\bar{\theta}$ terms proportional to $Hh\lambda$ and integrating, we find an interaction Lagrangian of the form

$$\mathcal{L} = \frac{1}{\sqrt{2}}\left[\left(gH^*_i(\tau^a)^i{}_j h^j\lambda^a_W + g'YH^*_i h^i\lambda_B\right) + \text{h.c.}\right] . \quad \text{(A.44)}$$

To work out vertex factors it is convenient to write the higgsino h as a component of a Dirac spinor and the gauginos $\lambda_{W,B}$ as Majorana spinors:

$$\Psi^i \equiv \begin{pmatrix} h^i \\ — \end{pmatrix} \; ; \quad \Lambda^a_W \equiv \begin{pmatrix} \lambda^a_W \\ \bar{\lambda}^a_W \end{pmatrix} \; ; \quad \Lambda_B \equiv \begin{pmatrix} \lambda_B \\ \bar{\lambda}_B \end{pmatrix} . \quad \text{(A.45)}$$

Then, making use of the identities

$$h^i = P_{\rm L}\Psi^i \; , \quad \text{(A.46)}$$

$$\bar{h}_i = \overline{P_{\rm L}\Psi_i} = \overline{\Psi}_i P_{\rm R} \; , \quad \text{(A.47)}$$

$$\overline{\Lambda} = \Lambda^{\rm T}\mathcal{C} \; , \quad \text{(A.48)}$$

where $P_{\rm L} = \frac{1}{2}(1-\gamma_5)$ and $P_{\rm R} = \frac{1}{2}(1+\gamma_5)$ are left- and right-projection matrices and $\mathcal{C}$ is the charge conjugation matrix, we find that the λh contractions can be re-expressed as

$$\lambda^a_W h^j = (\Lambda^a_W)^{\rm T}\mathcal{C}P_{\rm L}\Psi^j \quad , \quad \bar{h}_i\bar{\lambda}^a_W = \overline{\Psi}_i P_{\rm R}\Lambda^a_W \; ,$$
$$\lambda_B h^i = (\Lambda_B)^{\rm T}\mathcal{C}P_{\rm L}\Psi^i \quad , \quad \bar{h}_i\bar{\lambda}_B = \overline{\Psi}_i P_{\rm R}\Lambda_B \; . \quad \text{(A.49)}$$

Therefore the tree-level vertex factors (figure A.4) are given by

$$\Big(\text{Figure A.4(a)}\Big) = \frac{ig}{\sqrt{2}}(\tau^a)^i{}_j P_{\rm R} \quad , \quad \Big(\text{Figure A.4(b)}\Big) = \frac{ig}{\sqrt{2}}(\tau^a)^i{}_j \mathcal{C} P_{\rm L} \quad ,$$
$$\Big(\text{Figure A.4(c)}\Big) = \frac{ig'Y}{\sqrt{2}}\delta^i{}_j P_{\rm R} \quad , \qquad \Big(\text{Figure A.4(d)}\Big) = \frac{ig'Y}{\sqrt{2}}\delta^i{}_j \mathcal{C} P_{\rm L} \quad . \tag{A.50}$$

Evaluating the loop diagram

To evaluate the loop diagrams of figure we also need the fermion propagators,

$$S(p) = \frac{-\not{p} + m}{p^2 + m^2 - i\epsilon} \, . \tag{A.51}$$

In particular, the higgsino propagator is

$$(S_h)^i{}_j(p) = \delta^i{}_j S(p) \, , \tag{A.52}$$

while the gaugino propagators are

$$S^{ab}_{\lambda_W}(p) = \delta^{ab} S(p)\mathcal{C}^{-1} \, , \quad S_{\lambda_B}(p) = S(p)\mathcal{C}^{-1} \, . \tag{A.53}$$

We can now evaluate the correction to the Higgs propagator by integrating and taking the trace around the fermion loop.[3] This gives

$$i\Pi_{\rm ino}\delta^i{}_j = -\frac{(3g^2 + g'^2)}{2}\delta^i{}_j \int \frac{{\rm d}^4 q}{(2\pi)^4} {\rm Tr}\left[\frac{(-\not{p} - \not{q} + m)P_{\rm R}(-\not{q} + m)P_{\rm L}}{\big((p+q)^2 + m^2 - i\epsilon\big)\big(q^2 + m^2 - i\epsilon\big)}\right] . \tag{A.54}$$

We can simplify the trace over spinor indices by using the identities

$$\gamma_5^2 = 1 \, , \quad \big\{\gamma^\mu, \gamma_5\big\} = 0 \, , \quad {\rm Tr}\gamma_5 = 0 \, , \quad {\rm Tr}\big[\gamma_5\gamma^\mu\gamma^\nu\big] = 0 \, , \tag{A.55}$$

and the fact that

$${\rm Tr}\big[\gamma^{\mu_1} \ldots \gamma^{\mu_n}\big] = 0 \, , \quad {\rm Tr}\big[\gamma_5\gamma^{\mu_1} \ldots \gamma^{\mu_n}\big] = 0 \, , \tag{A.56}$$

for odd values of n. Applying these identities gives

$${\rm Tr}\Big[(-\not{p} - \not{q} + m)P_{\rm R}(-\not{q} + m)P_{\rm L}\Big] = \frac{1}{2}{\rm Tr}\Big[(\not{p} + \not{q})\not{q}\Big] = -2(p+q)\cdot q \, , \tag{A.57}$$

[3]Note that since we are dealing with spinor fields this induces an additional minus sign.

where in the second step we have made use of the additional identity

$$\mathrm{Tr}\big[\not{a}\not{b}\big] = -4(a\cdot b)\ . \tag{A.58}$$

We are now in a position to evaluate the loop integral. Again suppressing $i\epsilon$ terms for clarity, we find that

$$i\Pi_{\mathrm{ino}} = i(3g^2+g'^2)\int_0^1 \mathrm{d}x \int \frac{\mathrm{d}^4\bar{q}}{(2\pi)^4}\frac{(\bar{q}^2 - x(1-x)p^2)}{\big[\bar{q}^2+D\big]^2}\ , \tag{A.59}$$

where $q' \equiv q + xp$, $D \equiv x(1-x)p^2 + m^2$ and we have performed the usual Wick rotation. Continuing to $d = 4-\epsilon$ dimensions gives

$$\begin{aligned} I'_{\mathrm{loop}} &\equiv \int \frac{\mathrm{d}^d\bar{q}}{(2\pi)^d}\frac{(\bar{q}^2 - x(1-x)p^2)}{\big[\bar{q}^2+D\big]^2} \\ &= \frac{-1}{16\pi^2}\bigg[-3D+m^2\bigg]\frac{2}{\epsilon} + \mathcal{O}(\epsilon^0)\ . \end{aligned} \tag{A.60}$$

Finally, we can use the fact that $\int_0^1 \mathrm{d}x D = \frac{1}{6}p^2 + m^2$ and take $m \to 0$ to arrive at the result

$$\Pi_{\mathrm{ino}} = \frac{(3g^2+g'^2)}{4}\big(-2p^2\big)\lim_{\epsilon\to 0}\left\{\frac{1}{8\pi^2\epsilon}\right\} + \text{finite}\ . \tag{A.61}$$

A.2.3 Fermion contribution

The MSSM superpotential,

$$W = y_{u,IJ}H_u Q_L^I \bar{U}_R^J + y_{d,IJ}H_d Q_L^I \bar{D}_R^J + y_{l,IJ}H_d L_L^I \bar{E}_R^J\ , \tag{A.62}$$

gives rise to quartic scalar couplings, $y_{IJK}y^*_{IMN}\phi^J\phi^K\phi^{*M}\phi^{*N}$, as well as trilinear fermion-fermion-scalar Yukawa couplings, $y_{IJK}\phi^I\psi^J\psi^K + \text{h.c.}$. In what follows, we will assume that the third-generation Yukawa couplings give the dominant contributions to the Yukawa matrices, i.e. $y_{u,IJ} \approx \mathrm{diag}(0,0,y_t)$, $y_{d,IJ} \approx \mathrm{diag}(0,0,y_b)$ and $y_{l,IJ} \approx \mathrm{diag}(0,0,y_\tau)$.

The correction to the $H_{u,d}$ propagators from the left- and right-handed scalar loops is proportional to the scalar mass squared. Therefore, since we are taking all soft masses to zero (as the interactions we are considering take

place at $\mathcal{O}(10^6\,\mathrm{GeV}) \gg M_{\mathrm{soft}} \sim \mathcal{O}(\mathrm{TeV})$), the quartic scalar couplings do not contribute to wavefunction renormalisation. On the other hand, corrections to the $H_{u,d}$ wavefunctions do arise from quark loops. These are mediated by the trilinear Yukawa couplings: the fermion-fermion-Higgs Lagrangian for H_u is

$$\mathcal{L} \supset -y_t \epsilon_{ij} H_u^i q_L^j t_R^\dagger + \text{h.c.} \,, \tag{A.63}$$

where q_l is the doublet containing the left-handed components of the top and bottom quarks. Here we will focus on the H_u case — there are analogous interactions for H_d involving bottom quarks and τ leptons.

We use the following relations to rewrite this Lagrangian in terms of Dirac spinors:

$$\begin{aligned} \bar{\Psi} P_L \Psi &= \chi \xi \,; \\ \bar{\Psi} P_R \Psi &= \xi^\dagger \chi^\dagger \,. \end{aligned} \tag{A.64}$$

The Weyl top-quark kinetic terms then combine into a Dirac term,

$$i\partial_\mu t_L^\dagger \bar{\sigma}^\mu t_L + i\partial_\mu t_R \bar{\sigma}^\mu t_R^\dagger = i\bar{\Psi}_t \gamma^\mu \partial_\mu \Psi_t \,. \tag{A.65}$$

The interaction term becomes

$$\mathcal{L} \supset -y_t \epsilon_{ij} H_u^i \bar{\Psi}_t P_L \Psi_q^j - y_t^* \epsilon_{ij} H_u^{i*} \bar{\Psi}_q^j P_R \Psi_t \,, \tag{A.66}$$

from which we can read off vertex factors

$$(V_{Ht\bar{t}})_{ij} = -y_t P_L \epsilon_{ij} \,, \quad (V_{H^*\bar{t}t})_{ij} = -y_t^* P_R \epsilon_{ij} \,. \tag{A.67}$$

Finally, the fermion propagator is given by

$$\left(S^{ab}(p)\right)^{i}_{\ j,\ \alpha\beta} = \left(\frac{-\not{p} + m}{p^2 + m^2 - i\epsilon}\right)_{\alpha\beta} \delta^{ab} \delta^i{}_j \,, \tag{A.68}$$

where a and b are colour indices.

Putting all this together, we can evaluate the relevant one-loop diagram (figure A.3, right),

$$\begin{aligned} &i\Pi^{H_u}_{\mathrm{fermion}} \delta^i{}_j \\ &= -3 \int \frac{\mathrm{d}^4 q}{(2\pi)^4} \mathrm{Tr} \left[\frac{-i(-\not{q} + m)}{q^2 + m^2 - i\epsilon} (-iy_t P_L \epsilon_{jl}) \frac{-i(-\not{p} - \not{q} + m)}{(p+q)^2 + m^2 - i\epsilon} (-iy_t^* P_R \epsilon^{li}) \right] \,, \end{aligned} \tag{A.69}$$

where m is the usual infrared regulator. Here the trace is over spinor indices, and the trace over colour indices has been evaluated to give a factor of 3. If we change variables to $l = k + xp$, define $D = x(1-x)p^2 + m^2$ and use $\epsilon_{jl}\epsilon^{li} = \delta^i{}_j$, we find

$$i\Pi^{H_u}_{\text{fermion}} = 6y_t y_t^* \int_0^1 \mathrm{d}x \int \frac{\mathrm{d}^4\bar{q}}{(2\pi)^4} \frac{\bar{q}^2 - x(1-x)p^2}{[\bar{q}^2 + D]^2} \,, \tag{A.70}$$

where as usual we have dropped the $i\epsilon$ for clarity. After Wick rotating and evaluating the integral in $d = 4 - \epsilon$ dimensions, we find (for $m \to 0$)

$$\Pi^{H_u}_{\text{fermion}} = 3y_t y_t^* \big(-p^2\big) \lim_{\epsilon\to 0}\left\{\frac{1}{8\pi^2\epsilon}\right\} + \text{finite} \,. \tag{A.71}$$

The same analysis for the H_d propagator yields

$$\Pi^{H_d}_{\text{fermion}} = (3y_b y_b^* + y_\tau y_\tau^*) \big(-p^2\big) \lim_{\epsilon\to 0}\left\{\frac{1}{8\pi^2\epsilon}\right\} + \text{finite} \,. \tag{A.72}$$

A.2.4 One-loop result

To summarise:

$$\Pi_{\text{gauge}} = -\frac{(3g^2 + g'^2)}{4}(3-\xi)\big(-p^2\big) \lim_{\epsilon\to 0}\left\{\frac{1}{8\pi^2\epsilon}\right\} + \text{finite} \,; \tag{A.73}$$

$$\Pi_{\text{ino}} = -\frac{(3g^2 + g'^2)}{4}(-2)\big(-p^2\big) \lim_{\epsilon\to 0}\left\{\frac{1}{8\pi^2\epsilon}\right\} + \text{finite} \,; \tag{A.74}$$

and

$$\Pi^{H_u}_{\text{fermion}} = 3y_t y_t^* \big(-p^2\big) \lim_{\epsilon\to 0}\left\{\frac{1}{8\pi^2\epsilon}\right\} + \text{finite} \,, \tag{A.75}$$

$$\Pi^{H_d}_{\text{fermion}} = (3y_b y_b^* + y_\tau y_\tau^*) \big(-p^2\big) \lim_{\epsilon\to 0}\left\{\frac{1}{8\pi^2\epsilon}\right\} + \text{finite} \,. \tag{A.76}$$

The one-loop correction is given by the sum of these contributions, so we find that the wavefunction renormalisation of the Higgs doublets that is required to compensate for these divergences is given by

$$\mathcal{Z}_{H_{\text{u}}} = 1 + \lim_{\epsilon\to 0}\left\{\frac{1}{8\pi^2\epsilon}\right\}\left[\frac{(3g^2 + g'^2)}{4}\big(1-\xi\big) - 3y_t y_t^*\right] \,, \tag{A.77}$$

$$\mathcal{Z}_{H_{\text{d}}} = 1 + \lim_{\epsilon\to 0}\left\{\frac{1}{8\pi^2\epsilon}\right\}\left[\frac{(3g^2 + g'^2)}{4}\big(1-\xi\big) - 3y_b y_b^* - y_\tau y_\tau^*\right] \,. \tag{A.78}$$

A.3 RG evolution

The final task is to combine the one-loop corrections to the Higgs propagators and the vertex in order to determine the RG flow equation for the coupling Z. This corresponds to computing the anomalous dimension of the vertex, defined as

$$\gamma_Z = \frac{\mathrm{d}\ln Z}{\mathrm{d}\ln\mu} \,, \tag{A.79}$$

where Z is the renormalised coupling to $H_\mathrm{u}H_\mathrm{d}\Box\Phi$. The bare coupling Z_0, defined by

$$\mathcal{L} \supset \frac{1}{\sqrt{6}M_\mathrm{P}}\Big[Z_0 H_{\mathrm{u}0}H_{\mathrm{d}0}\Box\Phi_0 + \mathrm{h.c.}\Big] \,, \tag{A.80}$$

must be independent of the renormalisation scale μ, i.e.

$$\frac{\mathrm{d}\ln Z_0}{\mathrm{d}\ln\mu} = 0 \,. \tag{A.81}$$

The loop corrections to Φ are Planck-suppressed, so we can set $\Phi = \Phi_0$; on the other hand the Higgs doublets receive radiative corrections (computed in section A.2) such that $H_\mathrm{u} = \mathcal{Z}_{H_\mathrm{u}}^{-1/2}H_{\mathrm{u}0}$ and $H_\mathrm{d} = \mathcal{Z}_{H_\mathrm{d}}^{-1/2}H_{\mathrm{d}0}$.[4] Re-expressing the relevant term in the Lagrangian (in $d = 4-\epsilon$) as

$$\mathcal{L} \supset \frac{1}{\sqrt{6}M_\mathrm{P}}\left(\mathcal{Z}_Z Z\mu^{\epsilon/2}H_\mathrm{u}H_\mathrm{d}\Box\Phi + \mathrm{h.c.}\right) \,, \tag{A.82}$$

we can see that the bare and renormalised couplings are related by

$$Z_0 = \mathcal{Z}_Z\mathcal{Z}_{H_\mathrm{u}}^{-1/2}\mathcal{Z}_{H_\mathrm{d}}^{-1/2}\mu^{\epsilon/2}Z \,. \tag{A.83}$$

Defining

$$F \equiv \ln\left(\mathcal{Z}_Z\mathcal{Z}_{H_\mathrm{u}}^{-1/2}\mathcal{Z}_{H_\mathrm{d}}^{-1/2}\right) \,, \tag{A.84}$$

we can use equation (A.81) to deduce that

$$\frac{\mathrm{d}\ln Z}{\mathrm{d}\ln\mu} + \left(\frac{\partial}{\partial\ln\mu} + \frac{\mathrm{d}g}{\mathrm{d}\ln\mu}\frac{\partial}{\partial g} + \frac{\mathrm{d}g'}{\mathrm{d}\ln\mu}\frac{\partial}{\partial g'} + \frac{\mathrm{d}y_t}{\mathrm{d}\ln\mu}\frac{\partial}{\partial y_t} + \frac{\mathrm{d}y_t^*}{\mathrm{d}\ln\mu}\frac{\partial}{\partial y_t^*}\right)F + \frac{\epsilon}{2} = 0 \,. \tag{A.85}$$

[4]The intuition for this is that the $\mathcal{Z}_H$ factors renormalise the kinetic terms in the Higgs Lagrangian.

Expanding in powers of $1/\epsilon$, we can write

$$\mathcal{Z}_Z = 1 + \sum_{n=1}^{\infty} \frac{\mathcal{Z}_Z^{(n)}}{(8\pi^2)^n \epsilon^n} \,, \tag{A.86}$$

$$\mathcal{Z}_{H_\mathrm{u}} = 1 + \sum_{n=1}^{\infty} \frac{\mathcal{Z}_{H_\mathrm{u}}^{(n)}}{(8\pi^2)^n \epsilon^n} \,, \tag{A.87}$$

$$\mathcal{Z}_{H_\mathrm{d}} = 1 + \sum_{n=1}^{\infty} \frac{\mathcal{Z}_{H_\mathrm{d}}^{(n)}}{(8\pi^2)^n \epsilon^n} \,, \tag{A.88}$$

and

$$F = \sum_{n=1}^{\infty} \frac{F^{(n)}}{(8\pi^2)^n \epsilon^n} \,. \tag{A.89}$$

Using equation (A.84) and comparing powers of $1/\epsilon$ gives

$$F^{(1)} = \mathcal{Z}_Z^{(1)} - \frac{1}{2}\big(\mathcal{Z}_{H_\mathrm{u}}^{(1)} + \mathcal{Z}_{H_\mathrm{d}}^{(1)}\big) \,. \tag{A.90}$$

From sections A.1 and A.2 we know that

$$\mathcal{Z}_Z^{(1)} = -\frac{(3g^2 + g'^2)}{4}\big(1 + \xi\big) \,, \tag{A.91}$$

$$\mathcal{Z}_{H_\mathrm{u}}^{(1)} = \frac{(3g^2 + g'^2)}{4}\big(1 - \xi\big) - 3y_t y_t^* \,, \tag{A.92}$$

$$\mathcal{Z}_{H_\mathrm{d}}^{(1)} = \frac{(3g^2 + g'^2)}{4}\big(1 - \xi\big) - 3y_b y_b^* - y_\tau y_\tau^* \,. \tag{A.93}$$

Therefore

$$F^{(1)} = -\frac{3g^2}{2} - \frac{g'^2}{2} + \frac{3y_t y_t^*}{2} + \frac{3y_b y_b^*}{2} + \frac{y_\tau y_\tau^*}{2} \,. \tag{A.94}$$

Combining this with (A.79) and (A.85), and using the fact that

$$\frac{\mathrm{d}c_i}{\mathrm{d}\ln\mu} = -\frac{\epsilon}{2}c_i + \beta_i \tag{A.95}$$

for all couplings c_i, we arrive at the final result,[5]

$$\gamma_Z = \frac{1}{16\pi^2}\bigg(-3g^2 - g'^2 + 3y_t y_t^* + 3y_b y_b^* + y_\tau y_\tau^*\bigg) \,. \tag{A.96}$$

[5]For comparison with (2.27), note that $g_1 = \sqrt{5/3}\,g'$ and $g_2 = g$.

Bibliography

[1] S. Angus and J. P. Conlon, *Soft Supersymmetry Breaking in Anisotropic LARGE Volume Compactifications*, *JHEP* **1303** (2013) 071, [arXiv:1211.6927].

[2] S. Angus, J. P. Conlon, U. Haisch, and A. J. Powell, *Loop corrections to ΔN_{eff} in large volume models*, *JHEP* **1312** (2013) 061, [arXiv:1305.4128].

[3] S. Angus, J. P. Conlon, M. C. D. Marsh, A. Powell, and L. T. Witkowski, *Soft X-ray Excess in the Coma Cluster from a Cosmic Axion Background*, arXiv:1312.3947.

[4] S. Angus, *Dark Radiation in Anisotropic LARGE Volume Compactifications*, arXiv:1403.6473.

[5] P. Horava and E. Witten, *Heterotic and type I string dynamics from eleven-dimensions*, *Nucl.Phys.* **B460** (1996) 506–524, [hep-th/9510209].

[6] M. R. Douglas, *The Statistics of string / M theory vacua*, *JHEP* **0305** (2003) 046, [hep-th/0303194].

[7] S. Kachru, R. Kallosh, A. D. Linde, and S. P. Trivedi, *De Sitter vacua in string theory*, *Phys.Rev.* **D68** (2003) 046005, [hep-th/0301240].

[8] V. Balasubramanian, P. Berglund, J. P. Conlon, and F. Quevedo, *Systematics of moduli stabilisation in Calabi-Yau flux compactifications*, *JHEP* **0503** (2005) 007, [hep-th/0502058].

[9] J. P. Conlon, F. Quevedo, and K. Suruliz, *Large-volume flux compactifications: Moduli spectrum and D3/D7 soft supersymmetry breaking*, *JHEP* **0508** (2005) 007, [hep-th/0505076].

[10] M. Cicoli, J. P. Conlon, and F. Quevedo, *General Analysis of LARGE Volume Scenarios with String Loop Moduli Stabilisation*, *JHEP* **0810** (2008) 105, [arXiv:0805.1029].

[11] **Planck** Collaboration, P. Ade et al., *Planck 2013 results. XVI. Cosmological parameters*, arXiv:1303.5076.

[12] Z. Hou, C. Reichardt, K. Story, B. Follin, R. Keisler, et al., *Constraints on Cosmology from the Cosmic Microwave Background Power Spectrum of the 2500-square degree SPT-SZ Survey*, *Astrophys.J.* **782** (2014) 74, [arXiv:1212.6267].

[13] **Atacama Cosmology Telescope** Collaboration, J. L. Sievers et al., *The Atacama Cosmology Telescope: Cosmological parameters from three seasons of data*, *JCAP* **1310** (2013) 060, [arXiv:1301.0824].

[14] **WMAP** Collaboration, G. Hinshaw et al., *Nine-Year Wilkinson Microwave Anisotropy Probe (WMAP) Observations: Cosmological Parameter Results*, *Astrophys.J.Suppl.* **208** (2013) 19, [arXiv:1212.5226].

[15] A. G. Riess, L. Macri, S. Casertano, H. Lampeitl, H. C. Ferguson, et al., *A 3Telescope and Wide Field Camera 3*, *Astrophys.J.* **730** (2011) 119, [arXiv:1103.2976].

[16] R. Cooke, M. Pettini, R. A. Jorgenson, M. T. Murphy, and C. C. Steidel, *Precision measures of the primordial abundance of deuterium*, arXiv:1308.3240.

[17] **BICEP2** Collaboration, P. Ade et al., *Detection of B-Mode Polarization at Degree Angular Scales by BICEP2*, *Phys.Rev.Lett.* **112** (2014) 241101, [arXiv:1403.3985].

[18] E. Giusarma, E. Di Valentino, M. Lattanzi, A. Melchiorri, and O. Mena, *Relic Neutrinos, thermal axions and cosmology in early 2014*, arXiv:1403.4852.

[19] J.-F. Zhang, Y.-H. Li, and X. Zhang, *Sterile neutrinos help reconcile the observational results of primordial gravitational waves from Planck and BICEP2*, arXiv:1403.7028.

[20] C. Dvorkin, M. Wyman, D. H. Rudd, and W. Hu, *Neutrinos help reconcile Planck measurements with both Early and Local Universe*, arXiv:1403.8049.

[21] M. Cicoli, J. P. Conlon, and F. Quevedo, *Dark Radiation in LARGE Volume Models*, *Phys.Rev.* **D87** (2013), no. 4 043520, [arXiv:1208.3562].

[22] T. Higaki and F. Takahashi, *Dark Radiation and Dark Matter in Large Volume Compactifications*, *JHEP* **1211** (2012) 125, [arXiv:1208.3563].

[23] J. Wess and J. Bagger, *Supersymmetry and supergravity: Revised and Expanded Edition*. Princeton University Press, 1992.

[24] S. Gukov, C. Vafa, and E. Witten, *CFT's from Calabi-Yau four folds*, *Nucl.Phys.* **B584** (2000) 69–108, [hep-th/9906070].

[25] G. Coughlan, W. Fischler, E. W. Kolb, S. Raby, and G. G. Ross, *Cosmological Problems for the Polonyi Potential*, *Phys.Lett.* **B131** (1983) 59.

[26] T. Banks, D. B. Kaplan, and A. E. Nelson, *Cosmological implications of dynamical supersymmetry breaking*, *Phys.Rev.* **D49** (1994) 779–787, [hep-ph/9308292].

[27] B. de Carlos, J. Casas, F. Quevedo, and E. Roulet, *Model independent properties and cosmological implications of the dilaton and moduli sectors of 4-d strings*, *Phys.Lett.* **B318** (1993) 447–456, [hep-ph/9308325].

[28] R. Blumenhagen, J. Conlon, S. Krippendorf, S. Moster, and F. Quevedo, *SUSY Breaking in Local String/F-Theory Models*, *JHEP* **0909** (2009) 007, [arXiv:0906.3297].

[29] A. Hebecker, A. K. Knochel, and T. Weigand, *A Shift Symmetry in the Higgs Sector: Experimental Hints and Stringy Realizations*, *JHEP* **1206** (2012) 093, [arXiv:1204.2551].

[30] A. Hebecker, A. K. Knochel, and T. Weigand, *The Higgs mass from a String-Theoretic Perspective*, *Nucl.Phys.* **B874** (2013) 1–35, [arXiv:1304.2767].

[31] M. Dine, L. Randall, and S. D. Thomas, *Supersymmetry breaking in the early universe*, *Phys.Rev.Lett.* **75** (1995) 398–401, [hep-ph/9503303].

[32] G. Giudice and A. Masiero, *A Natural Solution to the mu Problem in Supergravity Theories*, *Phys.Lett.* **B206** (1988) 480–484.

[33] M. T. Grisaru, W. Siegel, and M. Rocek, *Improved Methods for Supergraphs*, *Nucl.Phys.* **B159** (1979) 429.

[34] M. E. Machacek and M. T. Vaughn, *Two Loop Renormalization Group Equations in a General Quantum Field Theory. 1. Wave Function Renormalization*, *Nucl.Phys.* **B222** (1983) 83.

[35] M. E. Machacek and M. T. Vaughn, *Two Loop Renormalization Group Equations in a General Quantum Field Theory. 2. Yukawa Couplings*, *Nucl.Phys.* **B236** (1984) 221.

[36] D. Capper and D. Jones, *The Effective Potential in the Light Cone Gauge and Supersymmetric Yang-Mills Theories*, *Nucl.Phys.* **B252** (1985) 718.

[37] S. P. Martin, *A Supersymmetry primer*, *Adv.Ser.Direct.High Energy Phys.* **21** (2010) 1–153, [hep-ph/9709356].

[38] B. Allanach, *SOFTSUSY: a program for calculating supersymmetric spectra*, *Comput.Phys.Commun.* **143** (2002) 305–331, [hep-ph/0104145].

[39] D. M. Pierce, J. A. Bagger, K. T. Matchev, and R.-j. Zhang, *Precision corrections in the minimal supersymmetric standard model*, *Nucl.Phys.* **B491** (1997) 3–67, [hep-ph/9606211].

[40] **Particle Data Group** Collaboration, J. Beringer et al., *Review of Particle Physics (RPP)*, *Phys.Rev.* **D86** (2012) 010001.

[41] **CDF, D0** Collaboration, T. Aaltonen et al., *Combination of the top-quark mass measurements from the Tevatron collider*, *Phys.Rev.* **D86** (2012) 092003, [arXiv:1207.1069].

[42] M. Beneke, P. Falgari, S. Klein, and C. Schwinn, *Hadronic top-quark pair production with NNLL threshold resummation*, *Nucl.Phys.* **B855** (2012) 695–741, [arXiv:1109.1536].

[43] **ATLAS Collaboration** Collaboration, G. Aad et al., *Observation of a new particle in the search for the Standard Model Higgs boson with the ATLAS detector at the LHC*, *Phys.Lett.* **B716** (2012) 1–29, [arXiv:1207.7214].

[44] **CMS Collaboration** Collaboration, S. Chatrchyan et al., *Observation of a new boson at a mass of 125 GeV with the CMS experiment at the LHC*, *Phys.Lett.* **B716** (2012) 30–61, [arXiv:1207.7235].

[45] J. Casas, J. Espinosa, M. Quiros, and A. Riotto, *The Lightest Higgs boson mass in the minimal supersymmetric standard model*, *Nucl.Phys.* **B436** (1995) 3–29, [hep-ph/9407389].

[46] A. Dabelstein, *The One loop renormalization of the MSSM Higgs sector and its application to the neutral scalar Higgs masses*, *Z.Phys.* **C67** (1995) 495–512, [hep-ph/9409375].

[47] B. Allanach, A. Djouadi, J. Kneur, W. Porod, and P. Slavich, *Precise determination of the neutral Higgs boson masses in the MSSM*, *JHEP* **0409** (2004) 044, [hep-ph/0406166].

[48] T. Higaki, K. Nakayama, and F. Takahashi, *Moduli-Induced Axion Problem*, *JHEP* **1307** (2013) 005, [arXiv:1304.7987].

[49] M. Cicoli, C. Burgess, and F. Quevedo, *Fibre Inflation: Observable Gravity Waves from IIB String Compactifications*, *JCAP* **0903** (2009) 013, [arXiv:0808.0691].

[50] M. Cicoli, C. Burgess, and F. Quevedo, *Anisotropic Modulus Stabilisation: Strings at LHC Scales with Micron-sized Extra Dimensions*, *JHEP* **1110** (2011) 119, [arXiv:1105.2107].

[51] M. Cicoli, F. G. Pedro, and G. Tasinato, *Poly-instanton Inflation*, *JCAP* **1112** (2011) 022, [arXiv:1110.6182].

[52] M. Cicoli, F. G. Pedro, and G. Tasinato, *Natural Quintessence in String Theory*, *JCAP* **1207** (2012) 044, [arXiv:1203.6655].

[53] R. Blumenhagen, X. Gao, T. Rahn, and P. Shukla, *Moduli Stabilization and Inflationary Cosmology with Poly-Instantons in Type IIB Orientifolds*, *JHEP* **1211** (2012) 101, [arXiv:1208.1160].

[54] M. Cicoli, M. Kreuzer, and C. Mayrhofer, *Toric K3-Fibred Calabi-Yau Manifolds with del Pezzo Divisors for String Compactifications*, *JHEP* **1202** (2012) 002, [arXiv:1107.0383].

[55] M. Cicoli, C. Mayrhofer, and R. Valandro, *Moduli Stabilisation for Chiral Global Models*, *JHEP* **1202** (2012) 062, [arXiv:1110.3333].

[56] R. Blumenhagen, X. Gao, T. Rahn, and P. Shukla, *A Note on Poly-Instanton Effects in Type IIB Orientifolds on Calabi-Yau Threefolds*, *JHEP* **1206** (2012) 162, [arXiv:1205.2485].

[57] A. Hebecker, P. Mangat, F. Rompineve, and L. T. Witkowski, *Dark Radiation predictions from general Large Volume Scenarios*, arXiv:1403.6810.

[58] M. Cicoli and A. Mazumdar, *Reheating for Closed String Inflation*, *JCAP* **1009** (2010) 025, [arXiv:1005.5076].

[59] C. Burgess, M. Cicoli, M. Gomez-Reino, F. Quevedo, G. Tasinato, et al., *Non-standard primordial fluctuations and nongaussianity in string inflation*, *JHEP* **1008** (2010) 045, [arXiv:1005.4840].

[60] M. Cicoli, G. Tasinato, I. Zavala, C. Burgess, and F. Quevedo, *Modulated Reheating and Large Non-Gaussianity in String Cosmology*, *JCAP* **1205** (2012) 039, [arXiv:1202.4580].

[61] R. Blumenhagen and M. Schmidt-Sommerfeld, *Power Towers of String Instantons for N=1 Vacua*, *JHEP* **0807** (2008) 027, [arXiv:0803.1562].

[62] J. P. Conlon, D. Cremades, and F. Quevedo, *Kahler potentials of chiral matter fields for Calabi-Yau string compactifications*, *JHEP* **0701** (2007) 022, [hep-th/0609180].

[63] A. Brignole, L. E. Ibanez, and C. Munoz, *Soft supersymmetry breaking terms from supergravity and superstring models*, *Adv.Ser.Direct.High Energy Phys.* **21** (2010) 244–268, [hep-ph/9707209].

[64] R. Blumenhagen, S. Moster, and E. Plauschinn, *Moduli Stabilisation versus Chirality for MSSM like Type IIB Orientifolds*, *JHEP* **0801** (2008) 058, [arXiv:0711.3389].

[65] T. W. Grimm, M. Kerstan, E. Palti, and T. Weigand, *On Fluxed Instantons and Moduli Stabilisation in IIB Orientifolds and F-theory*, *Phys.Rev.* **D84** (2011) 066001, [arXiv:1105.3193].

[66] J. P. Conlon, S. S. Abdussalam, F. Quevedo, and K. Suruliz, *Soft SUSY Breaking Terms for Chiral Matter in IIB String Compactifications*, *JHEP* **0701** (2007) 032, [hep-th/0610129].

[67] L. Aparicio, D. Cerdeno, and L. Ibanez, *Modulus-dominated SUSY-breaking soft terms in F-theory and their test at LHC*, *JHEP* **0807** (2008) 099, [arXiv:0805.2943].

[68] R. Kitano and Y. Nomura, *Supersymmetry, naturalness, and signatures at the LHC*, *Phys.Rev.* **D73** (2006) 095004, [hep-ph/0602096].

[69] S. Krippendorf, H. P. Nilles, M. Ratz, and M. W. Winkler, *The heterotic string yields natural supersymmetry*, *Phys.Lett.* **B712** (2012) 87–92, [arXiv:1201.4857].

[70] J. P. Conlon and M. C. D. Marsh, *Searching for a 0.1-1 keV Cosmic Axion Background*, *Phys.Rev.Lett.* **111** (2013) 151301, [arXiv:1305.3603].

[71] F. Zwicky, *On the Masses of Nebulae and of Clusters of Nebulae*, *Astrophys. J.* **86** (Oct., 1937) 217.

[72] R. Lieu, J. P. D. Mittaz, S. Bowyer, F. J. Lockman, C.-Y. Hwang, and J. H. M. M. Schmitt, *Discovery of 0.5 MK Gas in the Center of the Virgo Cluster*, *Astrophys. J.* **458** (Feb., 1996) L5.

[73] R. Lieu, J. P. D. Mittaz, S. Bowyer, J. O. Breen, F. J. Lockman, E. M. Murphy, and C.-Y. Hwang, *Diffuse Extreme-Ultraviolet Emission from the Coma Cluster: Evidence for Rapidly Cooling Gases at Submegakelvin Temperatures*, *Science* **274** (Nov., 1996) 1335–1338.

[74] S. Bowyer, M. Lampton, and R. Lieu, *Extreme-Ultraviolet Flux from the Virgo Cluster: Further Evidence for a 500,000-Kelvin Component*, *Science* **274** (Nov., 1996) 1338–1340.

[75] M. Bonamente, R. Lieu, M. K. Joy, and J. H. Nevalainen, *The Soft X-Ray Emission in a Large Sample of Galaxy Clusters with the ROSAT Position Sensitive Proportional Counter*, *Astrophys. J.* **576** (Sept., 2002) 688–707, [astro-ph/0205473].

[76] F. Durret, J. S. Kaastra, J. Nevalainen, T. Ohashi, and N. Werner, *Soft X-Ray and Extreme Ultraviolet Excess Emission from Clusters of Galaxies*, *Space Sci. Rev.* **134** (Feb., 2008) 51–70, [arXiv:0801.0977].

[77] J. P. Conlon and M. C. D. Marsh, *The Cosmophenomenology of Axionic Dark Radiation*, *JHEP* **1310** (2013) 214, [arXiv:1304.1804].

[78] P. Sikivie, *Experimental Tests of the Invisible Axion*, *Phys.Rev.Lett.* **51** (1983) 1415.

[79] C. Burrage, A.-C. Davis, and D. J. Shaw, *Active Galactic Nuclei Shed Light on Axion-like-Particles*, *Phys.Rev.Lett.* **102** (2009) 201101, [arXiv:0902.2320].

[80] C. Burrage, *Searching for axion-like-particles in the sky*, *Nucl.Phys.Proc.Suppl.* **194** (2009) 190–195.

[81] C. Burrage, A.-C. Davis, and D. J. Shaw, *Searching for Axion-like Particles with Active Galactic Nuclei*, arXiv:0912.1716.

[82] A. Bonafede, L. Feretti, M. Murgia, F. Govoni, G. Giovannini, D. Dallacasa, K. Dolag, and G. B. Taylor, *The Coma cluster magnetic field from Faraday rotation measures*, *Astron. Astrophys.* **513** (Apr., 2010) A30, [arXiv:1002.0594].

[83] A. Bonafede, F. Vazza, M. Brüggen, M. Murgia, F. Govoni, L. Feretti, G. Giovannini, and G. Ogrean, *Measurements and simulation of Faraday rotation across the Coma radio relic*, *Mon.Not.Roy.Astron.Soc.* **433** (Aug., 2013) 3208–3226, [arXiv:1305.7228].

[84] M. C. D. Marsh, *The Darkness of Spin-0 Dark Radiation*, arXiv:1407.2501.

[85] P. Sikivie, *Detection Rates for 'Invisible' Axion Searches*, *Phys.Rev.* **D32** (1985) 2988.

[86] T. Higaki, K. Nakayama, and F. Takahashi, *Cosmological constraints on axionic dark radiation from axion-photon conversion in the early Universe*, *JCAP* **1309** (2013) 030, [arXiv:1306.6518].

[87] M. Fairbairn, *Axionic Dark Radiation and the Milky Way's Magnetic Field*, *ArXiv e-prints* (Oct., 2013) [arXiv:1310.4464].

[88] M. A. G. Willson, *Radio observations of the cluster of galaxies in Coma Berenices - the 5C4 survey.*, *Mon.Not.Roy.Astron.Soc.* **151** (1970) 1–44.

[89] P. A. Henning, *30.9 MHz observations of the radio halo in the coma cluster of galaxies*, *Astron. J.* **97** (June, 1989) 1561–1565.

[90] K.-T. Kim, P. P. Kronberg, P. E. Dewdney, and T. L. Landecker, *The halo and magnetic field of the Coma cluster of galaxies*, *Astrophys. J.* **355** (May, 1990) 29–37.

[91] G. Giovannini, L. Feretti, T. Venturi, K.-T. Kim, and P. P. Kronberg, *The halo radio source Coma C and the origin of halo sources*, *Astrophys. J.* **406** (Apr., 1993) 399–406.

[92] M. Thierbach, U. Klein, and R. Wielebinski, *The diffuse radio emission from the Coma cluster at 2.675 GHz and 4.85 GHz*, *Astron. Astrophys.* **397** (Jan., 2003) 53–61, [astro-ph/0210147].

[93] R. Fusco-Femiano, M. Orlandini, G. Brunetti, L. Feretti, G. Giovannini, P. Grandi, and G. Setti, *Confirmation of Nonthermal Hard X-Ray Excess in the Coma Cluster from Two Epoch Observations*, *Astrophys. J.* **602** (Feb., 2004) L73–L76, [astro-ph/0312625].

[94] C. M. H. Chen, D. E. Harris, F. A. Harrison, and P. H. Mao, *Constraints on the average magnetic field strength of relic radio sources 0917+75 and 1401-33 from XMM-Newton observations*, *Mon.Not.Roy.Astron.Soc.* **383** (Jan., 2008) 1259–1268, [arXiv:0801.0288].

[95] L. Feretti, G. Giovannini, F. Govoni, and M. Murgia, *Clusters of galaxies: observational properties of the diffuse radio emission*, *Astron. Astrophys. Rev.* **20** (May, 2012) 54, [arXiv:1205.1919].

[96] L. Rudnick and K. M. Blundell, *Lowering Inferred Cluster Magnetic Field Strengths: The Radio Galaxy Contributions*, *Astrophys. J.* **588** (May, 2003) 143–154, [astro-ph/0301260].

[97] K.-T. Kim, P. P. Kronberg, P. E. Dewdney, and T. L. Landecker, *The halo and magnetic field of the Coma cluster of galaxies*, *Astrophys. J.* **355** (May, 1990) 29–37.

[98] L. Feretti, D. Dallacasa, G. Giovannini, and A. Tagliani, *The magnetic field in the Coma cluster.*, *Astron. Astrophys.* **302** (Oct., 1995) 680, [astro-ph/9504058].

[99] M. Murgia, F. Govoni, L. Feretti, G. Giovannini, D. Dallacasa, R. Fanti, G. B. Taylor, and K. Dolag, *Magnetic fields and Faraday rotation in clusters of galaxies*, *Astron. Astrophys.* **424** (Sept., 2004) 429–446, [astro-ph/0406225].

[100] R. A. Laing, A. H. Bridle, P. Parma, and M. Murgia, *Structures of the magnetoionic media around the Fanaroff-Riley Class I radio galaxies 3C31 and Hydra A*, *Mon.Not.Roy.Astron.Soc.* **391** (Dec., 2008) 521–549, [arXiv:0809.2411].

[101] C. Vogt and T. A. Enßlin, *A Bayesian View on Faraday Rotation Maps – Seeing the Magnetic Power Spectrum in Clusters of Galaxies*, *Journal of Korean Astronomical Society* **37** (Dec., 2004) 349–353.

[102] U. G. Briel, J. P. Henry, and H. Boehringer, *Observation of the Coma cluster of galaxies with ROSAT during the all-sky survey*, *Astron. Astrophys.* **259** (June, 1992) L31–L34.

[103] M. Frigo and S. G. Johnson, *The Design and Implementation of FFTW3*, *Proceedings of IEEE* **93** (2005) 216231.

[104] G. Raffelt and L. Stodolsky, *Mixing of the photon with low-mass particles*, *Phys. Rev.* **D37** (Mar., 1988) 1237–1249.

[105] E. L. Wright, *A Cosmology Calculator for the World Wide Web*, *Publ. Astron. Soc. Pac.* **118** (Dec., 2006) 1711–1715, [astro-ph/0609593].

[106] A. Ringwald, *Exploring the Role of Axions and Other WISPs in the Dark Universe*, *Phys.Dark Univ.* **1** (2012) 116–135, [arXiv:1210.5081].

[107] R. Bhre, B. Dbrich, J. Dreyling-Eschweiler, S. Ghazaryan, R. Hodajerdi, et al., *Any light particle search II Technical Design Report*, *JINST* **8** (2013) T09001, [arXiv:1302.5647].

[108] E. Armengaud, F. Avignone, M. Betz, P. Brax, P. Brun, et al., *Conceptual Design of the International Axion Observatory (IAXO)*, arXiv:1401.3233.

[109] G. G. Raffelt, *Stars as laboratories for fundamental physics: the astrophysics of neutrinos, axions, and other weakly interacting particles*. University of Chicago Press, Chicago, USA, 1996.

[110] A. Friedland, M. Giannotti, and M. Wise, *Constraining the Axion-Photon Coupling with Massive Stars*, *Phys.Rev.Lett.* **110** (2013) 061101, [arXiv:1210.1271].

[111] J. W. Brockway, E. D. Carlson, and G. G. Raffelt, *SN1987A gamma-ray limits on the conversion of pseudoscalars*, *Phys.Lett.* **B383** (1996) 439–443, [astro-ph/9605197].

[112] J. Grifols, E. Masso, and R. Toldra, *Gamma-rays from SN1987A due to pseudoscalar conversion*, *Phys.Rev.Lett.* **77** (1996) 2372–2375, [astro-ph/9606028].

[113] M. Meyer, D. Horns, and M. Raue, *First lower limits on the photon-axion-like particle coupling from very high energy gamma-ray observation*, *Phys.Rev.* **D87** (2013) 035027, [arXiv:1302.1208].

[114] A. De Angelis, M. Roncadelli, and O. Mansutti, *Evidence for a new light spin-zero boson from cosmological gamma-ray propagation?*, *Phys.Rev.* **D76** (2007) 121301, [arXiv:0707.4312].

[115] M. Simet, D. Hooper, and P. D. Serpico, *The Milky Way as a Kiloparsec-Scale Axionscope*, *Phys.Rev.* **D77** (2008) 063001, [arXiv:0712.2825].

[116] M. Sanchez-Conde, D. Paneque, E. Bloom, F. Prada, and A. Dominguez, *Hints of the existence of Axion-Like-Particles from the gamma-ray spectra of cosmological sources*, *Phys.Rev.* **D79** (2009) 123511, [arXiv:0905.3270].

[117] D. Horns, L. Maccione, M. Meyer, A. Mirizzi, D. Montanino, et al., *Hardening of TeV gamma spectrum of AGNs in galaxy clusters by conversions of photons into axion-like particles*, *Phys.Rev.* **D86** (2012) 075024, [arXiv:1207.0776].

[118] J. Isern, E. García-Berro, S. Torres, and S. Catalán, *Axions and the Cooling of White Dwarf Stars*, *Astrophys. J.* **682** (Aug., 2008) L109–L112, [arXiv:0806.2807].

[119] J. Isern, S. Catalán, E. García-Berro, and S. Torres, *Axions and the white dwarf luminosity function*, *Journal of Physics Conference Series* **172** (June, 2009) 012005, [arXiv:0812.3043].

[120] J. Isern, *White dwarfs as physics laboratories: the case of axions*, in *7th Patras Workshop on Axions, WIMPs and WISPs (PATRAS 2011)* (K. Zioutas and M. Schumann, eds.), p. 158, Jan., 2012. arXiv:1204.3565.

[121] R. Jansson and G. R. Farrar, *A New Model of the Galactic Magnetic Field*, *Astrophys. J.* **757** (Sept., 2012) 14, [arXiv:1204.3662].

[122] R. Jansson and G. R. Farrar, *The Galactic Magnetic Field*, *Astrophys. J.* **761** (Dec., 2012) L11, [arXiv:1210.7820].

[123] D. Kraljic, M. Rummel, and J. P. Conlon, *ALP Conversion and the Soft X-ray Excess in the Outskirts of the Coma Cluster*, arXiv:1406.5188.

[124] E. Bulbul, M. Markevitch, A. Foster, R. K. Smith, M. Loewenstein, et al., *Detection of An Unidentified Emission Line in the Stacked X-ray*

spectrum of Galaxy Clusters, *Astrophys.J.* **789** (2014) 13, [arXiv:1402.2301].

[125] A. Boyarsky, O. Ruchayskiy, D. Iakubovskyi, and J. Franse, *An unidentified line in X-ray spectra of the Andromeda galaxy and Perseus galaxy cluster*, arXiv:1402.4119.

[126] M. Cicoli, J. P. Conlon, M. C. D. Marsh, and M. Rummel, *A 3.55 keV Photon Line and its Morphology from a 3.55 keV ALP Line*, *Phys.Rev.* **D90** (2014) 023540, [arXiv:1403.2370].

[127] J. P. Conlon and A. J. Powell, *A 3.55 keV line from DM $\to a \to \gamma$: predictions for cool-core and non-cool-core clusters*, arXiv:1406.5518.

[128] J. P. Conlon and F. V. Day, *3.55 keV photon lines from axion to photon conversion in the Milky Way and M31*, arXiv:1404.7741.